CHAPTER 1

The Basic Physics of Intersubband Transitions

Manfred Helm

INSTITUT FÜR HALBLEITER- UND FESTKÖRPERPHYSIK
JOHANNES-KEPLER-UNIVERSITÄT LINZ
LINZ, AUSTRIA

I. INTRODUCTION 1
II. THE INTERSUBBAND ABSORPTION COEFFICIENT 5
III. THE SYMMETRIC QUANTUM WELL 14
IV. EXPERIMENTAL GEOMETRIES AND THEIR ELECTROMAGNETICS 19
V. ASYMMETRIC QUANTUM WELLS 26
VI. MULTIQUANTUM WELLS AND SUPERLATTICES 32
VII. NONPARABOLICITY AND MANY-BODY EFFECTS 39
1. *Nonparabolicity* 40
2. *Self-Consistent Coulomb Potential* 42
3. *Many-Body Effects on the Energy (Exchange and Correlation)* 45
4. *Collective Effects on the Absorption (Depolarization and Exciton Shift)* . . . 47
VIII. MECHANISMS FOR IN-PLANE ABSORPTION 54
1. *Indirect-Gap Semiconductors* 54
2. *Spatial Variation of the Effective Mass* 56
3. *Coupling to the Valence Band* 57
IX. INTERSUBBAND ABSORPTION IN THE VALENCE BAND 59
X. LINE BROADENING AND RELAXATION 73
XI. OTHER PHENOMENA RELATED TO INTERSUBBAND TRANSITIONS 80
1. *Magnetic-Field Effects* 80
2. *Parabolic Quantum Wells* 84
3. *Impurities* 86
4. *Photon Drag Effect* 88
XII. CONCLUDING REMARKS AND OUTLOOK 90
REFERENCES 91

I. Introduction

The term intersubband transitions has been used to describe optical transitions between quasi-two-dimensional electronic states in semiconductors ("subbands"), which are formed due to the confinement of the electron

ISBN 0-12-752171-2
ISSN 0080-8784/00 $30.00

wave function in one dimension. The formation of such low-dimensional electronic systems has been one of the major topics of semiconductor physics for the past two and a half decades (Ando *et al.*, 1982), and in this context, the term "band-structure engineering" was coined. This development has been mainly triggered by epitaxial crystal growth techniques such as molecular beam epitaxy, which provides atomic-layer control of layer thicknesses.

In these terms, the conceptually simplest band-structure engineered system that can be fabricated is a quantum well, which consists of a thin semiconductor layer (of the order of 100 Å) embedded in a semiconductor with a larger bandgap (see Fig. 1). Depending on the relative band offsets of the two semiconductor materials, both electrons and holes can be confined in one direction in the conduction band and the valence band, respectively, and one obtains allowed energy levels that are quantized along the growth direction. These energy levels can be tuned by the quantum well depth and thickness. Whereas, of course, optical transitions can take place between valence and conduction band states, in this chapter the term "intersubband transitions" is used solely for transitions between quantized levels within the conduction (or valence) band (Fig. 1 schematically shows both interband and intersubband transitions).

The first experimental evidence for quantized states in a semiconductor quantum well was presented by Dingle *et al.* in 1974 through optical bandgap spectroscopy in a GaAs/AlGaAs structure. Later Esaki and Sakaki

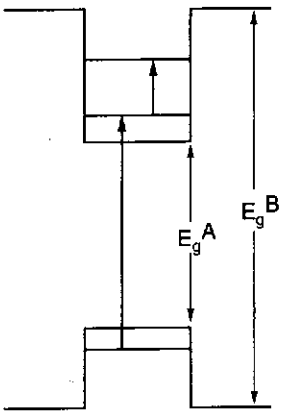

FIG. 1. Schematic of a quantum well made from a semiconductor with energy gap E_g^A embedded in a semiconductor with gap E_g^B. Subbands in the conduction and valence band are indicated as well as interband and intersubband transitions.

(1977) and Smith *et al.* (1983) showed the possibility of using intersubband transitions in quantum wells for infrared light detection. More than 10 years after the Dingle *et al.* report, intersubband absorption in a GaAs–AlGaAs quantum well was observed by West and Eglash (1985). Although this is often quoted as the beginning of intersubband spectroscopy, researchers put a lot of effort into the investigation of another quasi-two-dimensional electron system much earlier. Fowler *et al.* (1966) showed that the conducting channel in a Si-MOSFET (metal-oxide semiconductor field effect transistor) is effectively a two-dimensional electron gas that is formed at the interface between the Si and the oxide. Extensive investigation of this system followed, and Kamgar *et al.* (1974) reported the observation of intersubband absorption in a Si accumulation layer. Similar research was carried out on the GaAs–AlGaAs system, and in 1983, intersubband absorption was reported in an inversion layer at the interface of a GaAs–AlGaAs heterostructure (Schlesinger *et al.*, 1983).

These works remained relatively unknown to many researchers who later entered the field; one reason for this may be the fact that in these accumulation and inversion layers, the absorption wavelength was in the far infrared (FIR), at wavelengths longer than 40 μm, whereas in the work of West and Eglash (1985) the absorption occurred in the technologically more important range around 10 μm. Nevertheless the physical mechanism is, of course, the same in both types of structures.

After 1985, the number of works on intersubband absorption in quantum wells increased dramatically, most often motivated by the high technological potential of intersubband transitions for novel infrared detectors (Levine, 1993), emitters, and nonlinear optical elements. Research in these three areas has been so successful that each is covered in separate chapters of this volume. For example, focal-plane arrays of intersubband detectors (quantum well infrared photodetectors, QWIPs) with high detectivities have been fabricated (see Chapter 4) by a number of groups and intersubband lasers (quantum cascade lasers) (Faist *et al.*, 1994a; see also the corresponding chapter in this volume) were finally demonstrated in 1994.

Intersubband transitions have been observed in many different material systems. Apart from GaAs–AlGaAs the most important are strained InGaAs–AlGaAs structures, InGaAs–InAlAs lattice matched to InP, and InAs–AlGaSb structures. Much work has also been done with quantum wells based on group IV elements such as Si–SiGe. Both conduction and valence-band quantum wells have been employed. Besides the usual way of introducing *n*- or *p*-type doping into the quantum wells, a number of investigations were devoted to photoinduced intersubband absorption (Olszakier *et al.*, 1989; Yang *et al.*, 1990; Abramovich *et al.*, 1994; Julien and Boucaud, 1997). Here, electrons and holes are created in undoped material

using above-bandgap radiation and the intersubband absorption is studied simultaneously.

The photon energy (or wavelength) range accessible with intersubband transitions is limited through the magnitude of the conduction- or valence-band offset of the heterojunction on the high-energy side, and by the typical intersubband linewidth on the low-energy side. Currently, the spectral range covered by intersubband transitions extends over more than two orders of magnitude, from 200 (Helm *et al.*, 1991) to 2 μm (Chui *et al.*, 1994). Even the technologically important wavelength of 1.55 μm has been reached (Smet *et al.*, 1994). The development of intersubband physics research over the past decade can be followed in the proceedings of the Intersubband Physics Workshop, which has been held every two years since 1991. These were published as books (Rosencher *et al.*, 1992; H. C. Liu *et al.*, 1994; Li and Su, 1998) and in *Superlattices and Microstructures*, volume 19 (1996), respectively.

This chapter covers the more basic aspects of intersubband transitions with a main emphasis on linear absorption. Intersubband emission is covered in Chapter 5 by Faist *et al.* (see also the review by Perera *et al.*, 1997). A more compact account of some of the material covered here is due to Loehr and Manasreh (1993). The organization of the chapter is as follows.

In Section II, we derive an expression for the intersubband absorption coefficient based on Fermi's golden rule for the induced transition rate in the framework of the one-band effective mass approximation. In Section III this is applied to the case of a symmetric single quantum well. Section IV discusses several experimental geometries that enable coupling of the electromagnetic wave to the intersubband transition, which in most cases requires a polarization component perpendicular to the quantum well (QW) layers. Section V discusses asymmetrically shaped QW potentials, such as those induced by a vertical electric field or by variation of alloy composition. Due to the symmetry breaking, more transitions become allowed than in the symmetric situation. In Section VI we consider multiple quantum wells and superlattices, especially with regard to the formation of extended minibands with a finite dispersion along the growth direction. Section VII is devoted to the discussion of effects going beyond the most simple single-particle, one-band model, which are nonparabolicity and the inclusion of Coulomb and many-body effects in the intersubband absorption. In some situations, radiation polarized parallel to the layers can also be absorbed. These are discussed in Section VIII. The most important one exhibits constant-energy ellipsoids that are tilted away from the QW confinement direction. Intersubband absorption can take place not only in the conduction band but also in the valence band of *p*-type doped QWs. Due to the complicated valence–

band structure, this requires a more sophisticated theoretical treatment on the basis of a multilevel $\mathbf{k}\cdot\mathbf{p}$ Luttinger–Kohn type Hamiltonian, which is presented in Section IX. In Section X, we discuss line broadening and intersubband relaxation. In a loosely connected manner, Section XI presents several other effects also related to intersubband transitions, including magnetic-field effects, parabolic quantum wells, impurities, and the photon drag effect.

II. The Intersubband Absorption Coefficient

In this section, we derive an expression for the intersubband absorption coefficient based on Fermi's golden rule for the induced transition rate. On a more sophisticated level, the absorption spectrum can be calculated in a full many-body framework using linear response theory. Here, however, we present the single-particle approach, to which several many-body corrections can be added afterward. (For more discussion and references on this issue, see Section VII). For the moment, we restrict ourselves to the case of a single electronic band; that is, we make use of the envelope-function approach in the effective-mass approximation.

The total wave function $\psi_i(\mathbf{r})$ can then be written as the product between the lattice-periodic Bloch function of band v at the center (or another extremum) of the Brillouin zone $u_v(\mathbf{r})$ and an envelope function $f_i(\mathbf{r})$, which is supposed to vary slowly over one lattice period.

$$\psi_i(\mathbf{r}) = f_i(\mathbf{r})u_v(\mathbf{r}) \tag{1}$$

where i denotes the quantum numbers of the problem. This provides a reasonably good description for the conduction band of many semiconductors including GaAs. More accurate descriptions, which include several bands, are briefly discussed in Section VIII and more extensively in Section IX in connection with valence-band intersubband transitions. Equation (1) is simply a generalization of the usual Bloch ansatz for a bulk crystal, where the envelope function $f_i(\mathbf{r})$ reduces to a plane wave $e^{i\mathbf{k}\cdot\mathbf{r}}$. The envelope function $f_i(\mathbf{r})$ will depend on the shape of the quantum well potential or other external potentials such as electric and magnetic fields.

Under the assumption that the lattice-periodic function is the same in all constituent materials a Schrödinger equation only for the envelope function can be derived:

$$\frac{-\hbar^2}{2m^*}\nabla^2 f_i(\mathbf{r}) + V(\mathbf{r})f_i(\mathbf{r}) = E_i f_i(\mathbf{r}) \tag{2}$$

When z is chosen the growth direction, the free motion in the x and y directions, can be separated:

$$f_{n\mathbf{k}_\perp}(\mathbf{r}) = \frac{1}{\sqrt{A}} e^{i\mathbf{k}_\perp \cdot \mathbf{r}} \varphi_n(z) \tag{3}$$

where $\mathbf{k}_\perp$ denotes the two-dimensional vector (k_x, k_y) and A is the sample area. Then Eq. (3) reduces to a one-dimensional Schrödinger equation of the textbook form

$$\frac{-\hbar^2}{2m^*} \frac{d^2\varphi_n}{dz^2} + V(z)\varphi_n(z) = E_n \varphi_n(z) \tag{4}$$

This equation must be solved in each material layer $(A, B, \ldots)$ of the heterostructure, and the solutions have to be connected with the following matching conditions at each interface z_0:

$$\varphi^A(z_0) = \varphi^B(z_0) \qquad \text{and} \qquad \frac{1}{m^{*A}} \frac{d\varphi^A}{dz}(z_0) = \frac{1}{m^{*B}} \frac{d\varphi^B}{dz}(z_0) \tag{5}$$

The latter condition ensures conservation of the probability current, but as a consequence, the envelope function has a kink at each interface when the effective mass is discontinuous. In this case, the first term in Eq. (4) is better written in the form $-(\hbar^2/2)(d/dz)[1/m^*(z)](d/dz)\varphi_n(z)$.

The solution of Eqs. (2) and (4) leads to energy eigenvalues of the form

$$E_{n,\mathbf{k}_\perp} = E_n + \frac{\hbar^2 \mathbf{k}_\perp^2}{2m^*} \tag{6}$$

where the subband energies E_n depend on the shape of $V(z)$.

In simple cases, such as the finite, symmetric quantum well, Eq. (4) can be solved analytically, but for more complicated structures the solution must be obtained numerically. The most common method for an arbitrary one-dimensional potential is the well-documented, so-called transfer matrix method (Kane, 1969; Chuang, 1995). In this method, the potential is assumed to be piecewise constant, thus having plane-wave solutions (with either real or imaginary k-vector). The set of matching conditions in Eq. (5) is formulated in a 2×2 matrix at each interface. The solution is then achieved by multiplication of all matrices together with the requirement that the wave functions decay exponentially at each end of the structure.

Now let us turn to the calculation of the absorption coefficient. We start from Fermi's golden rule for the transition rate form a state i to a state f

induced by an external electromagnetic field

$$W_{if} = \frac{2\pi}{\hbar} |\langle \psi_i | H' | \psi_f \rangle|^2 \delta(E_f - E_i - \hbar\omega) \tag{7}$$

where H' is the interaction Hamiltonian, $H' = (e/2m^*)(\mathbf{A} \cdot \mathbf{p} + \mathbf{p} \cdot \mathbf{A})$ (the electron charge is $-e$). It can be shown (Bastard, 1988) that in a one-band effective-mass model, the interaction is correctly described when the effective mass m^* is used in this expression and not the free-electron mass. A linearly polarized, plane electromagnetic wave is described by

$$\mathbf{E} = E_0 \mathbf{e} \cos(\mathbf{q} \cdot \mathbf{r} - \omega t) \tag{8}$$

where $\mathbf{E}$ is the electric field, $\mathbf{e}$ is the polarization vector, and $\mathbf{q}$ is the propagation vector. The corresponding vector potential, which is related to the electric field by $\mathbf{E} = -\partial \mathbf{A}/\partial t$, can be written as

$$\mathbf{A} = \frac{iE_0 e}{2\omega} e^{i(\mathbf{q} \cdot \mathbf{r} - \omega t)} + \text{c.c.} \tag{9}$$

At this point, we can employ the dipole approximation, which requires the wavelength of the radiation to be much larger than any characteristic dimension of electronic origin. This is the lattice period for interband transitions and the quantum well width for intersubband transitions; in both cases, the dipole approximation is very well fulfilled. (Note, however, that electric quadrupole transitions were discussed by Sa'ar, 1993.) Then $\mathbf{p}$ commutes with $\mathbf{A}$, which leads to $H' = (e/m^*)\mathbf{A} \cdot \mathbf{p}$, and we obtain

$$W_{if} = \frac{2\pi}{\hbar} \frac{e^2 E_0^2}{4m^{*2}\omega^2} |\langle i | \mathbf{e} \cdot \mathbf{p} | f \rangle|^2 \delta(E_f - E_i - \hbar\omega) \tag{10}$$

Before deriving the absorption coefficient from the transition rate, we take a closer look at the matrix element in Eq. (10). Due to the properties of the periodic Bloch functions and the slowly varying envelope functions (Eq. (1)), the complete matrix element can be split up in the following way (Bastard, 1988):

$$\langle i | \mathbf{e} \cdot \mathbf{p} | f \rangle = \mathbf{e} \cdot \langle u_v | \mathbf{p} | u_{v'} \rangle \langle f_n | f_{n'} \rangle + \mathbf{e} \cdot \langle u_v | u_{v'} \rangle \langle f_n | \mathbf{p} | f_{n'} \rangle \tag{11}$$

where v and v' and n and n' are the band and subband indices of the initial and final states, respectively. The first term describes interband transitions,

which are accompanied by a change of the band index ν (e.g., transitions from the valence band to the conduction band). It consists of a dipole matrix element of Bloch functions, which dictates the interband polarization selection rules, and an overlap integral of the envelope functions, which gives rise to selection rules concerning the electron and hole subband quantum numbers. If the initial and the final bands are the same, as in the case of intersubband transitions in the conduction band, this term vanishes. Then the second term, which describes transitions between subbands in the same band, becomes relevant. It consists of an overlap integral of Bloch functions (which vanishes for $\nu \neq \nu'$ and is unity for $\nu = \nu'$), and a dipole matrix element of the envelope functions. This last term is the only one relevant for intersubband transitions treated in the one-band model. In a multiband model, which is necessary to describe intersubband transitions in the valence band, however, both terms are important. We come back to this point in Section IX.

Thus let us evaluate the dipole matrix element of the envelope functions:

$$\langle f_{n\mathbf{k}_\perp} | \mathbf{e} \cdot \mathbf{p} | f_{n'\mathbf{k}'_\perp} \rangle = \frac{1}{A} \int d^3r e^{-i\mathbf{k}_\perp \cdot \mathbf{r}} \varphi_n^*(z) [e_x p_x + e_y p_y + e_z p_z] e^{i\mathbf{k}'_\perp \cdot \mathbf{r}} \varphi_{n'}(z) \quad (12)$$

Only the term proportional to e_z yields a contribution at finite frequency. The other terms, proportional to e_x and e_y vanish, except when initial and final states are identical ($n = n'$ and $\mathbf{k}_\perp = \mathbf{k}'_\perp$). The physical meaning of these terms is the free-carrier absorption in the two-dimensional electron gas, which is finite only at zero frequency when no scattering processes are included. This is due to the impossibility of conserving energy and momentum simultaneously during the absorption of a photon by an electron. Thus it is the matrix element

$$\langle n | p_z | n' \rangle = \int dz \varphi_n^*(z) p_z \varphi_{n'}(z) \quad (13)$$

which determines the intersubband absorption in a one-band model. Thus we obtain the result that the electric field of the radiation must have a z component (i.e., a component perpendicular to the semiconductor layers) to couple to the intersubband transition. This is the famous polarization selection rule for intersubband transitions, which, of course, has consequences for how practical experiments are performed. We discuss several frequently employed coupling schemes and sample geometries in Section IV.

Next we briefly note that within the dipole approximation, a different interaction Hamiltonian H' for the electron–photon coupling can be employed, namely, $H' = -e\mathbf{E} \cdot \mathbf{r}$. The r matrix elements are related to the p

matrix elements through

$$\mathbf{p}_{nn'} = im^*\omega_{nn'}\mathbf{r}_{nn'} \tag{14}$$

where $\omega_{nn'} = (E_n - E_{n'})/\hbar$. Note, however, that the use of $e\mathbf{E}\cdot\mathbf{r}$ can lead to wrong results in a system with nonnormalizable, unbounded wave functions, such as in the Kronig–Penney model for superlattices. In this case, the $\mathbf{A}\cdot\mathbf{p}$ interaction should be used.

As in all areas of optical spectroscopy, it is very useful to define the dimensionless oscillator strength $f_{nn'}$ by

$$f_{nn'} = \frac{2}{m^*\hbar\omega_{n'n}}|\langle n|p_z|n'\rangle|^2 = \frac{2m^*\omega_{n'n}}{\hbar}|\langle n|z|n'\rangle|^2 \tag{15}$$

since it facilitates the comparison of transition strengths in different physical systems and also obeys the sum rule

$$\sum_{n'} f_{nn'} = 1 \tag{16}$$

valid for all initial states n and the sum extending over all final states n'. Absorption processes are counted positive, emission processes with a negative sign, which is implicitly taken care of already in the definition in Eq. (15). Sometimes the free-electron mass m_0 is used in Eq. (15) instead of the effective mass m^* (West and Eglash, 1985). The such defined oscillator strenghs are then not of the order of unity for allowed transitions, but rather of the order m_0/m^*, which also has to be substituted for the right-hand side of Eq. (16). This is especially necessary for multiband (or nonparabolic) models, where interband and intersubband transitions cannot be separated in the sum rule (Khurgin, 1993; Sirtori *et al.*, 1994). In a similar manner, the position dependence of the effective mass can be incorporated. It has been shown that m_0/m^* has to be replaced by $\langle n|m_0/m^*(z)|n\rangle$ in this case (Davé and Taylor, 1994); that is, an average of m^* over the ground state wave function must be performed. Of course, the absorption coefficient, if calculated consistently, remains unaffected by these definitions.

It is worth again summarizing the main issue related to the effective-mass approximation (with constant effective mass). As long as m^* is assumed constant and z-independent in all formulas known from elementary quantum mechanics, m_0 can be substituted for m^* and one can work with the envelope function alone. The incorporation of the position (Davé and Taylor, 1994) or energy (Sirtori *et al.*, 1994) dependence (nonparabolicity) requires more sophistication.

Having achieved a very simple form of the matrix element, we can proceed to evaluate the absorption coefficient α. The absorption coefficient is usually defined through the ratio of the absorbed electromagnetic energy per unit time and volume, $\hbar\omega \cdot W_{if}/V$, and the intensity of the incident radiation, $I = (1/2)\varepsilon_0 c\eta E_0^2$, summed over all occupied initial and empty final states. Here η denotes the refractive index of the material, for the moment taken to be real and constant. This leads to a dimension of inverse length for α. In the case of quasi-two-dimensional layers, this concept must be modified, and we have several possible ways to do that. The most natural way is to define a dimensionless absorption coefficient, α_{2D}, by dividing through the area A instead of the volume. Here α_{2D} is simply a measure of the fraction of electromagnetic energy absorbed by a 2D layer. When we also allow for stimulated emission in addition to absorption, sum over all possible combinations of initial and final states, and take into account their occupation via the Fermi–Dirac distribution function, we can write the very general expression for the absorption coefficient

$$\alpha_{2D} = \frac{\hbar\omega}{IA} \sum_{n,n'} \sum_{\mathbf{k}_\perp} \frac{2\pi}{\hbar} |\langle n|(e/m^*)\mathbf{A}\cdot\mathbf{p}|n'\rangle|^2 [f(E_n(\mathbf{k}_\perp)) - f(E_{n'}(\mathbf{k}_\perp))] \times \delta(E_{n'}(\mathbf{k}_\perp) - E_n(\mathbf{k}_\perp) - \hbar\omega) \qquad (17)$$

Now we express both I and $\mathbf{A}$ by the electric field amplitude E_0 (which then cancels) and change the summation into a two-dimensional integration in the usual way (including a factor of 2 for the spins).

$$\alpha_{2D} = \frac{\pi e^2}{\varepsilon_0 c\eta\omega m^{*2}} \sum_{n,n'} \frac{2}{(2\pi)^2} \int d^2k_\perp |\langle n|p_z|n'\rangle|^2 [f(E_n) - f(E_{n'})] \cdot \delta(E_{n'} - E_n - \hbar\omega) \qquad (18)$$

Here we have already accounted for the polarization selection rule and suppressed the k-dependence of the energies E_n and $E_{n'}$. This formula can be significantly simplified, if we assume a parabolic in-plane dispersion. Then the two-dimensional integration over the Fermi–Dirac distributions (where E_F is the Fermi energy and k is Boltzmann's constant) can be performed analytically (which is possible only in 2D!) and we get the final result

$$\alpha_{2D} = \frac{e^2 kT}{2\varepsilon_0 c\eta\hbar} \sum_{n,n'} f_{nn'} \ln\left[\frac{1 + \exp((E_F - E_n)/kT)}{1 + \exp((E_F - E_{n'})/kT)}\right] \frac{\Gamma/\pi}{(E_{n'} - E_n - \hbar\omega)^2 + \Gamma^2} \qquad (19)$$

We have also replaced the energy-conserving δ function by a normalized Lorentzian with half width at half maximum (HWHM) of Γ and the momentum matrix element by the oscillator strength using Eq. (15) and $\omega_{n'n} \approx \omega$, so that the prefactor in Eq. (19) becomes independent of ω. (Note that problems can arise in this connection for broad absorption lines such that $\hbar\omega_{n'n} \approx \Gamma$. This was thoroughly discussed by Cohen-Tannoudji *et al.*, 1989).

A main feature of intersubband transitions is their δ-function-like density of states, which is a consequence of the same curvature of the initial and final subband (corrections due to nonparabolicity will be discussed in Section VII). Mathematically, this is reflected through the cancellation of the $\hbar^2\mathbf{k}_\perp^2/2m^*$ terms in the energy conserving δ function (Eq. (17)). This is why intersubband transitions largely behave like atomic transitions, although we have a two-dimensional rather than a zero-dimensional system.

At zero temperature, where the ln approaches $(E_F - E_1)/kT$ (assuming only one subband is occupied) a particularly simple result is obtained, which can be used to estimate the peak absorption strength of a particular structure with certain carrier density, oscillator strength and linewidth. We also leave out the sum over all transitions with the exception of $1 \rightarrow 2$, which is usually the most important one:

$$\alpha_{2D}(T=0) = \frac{n_s e^2 \hbar}{2\varepsilon_0 c\eta m^*} f_{12} \frac{\Gamma}{(E_2 - E_1 - \hbar\omega)^2 + \Gamma^2} \tag{20}$$

Here n_s is the areal electron concentration. At the resonance, $E_2 - E_1 = \hbar\omega$, this yields the useful formula for GaAs (with $m^* = 0.068\ m_0$ and $\eta = 3.4$)

$$\alpha_{2D} = 0.15\ n_s[10^{12}\,\mathrm{cm}^{-2}] \frac{f_{12}}{\Gamma[\mathrm{meV}]} \tag{21}$$

Note, however, that this is valid only as long as $\alpha_{2D} \ll 1$ (strictly when $\alpha_{2D} \cdot \sin^2\theta/\cos\theta \ll 1$, where θ is the angle between the growth axis and the light propagation direction; for more details, see later), which is, fortunately, fulfilled for nearly all realistic cases. From Eq. (21) we see that a 2D layer with $n_s = 10^{12}\,\mathrm{cm}^{-2}$, $f_{12} = 1$ and $\Gamma = 1$ meV, which is about what can be achieved to date, leads to $\alpha_{2D} = 0.15$. If $\alpha_{2D} \geqslant 1$ (which actually happens in cyclotron resonance on high-mobility 2D electron gases), the simple linear absorption theory breaks down and we must treat the 2D system as a highly conducting, quasi-metallic sheet with a frequency-dependent surface conductivity σ^{2D}, and we must determine the transmitted intensity using the correct electromagnetic boundary conditions. The microscopic properties

are then included in σ^{2D}. For normal incidence this results to (Höpfel and Gornik, 1986).

$$T = \frac{4\eta_1\eta_2}{|\eta_1 + \eta_2 + (\sigma^{2D}/\varepsilon_0 c)|^2}$$

$$R = \frac{|\eta_1 - \eta_2 - (\sigma^{2D})/\varepsilon_0 c)|^2}{|\eta_1 + \eta_2 + (\sigma^{2D})/\varepsilon_0 c)|^2} \quad \text{and} \quad A = 1 - R - T = \frac{4\eta_1(\mathrm{Re}\sigma^{2D}/\varepsilon_0 c)}{|\eta_1 + \eta_2 + (\sigma^{2D}/\varepsilon_0 c)|^2} \tag{22}$$

Here T, R, and A are the transmission, reflection, and absorption, respectively, and η_1 and η_2 are the refractive indices before and after the active layer. For $\sigma^{2D} \ll \varepsilon_0 c = (377\Omega)^{-1}$ and $\eta_1 = \eta_2 = \eta$ we get $A = \mathrm{Re}\sigma^{2D}/\varepsilon_0 c\eta$. We show later that this is identical to the preceding α_{2D}, in Eq. (20), when $\sigma(\omega)$ is calculated assuming a Drude–Lorentz oscillator.

It is generally advisable to work with the dielectric function $\varepsilon(\omega)$ or the conductivity $\sigma(\omega)$ instead of the absorption coefficient, whenever the electromagnetic properties of a sample are to be calculated consistently (see Section IV) or many-body effects in the absorption are to be taken into account (see Section VII). The relation

$$\varepsilon(\omega) = 1 + i\frac{\sigma}{\varepsilon_0 \omega} \tag{23}$$

(for now neglecting the contribution from the background dielectric constant) known from three dimensions has to be modified in two dimensions to

$$\varepsilon(\omega) = 1 + i\frac{\sigma^{2D}}{\varepsilon_0 \omega L_{\mathrm{eff}}} \tag{24}$$

where σ^{2D} is again the 2D (areal) conductivity and L_{eff} is some effective thickness of the quasi-2D system. Using the relation between the optical constants

$$\mathrm{Im}(\varepsilon) = 2\,\mathrm{Re}(\eta)\,\mathrm{Im}(\eta) \tag{25}$$

and

$$\alpha_{3D} = 2\frac{\omega}{c}\mathrm{Im}(\eta)$$

where η is the refractive index, we obtain

$$\alpha_{3D} = \frac{\omega}{c\,\mathrm{Re}(\eta)}\,\mathrm{Im}(\varepsilon) = \frac{\mathrm{Re}(\sigma^{2D})}{\varepsilon_0 c\,\mathrm{Re}(\eta) L_{\mathrm{eff}}} =: \frac{\alpha_{2D}}{L_{\mathrm{eff}}} \tag{26}$$

Inserting here a Drude–Lorentz oscillator with oscillator strength f_{12} and damping constant $\gamma(=\Gamma/\hbar)$,

$$\sigma^{2D}(\omega) = \frac{n_s e^2 f_{12}}{m^*} \frac{-i\omega}{\omega_{21}^2 - \omega^2 - 2i\gamma\omega} \tag{27}$$

and approximating the denominator with the near-resonance expression $(\omega_{21} - \omega)(\omega_{21} + \omega) \approx 2\omega(\omega_{21} - \omega)$, we obtain

$$\mathrm{Re}\sigma^{2D}(\omega) = \frac{n_s e^2 f_{12}}{2m^*} \frac{\gamma}{(\omega_{21} - \omega)^2 + \gamma^2} \tag{28}$$

which is exactly equivalent to Eq. (20). For more detailed discussion, see Section IV.

In the discussion up to here we have pretended that one can simply shine light through a 2D system and get intersubband absorption according to Eq. (19). However, the polarization selection rule dictates that there must be a component of the electric field that is perpendicular to the 2D layers (z direction) to get coupling of the radiation to the intersubband transition. Obviously this is not the case for normal-incidence radiation. Therefore, experimentalists have used other geometries to obtain a finite coupling and thus a finite absorption. These geometries and their theoretical description will be discussed in more detail in Section IV. Here we consider only the simplest method, namely, oblique incidence of the radiation (see Fig. 2). Denoting the angle between the growth axis (z direction) and the propagation direction of the optical beam with θ, the electric-field component interacting with the intersubband transition is $E_z = E_0 \sin\theta$, which gives a factor $\sin^2\theta$ for the absorbed intensity. However, the effective interaction length of the radiation with the quantum well is then increased by $1/\cos\theta$, so α_{2D} in Eqs. (19)–(21) must be multiplied by $\sin^2\theta/\cos\theta$. Finally, if we are dealing with a multi-quantum-well (MQW) system of N quantum wells, the transmitted intensity will be proportional to $\exp(-N\alpha_{2D}\sin^2\theta/\cos\theta)$. Experimentally, one usually derives the absorption ("absorbance") from the transmission by *absorbance* $= -\log($*transmission*$)$, and proper normalization to obtain a flat baseline.

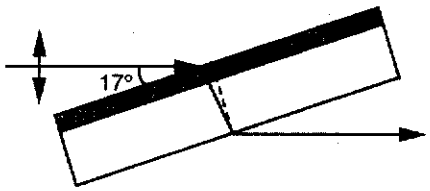

FIG. 2. Oblique-incidence geometry. Here the radiation is incident in Brewster's angle (73° for GaAs with $\eta = 3.3$), resulting in $\theta = 17° = 90° - 73°$.

In MQWs it is common to define a three-dimensional absorption coefficient α_{3D} with dimensions in inverse centimeters. This can be achieved by simply dividing α_{2D} by d, the MQW period. Yet we must recognize that α_{3D} then becomes dependent on the barrier thickness. This concept becomes more useful (and even necessary) when the barriers are thin (for strongly coupled superlattices). In this case, one can actually proceed just like for bulk material and extend the integration in Eqs. (17) and (18) over k_x, k_y, and k_z, leading to a three-dimensional absorption coefficient in the most natural way. We come back to this point in Section VI on superlattices. A third alternative definition of an α_{3D} that is sometimes used in the literature is obtained through normalizing α_{2D} by the quantum well thickness.

III. The Symmetric Quantum Well

In this section, we discuss in more detail the properties of a single, symmetric quantum well, with both infinitely high barriers and finite barriers. Especially the case of the infinite quantum well is very instructive, since all the energy levels, wave functions, and matrix elements can be easily calculated analytically.

For an infinitely deep quantum well (i.e., with a potential that is zero from $z = 0$ to $z = L$ and infinity everywhere else), the following eigenvalues and envelope wave functions are obtained

$$E_{n,\mathbf{k}_\perp} = \frac{n^2\pi^2\hbar^2}{2m^*L^2} + \frac{\hbar^2\mathbf{k}_\perp^2}{2m^*} \tag{29}$$

$$\varphi_n(z) = \sqrt{\frac{2}{L}}\sin\left(\frac{n\pi z}{L}\right) \tag{30}$$

The momentum matrix element between the ground state ($n = 1$) and the $n = 2$ excited subband can be calculated explicitly to yield

$$|\langle 1|p_z|2\rangle| = \frac{8\hbar}{3L} \tag{31}$$

which results in an oscillator strength

$$f_{12} = \frac{256}{27\pi^2} = 0.96 \tag{32}$$

where Eq. (29) must be used for the energy difference $E_2 - E_1 = \hbar\omega_{21}$. The oscillator strength has the nice feature of being independent of the quantum well width. The same expression for the oscillator strength can be obtained by using the dipole matrix element

$$|\langle 1|z|2\rangle| = \frac{16L}{9\pi^2} \tag{33}$$

It is even possible to derive a general expression for all allowed transitions in an infinite quantum well:

$$f_{mn} = \frac{64}{\pi^2} \frac{n^2 m^2}{(n^2 - m^2)^3} \tag{34}$$

Only parity changing (odd–even or even–odd) transitions are allowed due to the inversion symmetry of the potential. As further examples, $f_{14} = 0.03$, $f_{23} = 1.87$, and so on. Thus, we see that by far the strongest transition is the one with $n = m + 1$. The higher ones carry a smaller and smaller oscillator strength. We can also see that transitions between excited states are much stronger than transitions from the ground state, a fact well known from atomic physics and necessary to full the oscillator sum rule. For large n, it can actually be shown using Eq. (34) that $f_{n,n+1}$ increases linearly with n. In Fig. 3 an infinite square quantum well is sketched together with the allowed intersubband transitions.

A more realistic description must include the finite depth of the quantum well. This can be done either analytically (in the case of a symmetric square well) or numerically with the transfer matrix method, as mentioned in Section II. In general, the subband energies will be somewhat lower than for a structure having the same width, but infinite barriers and the wave functions penetrate into the barrier. But no matter how low the barriers and

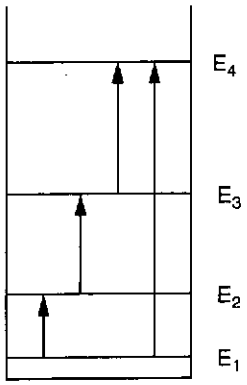

FIG. 3. Possible intersubband transitions in an infinite quantum well; only transitions with a change in parity are allowed.

how thin the quantum well, for a one-dimensional binding potential there will always be at least one confined state, which is well-known from quantum mechanics. Figure 4 shows a state-of-the-art absorption spectrum of an $In_{0.53}Ga_{0.47}As$–$In_{0.52}Al_{0.48}As$ quantum well (barrier height approximately 500 meV) with two bound states. The measurement here has been performed with the sample prepared in a multipass waveguide geometry (see Section IV) and taking the ratio of the transmission signals of two orthogonal polarizations, where only one polarization has an intersubband-active component (z direction).

In the remainder of this section we look at transitions from the ground state to the continuum in a finite, symmetric QW, which has some practical relevance for infrared detectors. For simplicity, we assume that the QW is reasonably deep so that we can approximate the wave function of the first subband by the infinite-well wave function. Taking the center of the well to be at $z = 0$, we have

$$\varphi_1(z) = \sqrt{\frac{2}{L}} \cos\left(\frac{\pi z}{L}\right) \tag{35}$$

and the continuum wave function is simply written as

$$\varphi_c(z) = \frac{1}{\sqrt{\ell}} \exp(ikz) \tag{36}$$

where we have neglected the effect of the boundaries between the well and

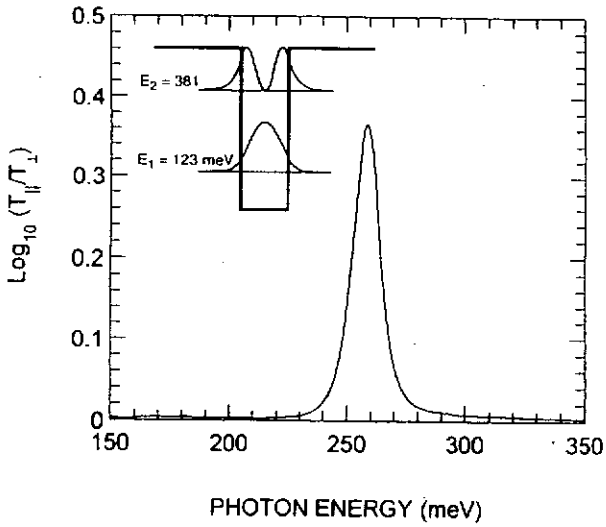

FIG. 4. Absorption spectrum of an $In_{0.53}Ga_{0.47}As$–$In_{0.52}Al_{0.48}As$ quantum well sample with two bound states (width 52 Å) obtained by taking the log of the transmission ratio of the two orthogonal polarizations. The subband levels and squared wave functions are shown in the inset (from Sirtori *et al.*, 1994).

the barrier, which normally give rise to standing-wave (Fabry–Pérot) effects in the continuum, and ℓ is the normalization length of the continuum. With these wave functions, the momentum matrix element can be calculated to give (Bastard, 1988)

$$\langle \varphi_1 | p_z | \varphi_c \rangle = \sqrt{\frac{2}{L\ell}} \cos\left(\frac{kL}{2}\right)\left[\frac{1}{k+\pi/L} - \frac{1}{k-\pi/L}\right]\hbar k \tag{37}$$

Summing over the continuum states (k-integration) leads to the 2D absorption coefficient

$$\alpha_{2D} = \frac{n_s e^2}{2\varepsilon_0 c\eta\omega} k_0 L \cos^2(k_0 L/2)\left[\frac{1}{k_0 L + \pi} - \frac{1}{k_0 L - \pi}\right]^2 \tag{38}$$

with $k_0^2 = (2m^*/\hbar^2)(\hbar\omega - V_b + E_1)$ and V_b is the barrier height. This function yields a steep rise at the ionization threshold $\hbar\omega = V_b - E_1$, and a more slowly decaying tail on the high-frequency side. Liu (1993) performed an exact analytical calculation of the absorption of a finite, symmetric QW. He

showed that the inclusion of a broadening parameter Γ removes all divergences and there is a smooth transition between bound-to-bound and bound-to-continuum transition. This is shown in Fig. 5, where the absorption is plotted for a QW with varying thicknesses (with $\Gamma = 5$ meV). For $L < 49$ Å the QW binds only one state, and the three curves for $L = 47$, 41, and 35 Å corresponds to continuum transitions. Only a decrease of the peak absorption and an asymmetric broadening is observed. Liu (1993) compared this calculation with experimental data of Asai and Kawamura (1990) and found good agreement. Figure 6 shows the bound-continuum absorption spectrum of a narrow (30 Å) $In_{0.53}Ga_{0.47}As$–$In_{0.52}Al_{0.48}As$ multiquantum well that has only one bound state.

Standing-electron-wave effects in the continuum can be used intentionally to drastically modify the absorption of the quantum well structure. For example, so-called Bragg confinement (Lenz and Salzman, 1990; Capasso *et al.*, 1992, Sirtori *et al.*, 1992) can be achieved by embedding a quantum well with one bound stated is into a superlattice, where the superlattice has to act like a quarter-wave dielectric stack for electrons. This is discussed more extensively in Chapter 2 of the present volume.

Dupont *et al.* (1995) have observed a photocurrent due to transitions into the continuum of a multi-QW structure, which was excited by simultaneous

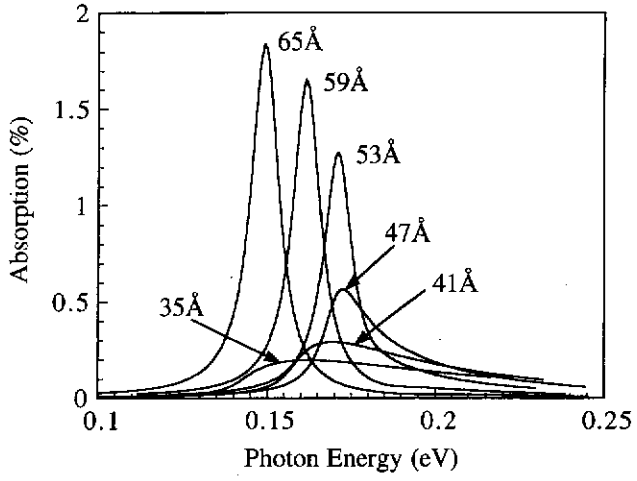

FIG. 5. The calculated intersubband absorption spectrum of a single GaAs–$Al_{0.3}Ga_{0.7}As$ QW plotted for different quantum well thicknesses as indicated. The second subband is bound only for thicknesses greater than 49 Å, otherwise the absorption is to the continuum (after Liu, 1993).

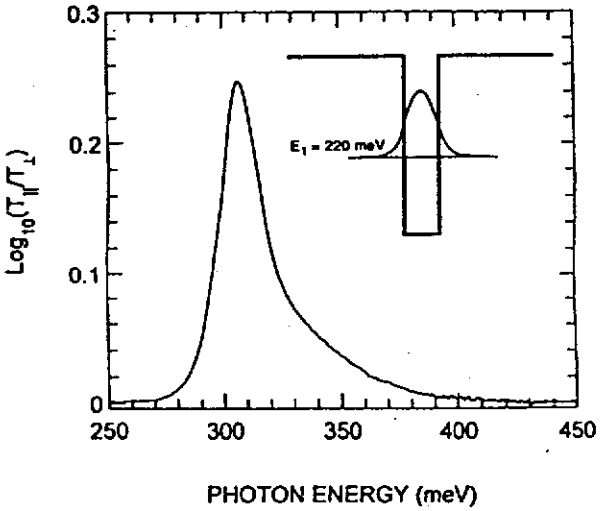

FIG. 6. Bound-to-continuum absorption spectrum of a 30-Å-wide $In_{0.53}Ga_{0.47}As$–$In_{0.52}Al_{0.48}As$ quantum well sample with one bound state obtained by taking the log of the transmission ratio of the two orthogonal polarizations. The bound state with its squared wave function is shown in the inset (from Sirtori *et al.*, 1994).

one-photon and two-photon absorption at a wavelength of 5.3 and 10.6 μm, respectively. Since the 5.3-μm radiation was generated through frequency doubling from the 10.6-μm radiation, the two waves had a constant but tunable phase relation. They were able to coherently control the direction of the induced photocurrent by changing the phase difference.

Before we proceed further and discuss other types of quantum wells, it seems appropriate to devote a section to some experimental techniques commonly employed for the study of intersubband transitions.

IV. Experimental Geometries and Their Electromagnetics

The specific nature of intersubband transitions—that is, the selection rule requiring an electric-field component perpendicular to the QW layers—necessitates the use of nonstandard geometries to perform absorption experiments, which in turn require a careful consideration of the electromagnetics (i.e., the spatial distribution of the electromagnetic field in the sample). These two issues are the topic of this section.

In a standard transmission geometry, where the light is incident perpendicular to the sample surface, the electric field has components only in the QW plane and intersubband transitions cannot be induced (at least in the simple band structure discussed so far; exceptions are discussed in Sections VIII and IX). The simplest way to overcome this problem is to shine the light on the sample at an oblique angle of incidence. A frequent choice is Brewster's angle (73° for GaAs with a refractive index of $\eta = 3.3$) (see Fig. 2 in Section II), at which the reflection on the surfaces also vanishes (West and Eglash, 1985; Levine *et al.*, 1987). However, due to the high refractive index of most semiconductors, the angle of incidence within the sample is still rather small ($\theta = 17°$ for GaAs) leading to a small intersubband-active electric-field component E_z. The effective coupling factor $\sin^2\theta/\cos\theta$ in this case is given by $1/\eta\sqrt{\eta^2+1} \approx 0.09$ for GaAs. Due to this small coupling, the Brewster-angle geometry is normally used only for relatively highly doped multi-QW systems. An advantage, however, is the very well defined electric-field strength and intensity at the QW position.

For samples exhibiting weaker absorption (e.g., for lower doping, single QWs or large linewidths), several types of waveguide geometries have been devised by various authors, where the incident radiation undergoes several total internal reflections in the sample (Fig. 7). In these geometries the light is coupled into the sample at the edges, which are wedged at a certain angle α. The number of passes through the active layer, M (=twice the number of reflections), is determined by the length (L_{substr}) and thickness (D_{substr}) of the substrate, $M = L_{\text{substr}}/(D_{\text{substr}} \cdot \tan\theta)$. For a sample with 0.5 mm thickness, 5 mm length, and an angle of $\theta = 45°$ one obtains five total internal reflections at each surface ($M = 10$), leading to a coupling strength of $10 \times \sin^2 45°/\cos 45° \approx 7$. Two frequently employed types of waveguides are shown in Figs. 7a and 7b. The geometry (Fig. 7a) (Levine *et al.*, 1987; Kane *et al.*, 1988; Wieck *et al.*, 1988) has the advantage that the surface reflection loss of the incident light is the same for both orthogonal polarizations, which is convenient for taking reference spectra. (The TM or *p* polarization is the one that couples to the intersubband transition, since the electric field contains a *z* component, whereas the TE or *s* polarization does not couple, since the electric field lies in the QW plane.) A slight drawback is the displacement of the beam after traversing the sample. In geometry (Fig. 7b) (Hertle *et al.*, 1991; Fromherz *et al.*, 1994) the surface reflections are different for both polarizations, but the beam is not displaced. The internal angle θ is given by $\theta = \alpha + \arcsin[\sin(90° - \alpha)/\eta]$, and when α is chosen so that $\theta = 90° - \alpha$ ($\alpha = 38°$, $\theta = 52°$ for GaAs), the propagation direction inside the sample is parallel to one of the wedged facets. Variations of these geometries contain a two-pass arrangement, where either the sample is so short (e.g., an etched mesa structure, Capasso *et al.*, 1994, see Fig. 7c), or the

FIG. 7. Sev
absorption are
Two types of t
text.

wedge angle
the light un
the intersub
the effective

To calcul
multipass wa
at the bound
interface. D
standing-wa
the *z* directi
Thus it is cl
(=*Nd*) is lar
wavelength i
out and the
work. As an e
intensity patt
hand, a mul
thickness (we
preceding co

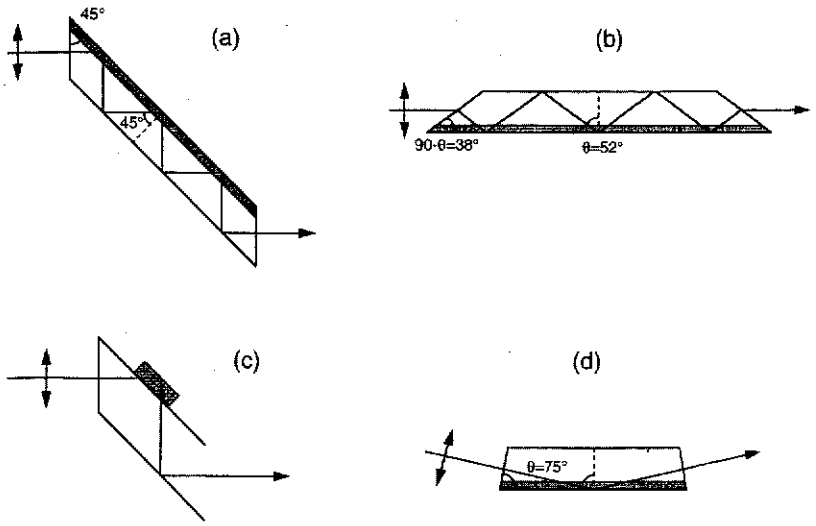

FIG. 7. Several common waveguide geometries for the measurement of intersubband absorption are shown. Top (a) and (b): two types of multipass waveguides. Bottom (c) and (d): Two types of two-pass waveguides; (c) shows an etched mesa structure. For a discussion, see text.

wedge angle α is so large (nearly 90°, Seilmeier *et al.*, 1987, see Fig. 7d) that the light undergoes only one total reflection. This is especially useful when the intersubband transition is pumped with a laser and one wants to know the effective light intensity in the QWs accurately.

To calculate the absorption of an electromagnetic wave in such a multipass waveguide structure, it is essential to consider what is happening at the boundary of the semiconductor slab, that is, at the semiconductor–air interface. Due to the interference of the incident and reflected wave, a standing-wave intensity pattern of the field component E_z will form along the z direction having a periodicity $\lambda/2\eta\cos\theta$ (Vodopyanov *et al.*, 1997). Thus it is clear that only as long as the total thickness of the active layer ($=Nd$) is larger than this standing-wave period (or essentially the resonant wavelength in the sample, λ/η), the nodes and antinodes are largely averaged out and the preceding simple approach for calculating the absorption will work. As an example, if the resonant wavelength is 10 μm, the corresponding intensity pattern has a period of 2.15 μm (for $\eta = 3.3$, $\theta = 45°$). On the other hand, a multiquantum well system with $N = 100$ periods of $d = 300$ Å thickness (well plus barrier width) yields a total thickness of 3 μm, and the preceding condition is satisfied. If this condition is not fulfilled, as is

obviously the case in a single quantum well, the absorption strongly depends on the position of the QW relative to the intensity nodes and antinodes.

Let us now consider a QW near the surface—that is, near the semiconductor–air interface (see Fig. 8)—and the corresponding electromagnetic boundary conditions for light incident from inside the semiconductor at an angle of $\theta = 45°$. According to Fresnel's formulas, the totally reflected wave will undergo a phase shift of 168° (for $\eta = 3.3$), which corresponds to an almost complete phase reversal, and produces a node in the perpendicular field component E_z. Therefore there is virtually no interaction of the light with the intersubband transition, when the active layer is thin in the preceeding sense. This can, of course, be remedied, when the QW is moved away from the surface to the next antinode; that is, by half a period of the intensity pattern. There is, however, another method, which was first discussed by Kane *et al.* (1988) for quantum wells, but has been routinely used in the seventies in connection with Si inversion and accumulation layers (Kamgar *et al.*, 1974; Kneschaurek *et al.*, 1976). When a metallic layer is deposited on the sample surface, the boundary conditions are changed, leading to a maximum of the field component E_z at the semiconductor-metal interface, as illustrated in Fig. 8.

Quantitatively, the transmission through such a multipass waveguide structure can be approximated by

$$T \cong \exp(-C \cdot M \cdot N \cdot \alpha_{2D} \cdot \sin^2\theta/\cos\theta) = \exp\left(-C\frac{L_{substr}}{D_{substr}} N \cdot \alpha_{2D} \cdot \sin\theta\right) \quad (39)$$

Here L_{substr} and D_{substr} are the length and thickness, respectively, of the sample including substrate, N is the number of multiquantum well periods,

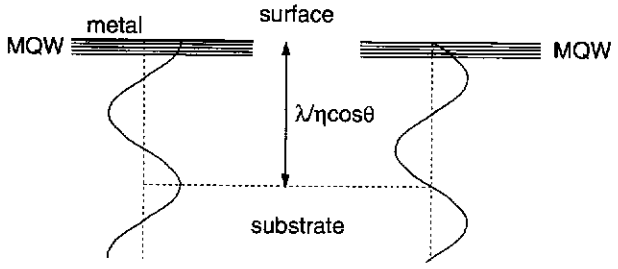

FIG. 8. Sketch of the electric-field distribution for a multiquantum well structure on a substrate, with (left) or without (right) a metal coating of the surface. A standing-wave pattern with period $\lambda/\eta \cos\theta$ is formed that has a crest or node at the surface, respectively.

M is the number of passes through the active layer, and C is a coupling factor between 0 and 2, which depends on the active layer thickness Nd relative to the wavelength λ/η and on the position of the QWs with respect to the standing-wave pattern.

For a thick MQW layer ($Nd > \lambda/\eta$), where the standing-wave effect is averaged out, $C = 1$, identical to what one gets in a simple traveling-wave picture. For a thin MQW layer ($Nd \ll \lambda/\eta$), C depends on the location of the active layer relative to the electric-field nodes and crests. If the MQW is in a crest of the electric-field pattern (for example, near the metal-coated surface), $C = 2$, whereas $C \ll 1$ if the MQWs are located at an electric-field node (for example, near the uncoated surface).

In summary, at a semiconductor–air interface the E_z component is nearly zero and the in-plane component E_{xy} is finite, whereas at a semiconductor–metal interface, the E_z component is finite (even enhanced) and the E_{xy} components are shorted out to zero. Therefore, intersubband absorption experiments with a small number of QW periods located near the surface require a metal coating of the surface.

Note that for *nonlinear* experiments (such as saturation measurements) even for a thick MQW layer, the local peak intensity is crucial, which can be a factor of four larger than in the traveling-wave picture (Vodopyanov *et al.*, 1997).

For a consistent treatment of the waveguide transmission, the electromagnetic wave propagation through the multilayer stack of the sample should be calculated using proper expressions for the dielectric functions for each layer as well as the electromagnetic boundary conditions between the layers. The quantity of interest describing the absorption is then the reflectivity at the semiconductor–air or semiconductor–metal interface. The numerics can be done, for example, using a transfer-matrix method (Harbecke, 1986; Terzis *et al.*, 1990). In this way, the substrate and (un)doped buffer or cap layers can be included in addition to the active MQW layer as well as a possible metallic layer on the surface, which may result in Fabry–Pérot-type fringes. For the substrate, buffer and cap layers, a classical Drude expression for $\varepsilon(\omega)$ can be employed (plus a phonon term, if any phonon resonances are close in frequency). The metal can be described in a similar way. The active MQW layers can be treated as a single layer (effective medium approximation), since the individual quantum well thicknesses are two orders of magnitude smaller than the wavelength of the light, and can be described with a simple anisotropic plasma model with an oscillator in the z direction (compare Eq. (27)) (Chen *et al.*, 1976; Kane *et al.*, 1988)

$$\varepsilon_{zz} = \varepsilon_\infty - \frac{\varepsilon_\infty f_{12}\omega_p^2}{\omega^2 - \omega_{21}^2 + 2i\omega\gamma} \quad \text{and} \quad \varepsilon_{xx} = \varepsilon_{yy} = \varepsilon_\infty - \frac{\varepsilon_\infty \omega_p^2}{\omega^2 + i\omega/\tau} \tag{40}$$

Here γ is the HWHM of the intersubband absorption, τ is a in-plane scattering time, and ω_p is the two-dimensional effective plasma frequency, given by $\omega_p = \sqrt{(n_s e^2/\varepsilon_\infty \varepsilon_0 m^* L_{\text{eff}})}$, where L_{eff} is an effective quantum well thickness (see also Section VII, Eq. (58)).

Dahl and Sham (1977) and Nakayama (1995, 1977) carefully considered the nonlocal electromagnetics of a quasi-2D electron system. Liu (1994) has even included retardation effects. In a nonlocal effective-medium approach for multiquantum well systems, Zaluzny and Nalewajko (1997, 1998) derive the dielectric tensor component ε_{zz} from the two-dimensional dynamic conductivity of each individual quantum-well layer. The conductivity σ^{2D} can be calculated microscopically, including depolarization shift and all many-body effects (see Section VII) properly, and with the resulting dielectric tensor, the transmission can be calculated. It turns out that not only the absorption strength but also the absorption frequency and the line shape may depend on the electromagnetic boundary conditions (semiconductor–air or semiconductor–metal); a metallic surface shifts the absorption to higher frequencies (related to this is the so-called Berreman effect, an absorption occurring in thin films at the LO-phonon frequency (see Berreman, 1963; Harbecke *et al.*, 1985). In general, the MQW absorption is usually proportional to $\text{Im}(-1/\varepsilon_{zz})$, and not to $\text{Im}(\varepsilon_{zz})$. In many cases, however, especially if the absorption of each individual QW is small, the transmission can be well approximated by Eq. (39).

Note that a detailed analysis of intersubband absorption strength, energy, and lineshape must include both many-body effects (see Section VII) and electromagnetics. The level of sophistication of the theoretical description must be chosen depending on the sample structure, the geometry, and the absorption strength.

A number of other geometries have been used to excite intersubband transitions, including a type of transmission line arrangement. Here the light is coupled directly into a cleaved facet of the semiconductor slab, which must be covered by a metal for the reasons already discussed. This technique has mostly been employed in the far-infrared spectral range ($\lambda > 50\,\mu$m), for example, in the earliest experiments on Si-MOS (metal-oxide semiconductor) accumulation and inversion layers (Kamgar *et al.*, 1974; Kneschaurek *et al.*, 1976), and theoretically discussed by Nakayama (1977) and Zaluzny (1996). It has also been used in intersubband absorption experiments performed with a far-infrared free-electron laser (Heyman *et al.*, 1994). Note that an experimentally relevant 3D absorption coefficient can be obtained here by dividing α_{2D} by the sample thickness, which is identical to the second expression in Eq. (39) for $\theta = 90°$. In another method, a Si or Ge prism is attached to the substrate and the radiation is coupled into the sample through the prism, thus avoiding refraction at the semiconductor–

air interface and retaining a large E_z component (McCombe *et al.*, 1979). A particularly elegant and useful way is the so-called "critical incidence coupling" proposed and demonstrated by Keilmann (1994), where radiation is coupled into the sample at the critical angle for total reflection, which forces the *p*-polarized light to be exactly perpendicular to the QW layer.

Finally, a technique that has proven very useful for many applications is the use of a grating coupler, either by etching a grating into the surface of the sample or by depositing a metallic grating. This enables coupling of normal-incidence radiation to the intersubband transitions. Two regimes can be distinguished: When the period of the grating is of the order of the wavelength in the semiconductor, the first diffracted order propagates nearly parallel to the surface, thus providing a large electric-field component E_z (Fig. 9, right). This has been applied in mid-infrared detectors based on intersubband transitions (Goossen and Lyon, 1985; Goossen *et al.*, 1988; Hasnain *et al.*, 1989; Andersson *et al.*, 1991; Andersson and Lundqvist, 1991; Yu *et al.*, 1992; Ralston *et al.*, 1992), and here the light is often incident from the substrate side (reflection grating mode). If, in contrast, the grating period is much smaller than the wavelength of the radiation (Fig. 9, left), which corresponds to a quasi-static rather than the optical regime (the diffracted modes are evanescent and not propagating), the electric-field components in the near field of the (metallic) grating get scrambled and, in particular, a finite component E_z results (Heitmann *et al.*, 1982; Heitmann and Mackens, 1986; Batke *et al.*, 1989; Helm *et al.*, 1991). Nonvertical intersubband transitions with a finite wavevector can also be excited (Heitmann and Mackens, 1986). This regime has mostly been employed for the far-infrared spectral region. Coupling efficiencies up to 30% in the FIR region (Li *et al.*,

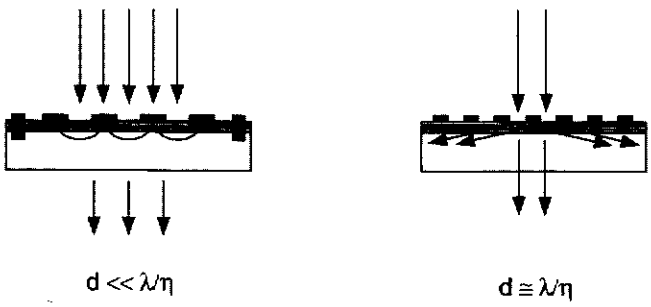

FIG. 9. Grating coupling for intersubband absorption: quasi-static regime (left), where the grating period is much smaller than the wavelength, and diffraction regime (right), where the grating period is of the same order as the wavelength. For the quasi-static regime the electric-field lines in the near field of the grating are sketched.

1990a, 1990b), and up to near unity in the midinfrared (MIR) region (Hasnain *et al.*, 1989; Andersson *et al.*, 1991; Andersson and Lundqvist, 1991) have been reported. The drawback of the grating coupler is that the exact coupling strength and field distribution are not very well known, so the light intensity and absorption strength cannot be quantified very accurately. Furthermore, a reliable theoretical treatment requires a nontrivial electromagnetic calculation (Zheng *et al.*, 1990; Li and McCombe, 1992; Andersson and Lundqvist, 1992; Duboz, 1996; Xu and Hu, 1997; Wendler *et al.*, 1997). Wendler *et al.* (1997) also studied the influence of the grating period on the absorption line shape. In some experiments, the metallic grating coupler was used as a Schottky gate to modulate the electron concentration, which results in increased sensitivity and in absorption spectra free of system artifacts (Helm *et al.*, 1991). The same can be done in waveguide geometry using the metal coating as a Schottky gate (Helm *et al.*, 1993).

V. Asymmetric Quantum Wells

In this section, we discuss quantum wells where the inversion symmetry with respect to the quantum well center is broken by some means. This leads to a relaxation of the selection rules (i.e., transitions between all subbands become allowed). The symmetry breaking can be achieved in several different ways:

1. Applying an electric field along the growth direction.
2. Varying the material (alloy) composition in the QW (e.g., "step quantum well").
3. Two quantum wells with different thicknesses separated/coupled by a thin barrier (asymmetric coupled QW; ACQW).

Of course, all of these three methods can be incorporated at the same time in a single structure, making possible true band-structure engineering. In addition, the symmetry can be broken through asymmetric doping profiles, generating an internal electric field in a quantum well or a heterostructure. An important example for an asymmetric quasi-two-dimensional system is, of course, also the inversion or accumulation layer at the interface of a heterostructure or at the surface in a MOS structure. In this case, the potential near the band edge has an asymmetric triangular shape.

The case of a square quantum well in an electric field F can be treated by second-order perturbation theory, as long as eFL is small compared to the

confinement energy E_1. In this case, the $n = 2$ level remains nearly unperturbed, since it still "feels" mainly the vertical energy barriers, whereas the $n = 1$ level is shifted down by an amount $\Delta E_1 = -C(m^*e^2F^2L^4/\hbar^2)$; that is, it is quadratic in the electric field. Here $C = 0.0022$ is a numerical constant (Bastard *et al.*, 1983). This results in a *blue* shift of the intersubband absorption and corresponds to the quantum confined Stark effect. (Note, however, that this term was originally coined for interband transitions, where the electric field causes a *red* shift of the absorption edge.) This effect can be used for electrooptic devices such as modulators. Experimental results were reported by Harwit and Harris (1987). In the nonperturbative regime of high electric fields and/or large well widths the energy levels can be calculated variationally (Bastard *et al.*, 1983) or by the usual numerical methods such as the transfer matrix (Ahn and Chuang, 1986, 1987). Figure 10 shows the calculated dependence of the subband separation E_{21} on the electric field for a GaAs–$Al_{0.4}Ga_{0.6}As$ QW with three different thicknesses. The initial quadratic behavior turns into linear at higher fields. For extremely high fields ($eFL \gg E_{21}$), E_{21} finally becomes independent of QW thickness, corresponding to the situation of a triangular potential. The conduction-band profile of a 120-Å-wide QW with $F = 100$ kV/cm is shown in Fig. 11. The deformation of the ground-state wave function can clearly be seen, giving rise to a partial transfer of oscillator strength from the $1 \rightarrow 2$ to higher transitions ($1 \rightarrow 3$, $1 \rightarrow 4$, etc.).

A simple way of breaking the symmetry with varying alloy composition is to introduce a potential step into the QW (Yuh and Wang, 1989).

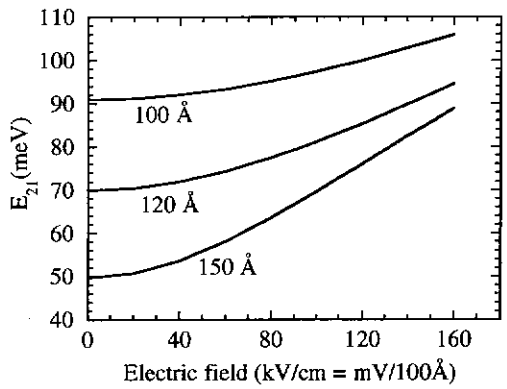

FIG. 10. Stark shift of the intersubband absorption. The energy separation of the two lowest subbands for GaAs–$Al_{0.4}Ga_{0.6}As$ quantum wells with different thicknesses (as indicated) is plotted vs electric field. Note the transition from quadratic to linear behavior.

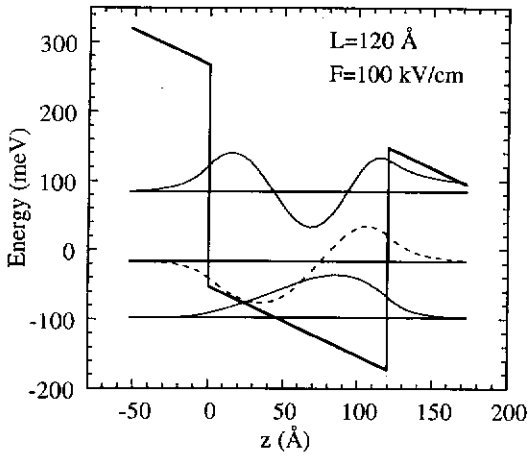

FIG. 11. Potential profile, energy levels, and wave functions of a 120-Å-wide GaAs–$Al_{0.4}Ga_{0.6}As$ quantum well with an electric field of 100 kV/cm.

Absorption experiments in such structures were first performed by Mii *et al.* (1990a), also including an additional electric field (Mii *et al.*, 1990b; see Fig. 12). The absorption spectrum (Fig. 12, right panel) shows two strong peaks, which correspond to the $1 \rightarrow 2$ and $1 \rightarrow 3$ transitions. Depending on the polarity of the applied electric field, a red or blue shift can occur (Yuh *et al.*, 1990). This Stark shift is much stronger than for a square well and nearly linear in the electric field, and is therefore useful for electrooptic modulators. A particularly valuable feature of step quantum wells is that the energy differences $E_3 - E_2$ and $E_2 - E_1$ can be made equal, which opens up the possibility of observing doubly resonant nonlinear optical phenomena (Rosencher and Bois, 1991; Rosencher *et al.*, 1992) such as second-harmonic generation. Such applications are discussed in great detail in Chapter 6 by Sirtori, *et al.*, in the present volume.

The same can be achieved with asymmetric coupled quantum wells. The additional application of an electric field enables one to observe anticrossing between different subbands (Yuh and Wang, 1988) and tuning of the oscillator strengths of the various transitions (Yuh and Wang, 1988; Faist *et al.*, 1993a). Such structures have again been used for giant nonlinear optical effects (Capasso *et al.*, 1994) and they also serve as the active cell in quantum cascade lasers (see Chapter 5 in the present volume). In Figs. 13 and 14 examples for the intersubband absorption in such structures is presented. The InGaAs–InAlAs structure in Fig. 13 has been optimized for doubly resonant nonlinear effects ($E_3 - E_2 \cong E_2 - E_1$), and in the

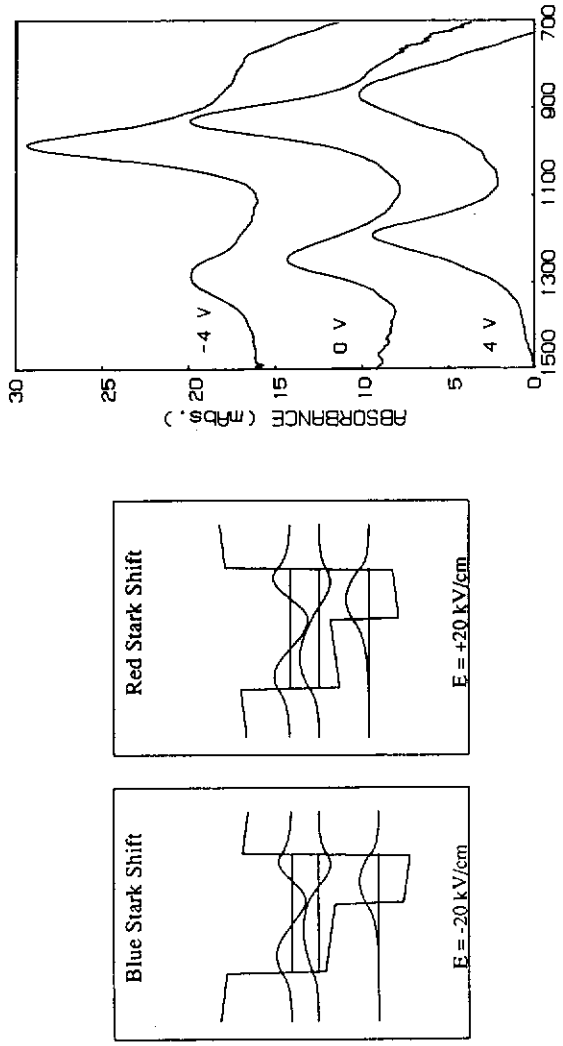

FIG. 12. Stark effect in a GaAs–$Al_{0.18}Ga_{0.82}As$–$Al_{0.44}Ga_{0.56}As$ step-quantum well (width of the GaAs part 60 Å, width of the step 90 Å). Left: Potential profile and wave functions for positive and negative bias. Right: Measured absorption spectrum for positive, zero, and negative bias (from Mii *et al.*, 1990b).

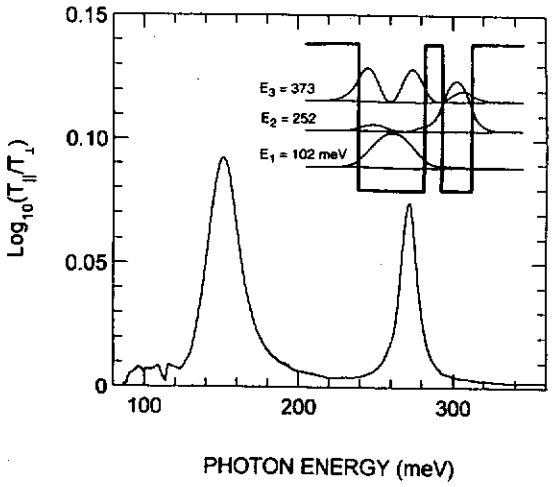

FIG. 13. Absorption spectrum of a strongly asymmetric InGaAs–InAlAs coupled quantum well structure with three bound states (thicknesses are 59, 13, and 24 Å for the first well, barrier, and second well, respectively). The subband levels and squared wave functions are shown in the inset (from Sirtori *et al.*, 1994).

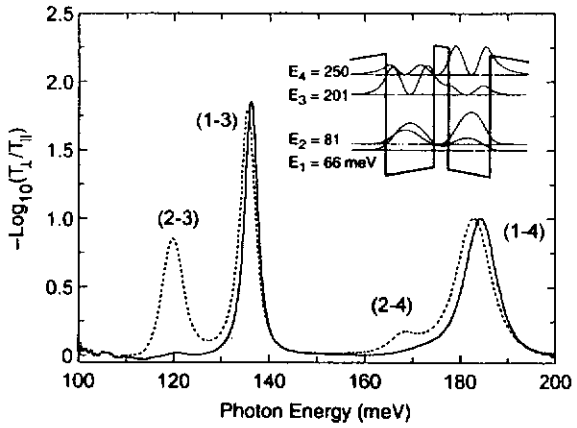

FIG. 14. Absorption spectrum of a weakly asymmetric GaAs–$Al_{0.33}Ga_{0.67}As$ coupled quantum well structure with four bound states (well, barrier, and well thicknesses are 70, 20, and 60 Å). The subband levels and squared wave functions are shown in the inset. The solid curve is recorded at $T = 10$ K, the dashed curve at $T = 60$ K. The relevant transitions are indicated; note the sharpness of the 1–3 transition (from Faist *et al.*, 1994b).

GaAs–AlGaAs structure of Fig. 14 the energy difference $E_2 - E_1$ is so small that the second subband can be populated with increasing temperature, allowing for the observation of the transitions $2 \rightarrow 3$ and $2 \rightarrow 4$.

Finally, we briefly discuss the "oldest" two-dimensional system, the inversion or accumulation layer in a heterostructure or MOSFET. Such a structure is also asymmetric due to the built-in electric field, and intersubband transitions from the ground state to several excited states were observed long before the investigation of quantum wells began. As examples, note the work of Heitmann and Mackens (1986) on Si inversion layers and of Batke *et al.* (1989) and Batke (1991) on GaAs inversion layers; the latter article contains many references to previous investigations. A sketch of a modulation doped GaAs–AlGaAs heterostructure is depicted in Fig. 15 and the intersubband absorption spectrum for such a structure is shown in Fig. 16 for different electron densities. Transitions from the ground state (labeled 0 in Fig. 16) to three excited states can be observed.

To summarize, by introducing several symmetry-breaking elements into a QW structure, the subband energy levels and the resulting absorption properties can be specifically tailored with great design freedom. Such structures can, in some sense, be regarded as artificial, man-made atoms or molecules, although they contain two-dimensional subbands and not really discrete energy levels such as, for instance, quantum dots. But because the joint density of states for intersubband transitions is essentially a δ function (when nonparabolic effects are neglected; see Section VII), quantum wells behave like atoms as far as their intersubband absorption properties are concerned. (One big difference are the short relaxation and dephasing times, as discussed in Section X). This can be exploited for novel, efficient devices like harmonic generators (see Chapter 2 on nonlinear optics in Volume 66) or infrared lasers (Chapter 1 of Volume 66).

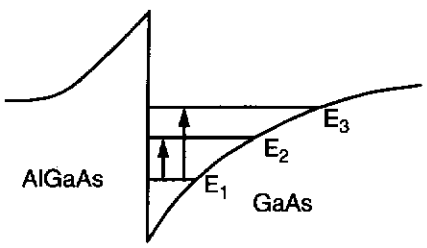

FIG. 15. Conduction-band edge of a modulation doped GaAs–AlGaAs heterostructure. An inversion layer with a two-dimensional electron gas is formed at the interface. Three subbands and possible transitions from the ground state are indicated.

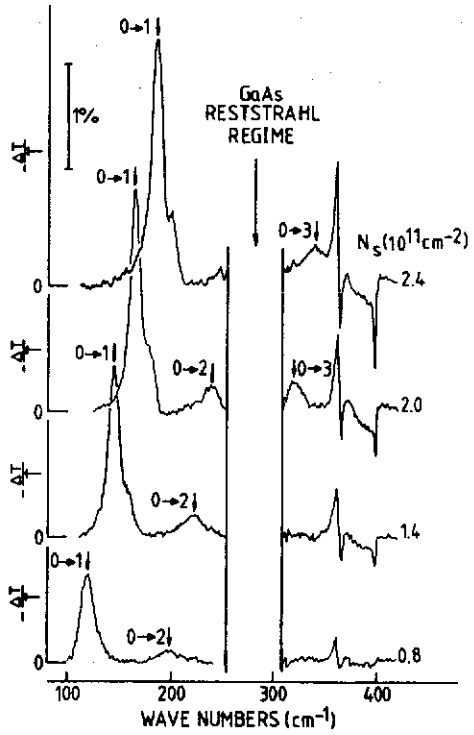

FIG. 16. Intersubband absorption in a gated GaAs–AlGaAs heterostructure. Plotted is the transmission change (relative to the depleted sample) for different electron concentrations as indicated. Transitions to three excited states are observed. (Note that the level numbering starts with 0 in the figure.) In the reststrahlen regime the sample is opaque; the sharp features above 350 cm^{-1} are related to AlAs photons (from Batke *et al.*, 1989).

VI. Multiquantum Wells and Superlattices

From a theoretical point of view, there are some fundamental differences between an isolated system of one or several quantum wells and a periodic sequence of an infinite number of quantum wells (with periodic boundary conditions). In the first case, the energy spectrum always consists of a set of bound states (subbands) and a continuum, where the bound states become more and more closely spaced, when the number of quantum wells becomes larger. For a large number of identical quantum wells, the system is better described by periodic boundary conditions. In this case, one obtains energy bands $E_n(k_z)$, where k_z is the wavevector component parallel to the growth

direction, which is now a good quantum number. This description is especially adequate if the barriers are so thin that strong coupling between different QWs occurs. Such a system is normally called a superlattice and the resulting energy bands are called minibands. There is no essential difference between minibands below and above the top of the barriers. When the barriers are thick (multiquantum well system), the minibands below the top of the barriers are extremely narrow and we have degenerate states localized in each quantum well. Above the top of the barriers we still obtain minibands, as in the case of strong-coupling superlattices, but they are very dense, forming a quasi-continuum. The energy spectrum of a MQW system and a superlattice are schematicaly shown in Fig. 17. For a review article on superlattices, see Helm (1995).

A superlattice with, ideally, an infinite number of periods, can be described by the Kronig–Penney model of a one-dimensional lattice with periodic boundary conditions. The z-dependent part of the envelope wave function can then be written as the product of a Bloch part, which is periodic in the superlattice period, and a slowly varying plane-wave part

$$\varphi_n(z) = e^{ik_z z} u_n(z) \tag{41}$$

where $u_n(z) = u_n(z + d)$ and d is the superlattice period. Note that $u_n(z)$ is different from the $u_v(\mathbf{r})$ in Eq. (1), but there should be no confusion, since

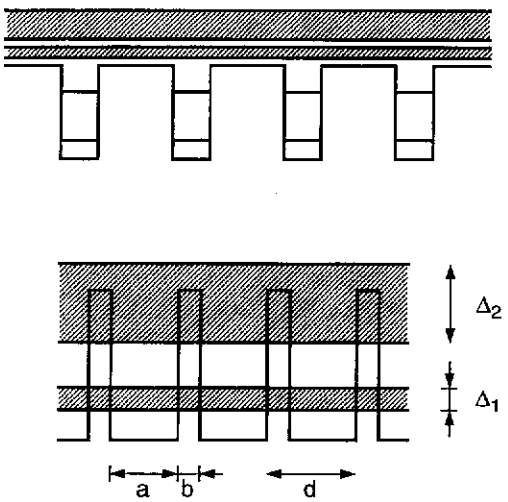

FIG. 17. Schematic conduction band profile and minibands of a multiquantum well structure (top) and a strongly coupled superlattice (bottom).

the two functions never appear in the same equation in this article. The resulting transcendental equation which yields the dispersion $E_n(k_z)$ reads

$$\cos(k_z d) = \cos(\alpha a)\cos(\beta b) - \frac{1}{2}\left(\xi + \frac{1}{\xi}\right)\sin(\alpha a)\sin(\beta b) \qquad (42)$$

where

$$\xi = \frac{m_w^*\beta}{m_b^*\alpha} \quad \alpha = \sqrt{2m_w^* E/\hbar^2} \quad \text{and} \quad \beta = \sqrt{2m_b^*(E - V)/\hbar^2}$$

where a and b are the superlattice well and barrier widths, and m_w^* and m_b^* are the well and barrier effective masses, respectively. In Fig. 18, the first three minibands of a GaAs–$Al_{0.3}Ga_{0.7}As$ superlattice with $a = 75$ Å and $b = 25$ Å are shown. (The $1s$ and $2p_z$ impurity levels, also shown in Fig. 18, are discussed in Subsection 3 of Section XI.) When the widths of the minibands are smaller than the gaps between them (which are, of course, not real gaps, since they contain a constant, two-dimensional density of

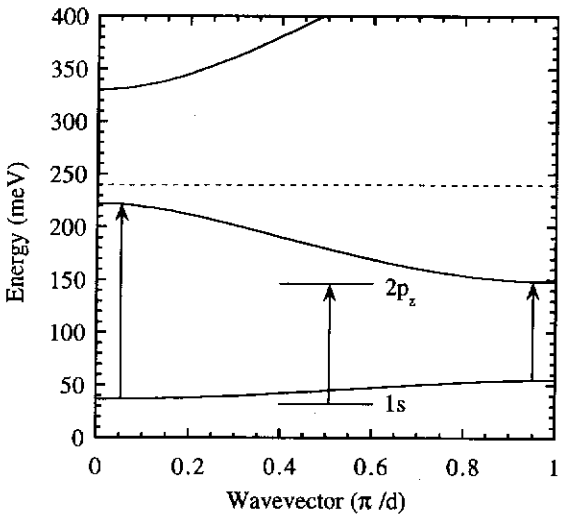

FIG. 18. Calculated miniband dispersions of the three lowest minibands of a GaAs–$Al_{0.3}Ga_{0.7}As$ superlattice with $a = 75$ Å and $b = 25$ Å. The horizontal dashed line indicates the top of the barriers. The $1s$ and $2p_z$ impurity states are also included schematically (for a discussion, see Subsection 3 in Section XI). The interminiband transitions at the center and the edge of the mini-Brillouin zone are indicated as well as the impurity transition.

states), the miniband dispersions can be approximated by the explicit analytic expression

$$E_n(\mathbf{k}) = \varepsilon_n + \frac{\Delta_n}{2}(1 \pm \cos k_z d) + \frac{\hbar^2(k_x^2 + k_y^2)}{2m^*} \tag{43}$$

where the minus sign holds for odd minibands ($n = 1, 3, \ldots$) and the plus sign for even ones ($n = 2, 4, \ldots$). We no longer distinguish between well and barrier effective mass. Equation (43) corresponds to a tight-binding approximation, taking into account the nearest neighboring wells.

The calculation of the absorption coefficient α proceeds in a manner similar to that in Section II for quantum wells, with the difference that we are now dealing with a three-dimensional problem. Therefore α is obtained through integration over k_x, k_y, and k_z, leading to (Helm *et al.*, 1993)

$$\alpha = \frac{e^2 kT}{\varepsilon_0 c\eta\hbar^2\pi m^*\omega}\int_0^{\pi/d} dk_z |\langle 1|p_z|2\rangle|^2 \ln\left[\frac{1+\exp([E_F - E_1(k_z)]/kT)}{1+\exp([E_F - E_2(k_z)]/kT)}\right] \times\left(\frac{\Gamma/\pi}{(E_2(k_z) - E_1(k_z) - \hbar\omega)^2 + \Gamma^2}\right) \tag{44}$$

The $k_x k_y$ integration has already been performed, assuming parabolic bands. The integral over k_z must be evaluated numerically, using the miniband dispersions $E_i(k_z)$ in the Lorentzian. Note that also the matrix elements are k_z-dependent.

Further note that in a periodic system with unbounded wave functions the $\mathbf{A}\cdot\mathbf{p}$ interaction for the electron–photon coupling is preferable over the $e\mathbf{E}\cdot\mathbf{r}$ interaction, since the latter can lead to wrong results (edge terms related to the choice of the unit cell would have to be included; Peeters *et al.*, 1993).

It is now instructive to analyze the different contributions in the preceding formula, namely, the oscillator strength (or the squared matrix element), the Fermi–Dirac thermal occupation factor, and the Lorentzian. Together with the k_z integration the latter is nothing less than the joint density of states (JDOS), which has two singularities at the center ($k_z = 0$) and the edge ($k_z = \pi/d$) of the mini-Brillouin zone with a $1/\omega$ divergence, characteristic of its one-dimensional character. The JDOS for transitions between the two lowest minibands of the above superlattice is shown in Fig. 19 (dotted curve). The singularities are smoothed out by a broadening parameter of $\Gamma = 10$ meV. Note that due to the different curvatures of the bands near $k_z = 0$ and $k_z = \pi/d$, respectively, the shape is not symmetric. (In the tight-binding approximation of (Eq. (43)) the shape can be described

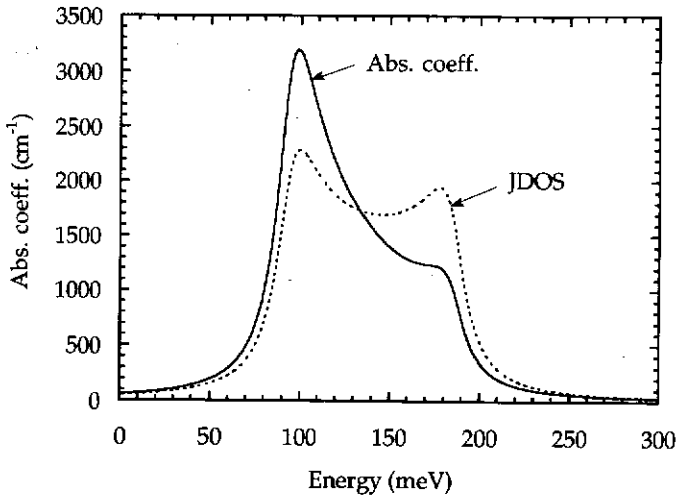

FIG. 19. Calculated JDOS (dotted) and absorption coefficient (solid line) for the above superlattice with $n = 6 \times 10^{17}\,\mathrm{cm}^{-3}$ at $T = 5\,\mathrm{K}$. The units for the JDOS are arbitrary (from Helm *et al.*, 1993).

analytically and turns out to be symmetric (Helm *et al.*, 1991). The full curve in Fig. 19 reflects the total absorption coefficient according to Eq. (44) using an electron concentration of $6 \times 10^{17}\,\mathrm{cm}^{-3}$ and a temperature of $T = 5\,\mathrm{K}$. (At this doping level the Fermi energy lies above the top of the first miniband, i.e., the first miniband is "full.") Now the asymmetry is further enhanced so that the low-frequency peak, resulting from transitions at the edge of the mini-Brillouin zone, becomes much stronger than the high-frequency peak (corresponding to transitions near $k_z = 0$), which is merely visible as a shoulder. (Note that naive use of the $e\mathbf{E}\cdot\mathbf{r}$ interaction leads just to a reversed asymmetry; Kim *et al.*, 1990). The reason for this is the variation of the oscillator strength, $f_{12}(k_z)$, across the Brillouin zone (Helm, 1995) illustrated in Fig. 20 for GaAs–$Al_{0.3}Ga_{0.7}As$ superlattices with 75-Å well width and barrier widths of $b = 15$, 25, and 40 Å, corresponding to miniband widths Δ_1 of 36, 18, and 7 meV, respectively. For comparison, the oscillator strength f_{12} of an infinite single QW is also shown. Evidently, for wider minibands, more and more oscillator strength is concentrated near the zone edge. In the opposite limit of very narrow minibands, the oscillator strength is independent of k_z and of the order unity. Note that the average of $f_{12}(k_z)$ across the minizone remains of the order unity even for wide bands. This can be understood with the help of the extension of the oscillator sum rule (Eq. (16)) for energy bands (and not only discrete levels),

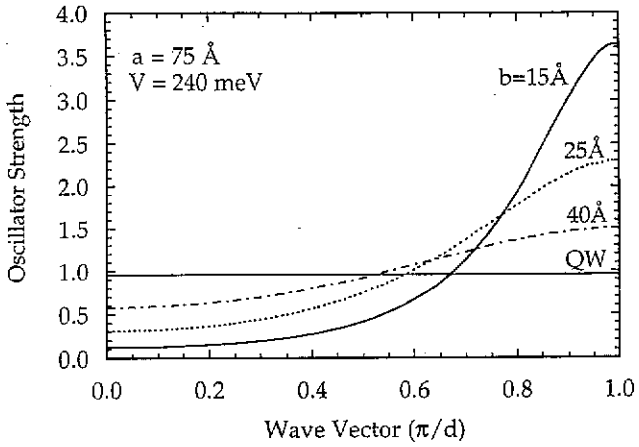

FIG. 20. Oscillator strength f_{12} as a function of k_z for superlattices with the same well width (75 Å), but different barrier widths b, as indicated. The horizontal line represents the case of an infinite QW (from Helm, 1995).

which reads

$$\sum_j f_{ij}(k_z) + \frac{m^*}{\hbar^2}\frac{\partial^2 E_i(k_z)}{\partial k_z^2} = 1 \qquad \text{or} \qquad \sum_j f_{ij}(k_z) = 1 - \frac{m^*}{m_{SL}^{(i)}} \tag{45}$$

Here $m_{SL}^{(i)}$ is the effective mass along the z direction, which is related to the curvature of the miniband at a certain point along k_z. In the preceding equation, the first term describes transitions between different minibands (interminiband transitions), whereas the second term corresponds to free-carrier type of transitions within one miniband (Helm, 1995). From Eq. (45) it is clear that a large curvature (or a small effective miniband mass along the z direction) will strongly influence the values of $f_{ij}(k_z)$. Since the miniband curvature is positive near $k_z = 0$, the oscillator strength must be reduced there, whereas it must be enhanced due to the negative curvature near $k_z = \pi/d$. Thus, near $k_z = 0$, the sum rule is completed through free-carrier absorption, whereas near $k_z = \pi/d$ it is accomplished through free-carrier emission processes (Helm, 1995).

Experiments on intersubband absorption in strongly coupled superlattices (or interminiband absorption) are rather scarce. After some initial reports in connection with infrared detectors (Byungsung *et al.*, 1990; Gunapala *et al.*, 1991), Helm *et al.* (1991, 1993) presented absorption spectra clearly

showing the predicted asymmetric line shape resulting from the singularities in the JDOS. As can be seen in Fig. 21, when compared to the calculated spectrum (Fig. 19) the interminiband absorption is well described by the above theory. In this superlattice ($n = 6 \times 10^{17}\,\mathrm{cm}^{-3}$) the Fermi energy at low temperatures lies above the top edge of the first miniband, and thus the spectra are basically temperature independent (apart from some additional line broadening at high temperature). The situation is different for a lower doping level ($n = 6 \times 10^{16}\,\mathrm{cm}^{-3}$), when the Fermi energy lies approximately in the middle of the first miniband (Fig. 22). In this case the top edge of the first miniband can be populated with electrons by increasing the temperature, and thus the absorption spectrum becomes strongly temperature dependent. The additional line appearing at low temperature at $\hbar\omega = 125$ meV is due to the $1s{-}2p_z$ donor transition, as discussed in more detail in Section XI, Subsection 3.

At the end of this section, we mention another experiment in which Streibl *et al.* (1996) observed the interminiband absorption in a finite superlattice, which was embedded in a modulation doped, wide parabolic quantum well (see Section XI, Subsection 2). In this way, the donor impurities are spatially separated from the entire superlattice (Jo *et al.*, 1990), leading to a higher electron mobility. The authors observed an indication of a line narrowing due to the collective effects (see Section VII), which was predicted by Zaluzny (1992b).

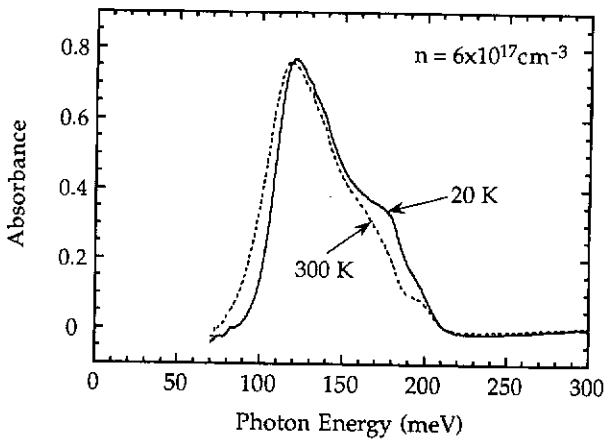

FIG. 21. Measured absorption spectrum for a GaAs–$Al_{0.3}Ga_{0.7}As$ superlattice ($a = 75$ Å, $b = 25$ Å) with $n = 6 \times 10^{17}\,\mathrm{cm}^{-3}$ at $T = 20$ and 300 K. This should be compared with the theoretical curve in Fig. 19 (from Helm, 1995).

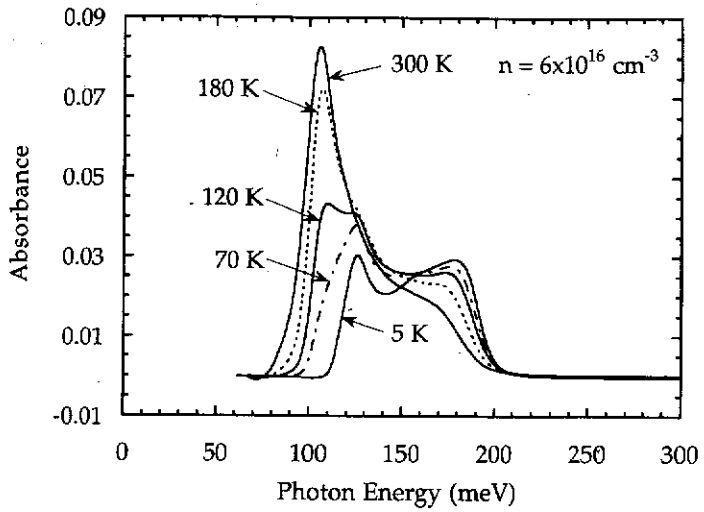

FIG. 22. Measured absorption spectrum for a GaAs–$Al_{0.3}Ga_{0.7}As$ superlattice (a = 75 Å, b = 25 Å) with $n = 6 \times 10^{16}$ cm^{-3} for different temperatures as indicated. For an explanation, see text (from Helm *et al.*, 1993).

VII. Nonparabolicity and Many-Body Effects

So far we have discussed the basic energy level structure of quantum wells and superlattices (SLs). In reality, however, it turns out that the exact energy levels and the measured absorption line positions can significantly differ from these simple predictions. There are a number of physical effects that can cause such energy shifts, all of which were studied in detail over the past decade. They can be divided into

1. Band structure effects: nonparabolicity in the z direction (Nelson *et al.* 1987; Yoo *et al.*, 1989), nonparabolicity in the QW plane (Ekenberg, 1987, 1989), and its effect on the intersubband absorption line shape (Newson and Kurobe, 1988; von Allmen *et al.*, 1988)
2. Effects of Coulomb interaction on the energy levels (Hartree self-consistent potential and exchange-correlation energy)
3. Effects of Coulomb interaction on absorption frequency (depolarization shift, exciton shift) (Ando *et al.*, 1982; Batke, 1991).

In the following, we briefly summarize all these effects, but we see that not all of them can simply be separated.

For many experimental situations (such as GaAs QWs with thicknesses between 50 and 100 Å and sheet electron density of 10^{11} to $10^{12}\,\mathrm{cm}^{-2}$), all of the preceding effects contribute not more than around 10% to the absorption peak position, so they often can be neglected as long as only a crude estimate is desired. A detailed understanding, however, requires inclusion of all of them, since they are of the same order of magnitude and partly compensate each other. For wide quantum wells, on the other hand, the Coulomb effects 2 and 3 become very important, since the Coulomb energy becomes of the same order of magnitude as the subband separation.

1. NONPARABOLICITY

The parabolic approximation for the band structure is valid only at low energies, close to the relevant conduction band minimum, which is the Γ point in most cases. At higher energy, coupling to different bands (the valence and higher conduction bands) plays a significant role, especially for narrow-gap materials, which makes the effective mass energy-dependent. The theoretical standard approach for, for example, the electrons in the conduction band of GaAs–AlGaAs quantum wells, is the evaluation of the full 8×8 or 14×14 $\mathbf{k}\cdot\mathbf{p}$ matrix Hamiltonian by applying Kane's theory to heterostructures (Bastard, 1981, 1982, 1988). Simpler $\mathbf{k}\cdot\mathbf{p}$ models (such as the Kane–Bastard two-band model), which are desired for less cumbersome calculations, put severe restrictions on the effective masses involved (e.g., masses of electrons and light holes are equal, as are the well and barrier masses at the same energy). Therefore some simple, more semiempirical methods have been proposed, which use a larger number of independent input parameters. Nelson *et al.* (1987) proposed an "empirical two-band model," which is based on Kane's two-band model, but three independent parameters are taken either from experiment or from a more accurate (14×14) $\mathbf{k}\cdot\mathbf{p}$ calculation for the bulk material. Within this model the energy dispersion can be written in the following form:

$$\frac{\hbar^2 k^2}{2m^*} = E(1 + E/E_g') \qquad \text{or} \qquad E = \frac{\hbar^2 k^2}{2m^*}(1 - \gamma k^2) \tag{46}$$

A relation of this type is valid for the well and barrier materials, leading to totally four parameters: the band-edge masses m^* in the well and the barrier, and the nonparabolicity parameter γ in both materials (or, equivalently, an "effective" energy gap E_g'). The band-edge masses in the well and barrier materials can be taken from experiment and are known with high

accuracy in most materials. The value of γ (or E_g') is chosen to achieve the best agreement with the experiments, or can be obtained from a more extensive $\mathbf{k}\cdot\mathbf{p}$ calculation with the results fitted by Eq. (46). Then for a given set (m_w^*, m_b^*, γ_w), γ_b is uniquely determined through the condition $\gamma_w/\gamma_b = (m_b^*/m_w^*)^2$ (or $m_w^*/m_b^* = E_w'/E_b'$), when the interband matrix elements are assumed to be the same in both materials. Thus, this scheme uses the simplest possible functional form to describe nonparabolicity and cures the remaining inaccuracy by determining the relevant adjustable parameters by some other means. Another way to put it is that the usual parameters in $\mathbf{k}\cdot\mathbf{p}$ theory, the (real) energy gap E_g and the Kane matrix element P are eliminated in favor of m^* and γ (Zaluzny, 1991). For example, the nonparabolicity parameter for GaAs is $\gamma = 4.9 \times 10^{-19}\,\mathrm{m}^2$ (Nelson *et al.*, 1987). A detailed description of this procedure can be found in Nelson *et al.* (1987) and Yoo *et al.* (1989). For further discussions, see Eppenga *et al.* (1987), Persson and Cohen (1988), Winkler and Rössler (1993), Burt (1992), and Meney *et al.* (1994). A simple approximate description was also presented by Altschul *et al.* (1992).

One interesting result of this model concerning subbands in QWs is that the position of the lowest subband is virtually uninfluenced by nonparabolicity, no matter how narrow the QW and how large the confinement energy. This is so because the strong nonparabolicity in the well material (increasing effective mass with energy) is compensated due to the strong wave function penetration into the barriers, where the nonparabolicity acts the opposite way (decreasing mass deeper in the barriers). The largest energy shifts (toward lower energy) are observed for subbands with high quantum numbers, since they are high in energy with respect to the QW band edge, but very close to the barrier band edge. This behavior obviously gives rise to a red shift of the intersubband absorption.

Nonparabolic effects, of course, not only shift the subband edges, but also increase the effective mass for electrons moving in the quantum well planes. Ekenberg (1987, 1989) presented a thorough discussion of the effect of nonparabolicity on the perpendicular mass, m_z^* (which influences the subband energies) and the in-plane mass, $m_\parallel^*$ (which influences the in-plane dispersion), starting from a fourth-order expansion of $E(\mathbf{k})$, which is based on the $14 \times 14\,\mathbf{k}\cdot\mathbf{p}$ model (Rössler, 1984; Braun and Rössler, 1985)

$$E(\mathbf{k}) = \alpha_0 k_z^4 + \left[\frac{\hbar^2}{2m_1} + (2\alpha_0 + \beta_0)(k_x^2 + k_y^2)\right] k_z^2 + \frac{\hbar^2}{2m_1}(k_x^2 + k_y^2) + (2\alpha_0 + \beta_0)k_x^2 k_y^2 + \alpha_0(k_x^4 + k_y^4) \qquad (47)$$

Here the spin splitting is neglected and the k_z terms are collected separately.

Note that α_0 and β_0 are negative. For heterostructures, k_z must be replaced by $-id/dz$ and the QW potential $V(z)$ must be added. He obtains approximate expressions for m_z^* and $m_\parallel^*$, which are

$$m_z^*(E) = m^*(1 + \alpha E) \tag{48}$$

and

$$m_\parallel^*(E) = m^*[1 + (2\alpha + \beta)E] \tag{49}$$

Here m^* is the band-edge effective mass, and α and β are related to the fourth-order coefficient of the $E(\mathbf{k})$ expansion ($\alpha = -(2m_1/\hbar^2)^2\alpha_0$, $\beta = -(2m_1/\hbar^2)^2\beta_0$, given by $\alpha = 0.64\,\mathrm{eV}^{-1}$ and $\beta = 0.70\,\mathrm{eV}^{-1}$, respectively, for GaAs. Therefore, the nonparabolicity enhancement in the QW planes is about three times larger than along the growth direction. Ekenberg's result also confirm the weak influence on the ground-state binding energy. He further discusses the effect of different boundary conditions for matching the wave functions at the interfaces (Ekenberg, 1989; Burt, 1992).

The influence of nonparabolicity on the intersubband absorption (Newson and Kurobe, 1988) is, from a theoretical point of view, a crucial one, since the integration over k_x and k_y cannot be performed analytically and the JDOS is no longer a δ function. Thus, the absorption coefficient must be calculated through a two (for QWs) or three (for SLs) dimensional integration over k-space using some form of energy dispersion $E(\mathbf{k}_\perp k_z)$, as in Eq. (18) of Section II. The intersubband absorption line shape then acquires some additional, asymmetric broadening on the low-frequency side, which should become relevant at high doping levels, when the Fermi energy is large. Recently it has been shown, however, that this broadening can be entirely compensated by many-body effects (see below in Subsection 4; also Zaluzny, 1991; von Allmen, 1992; Warburton *et al.*, 1996).

2. Self-Consistent Coulomb Potential

To provide the electrons or holes necessary to observe intersubband transitions, quantum wells have to be doped. Since the electron charge distribution, which is determined by the wave functions of all occupied subband levels, will never be identical to the spatial distribution of the donor host ions, the positive and negative contributions do not cancel and there will be a remaining electrostatic potential. Although this effect is relatively weak, when the doping is placed directly in the QWs, it becomes very large when the doping is placed into the barrier material. In this case, the

electrons are transferred to the well and are spatially separated from the dopants, leading to a strong modification of the potential. This is called modulation doping and is known to increase the electron mobility and decrease the intersubband absorption line broadening, since impurity scattering becomes suppressed due to the spatial separation of the electrons from the impurities.

This contribution to the potential energy is called Hartree potential V_H and can be calculated via Poisson's equation (with $V_H = -e\Phi$)

$$\frac{\partial^2 \Phi}{\partial z^2} = \frac{e}{\varepsilon \varepsilon_0} [n(z) - N_D(z)] \tag{50}$$

the solution to which is obtained by two integrations, but it can be brought into a form containing only one integration, which is more convenient for numerical evaluation

$$\Phi(z) = \frac{e}{\varepsilon \varepsilon_0} \int_{-\infty}^{z} (z - z')[n(z') - N_D(z')]\, dz' \tag{51}$$

In these equations, $N_D(z)$ is the donor doping profile (ionized donors only) and $n(z)$ is the three-dimensional electron density, given by

$$n(z) = \sum_i n_i |\varphi_i(z)|^2 = \frac{m^* kT}{\pi \hbar^2} \sum_i \ln \left[1 + \exp\left(\frac{E_F - E_i}{kT} \right) \right] \cdot |\varphi_i(z)|^2 \tag{52}$$

for finite temperatures and multiple subband occupancy. If different effective masses m_i^* are used for the different subbands, m_i^* must be taken under the sum. Here n_i is the areal electron concentration in the ith subband and $\varphi_i(z)$ is the respective wave function. The Fermi energy E_F must also be determined self-consistently so that $\int n(z) = \Sigma_i n_i = n_s$, where n_s is the total areal electron concentration. Equations (50) and (52) must be solved self-consistently together with Schrödinger's equation with V_H added to the Hamiltonian. Both are coupled via the appearance of the wave function in Poisson's equation.

In the usual picture, where electron energies are counted positive, negative charge gives rise to negative curvature of the potential profile, while positive charge results in positive curvature. As an example, let us consider an 80-Å-wide $GaAs-Al_{0.3}Ga_{0.7}As$ quantum well. Using the bare confining potential (barrier height 240 meV) leads to two bound states, $E_1 = 42.3$ meV and $E_2 = 153.5$ meV, corresponding to a subband separation of $E_{21} = 111.1$ meV.

Now the self-consistent Hartree potential is taken into account for two doping profiles. Figure 23a shows a modulation doped structure, where the barriers are doped with $N_D = 5 \times 10^{18}\,\mathrm{cm}^{-3}$ over 10 Å, 40 Å away from the quantum well. This yields an areal electron density of $n_s = 1 \times 10^{12}\,\mathrm{cm}^{-2}$ in the QW. The strong band bending reduces the subband separation to $E_{21} =$ 104.4 meV. The second structure (Fig. 23b) is doped over the center 50 Å of the well with $N_D = 2 \times 10^{18}\,\mathrm{cm}^{-3}$, resulting in the same areal electron concentration. The band bending is, however, much weaker, and the subband separation is slightly increased to 112.3 meV with respect to the bare potential.

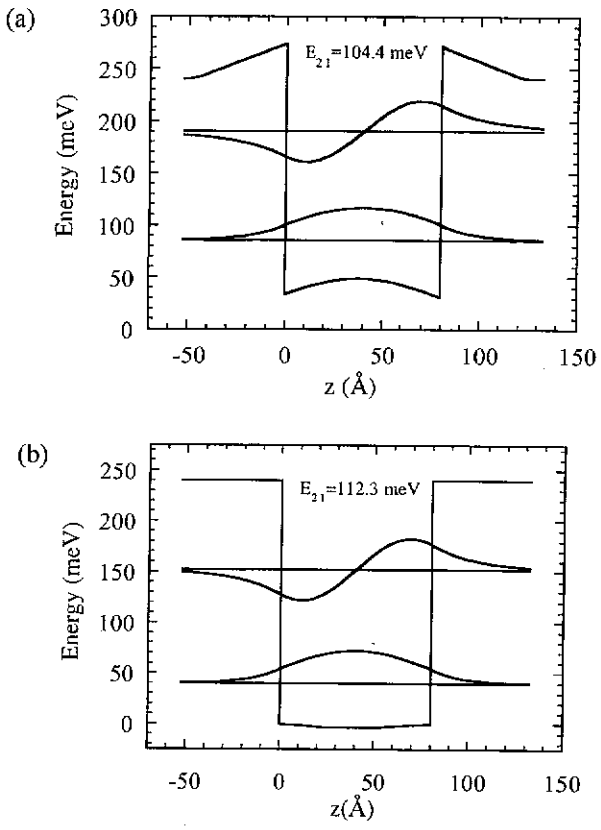

FIG. 23. Conduction-band profile, energy levels, and wave functions of an 80-Å-wide GaAs–$Al_{0.3}Ga_{0.7}As$ quantum well with an areal electron concentration of $n_s = 1 \times 10^{12}\,\mathrm{cm}^{-2}$: (a) doping in the barriers (modulation doping) and (b) doping in the well. The energy separation $E_2 - E_1$ is given in the figure.

Some complication arises, when a nonparabolic variation of the effective mass is taken into account, since due to the band bending m^* becomes z-dependent even within in the same material. In this case, a weighted spatial average of the effective mass can be used (Bastard, 1988), defined through

$$\frac{1}{m_i^*} = \int_{-\infty}^{\infty} \frac{|\varphi_i(z)|^2}{m_i^*(z)}\, dz \tag{53}$$

3. MANY-BODY EFFECTS ON THE ENERGY (EXCHANGE AND CORRELATION)

At the electron densities usually encountered in semiconductor QWs and heterostructures, many-body effects on the energy of the electron gas also play a nonnegligible role (i.e., the exchange and correlation energies). Two methods for their calculation have been frequently used for the quasi-two-dimensional electron gas in a quantum well: The Hartree–Fock method, which yields an explicit expression for the exchange energy but neglects correlations, and the local-density approximation (LDA) within the Kohn–Sham density functional theory (Kohn and Sham, 1965).

The exchange integral in the Hartree–Fock equation, which represents a nonlocal potential, has been evaluated in an approximate way by Bandara *et al.* (1988, 1989) for electrons in the ground subband using infinite QW wave functions. This leads to

$$E_{\text{exch}}(k) \cong \frac{-e^2}{4\pi\varepsilon\varepsilon_0} k_F \left[\frac{2}{\pi} E(k/k_F) - 0.32(k_F/k_L)\right] \tag{54}$$

for $k < k_F$. Here k_L is an inverse length characteristic of the QW (e.g., $k_L = \pi/L$ for an infinite QW), and $\mathbf{E}(k/k_F)$ is a complete elliptical integral of the second kind. For $k > k_F$, a similar expression results (Bandara *et al.*, 1988, 1989; Manasreh *et al.*, 1991; Szmulowicz *et al.*, 1994); also Zaluzny (1992a) provided a simple expression.

Within the Kohn–Sham density functional theory using the LDA, the combined exchange-correlation potential can be written as a functional of the electron density $V_{xc}(n(z))$ and added as a (now local) potential in the single-particle Schrödinger equation, in a way similar to the Hartree potential $V_H(n(z))$. (Note that for the LDA to hold strictly, the electron density is required to exhibit only slow spatial variations, which is, in fact, not well fulfilled in QWs.) Various forms for $V_{xc}(n(z))$ have been suggested

in the literature. The following expression given by Hedin and Lundqvist (1971) has also been used frequently for electrons in quantum wells (Bloss, 1989):

$$V_{xc} = -\left(\frac{9\pi}{4}\right)^{1/3} \frac{2}{\pi r_s}\left[1 + \frac{B}{A} r_s \ln\left(1 + \frac{A}{r_s}\right)\right] \cdot \frac{e^2}{8\pi\varepsilon\varepsilon_0 a^*} \tag{55}$$

Here r_s is the dimensionless parameter characterizing the electron gas, given by $r_s = [(4\pi/3)a^{*3}n(z)]^{-1/3}$ and corresponding to the mean electron distance normalized to the effective Bohr radius $a^* = (\varepsilon/m^*)a_B$. The constants A and B were quoted as $A = 21$ and $B = 0.7734$ (in a later paper, Gunnarsson and Lundqvist, 1976, give values of $A = 11.4$ and $B = 0.6213$, see also Chuang *et al.*, 1992; Luo *et al.*, 1993); both values probably lie within the uncertainty of the theory with the approximations made). This expression is claimed by its originators to be valid in a rather wide range of r_s.

In contrast to Eq. (54), Eq. (55) does not exhibit any k-dependence and leads to a correction that is two to three times smaller than in the Hartree–Fock approximation (Zaluzny, 1992a), which tends to overestimate the energy correction. For a discussion of the use of the Hartree–Fock equation vs density-functional theory, compare Jogai (1991) and the comment by Szmulowicz and Manasreh (1992).

The main effect of including the exchange (and correlation) energies is a lowering of the total electron energy (or the effective potential) in regions of high electron density. This results in a lowering of the subband levels. Since the ground subband is mostly influenced, this leads to a blue shift of the intersubband absorption. Note that in cases where the doping is placed into the QW (no charge separation), the exchange effect can be larger than the effect of the direct Coulomb term (Hartree potential). Especially in systems with a large effective mass, the exchange energy becomes appreciable when compared to the confinement energy.

Thus finally, using the preceding parameterization of the exchange-correlation energy, the following Schrödinger equation must be solved together with Eqs. (50) and (52):

$$\left[\frac{-\hbar^2}{2m^*}\frac{d^2}{dz^2} + V(z) + V_H(n(z)) + V_{xc}(n(z))\right]\varphi_n(z) = E_n\varphi_n(z) \tag{56}$$

neglecting all complications that arise from a nonconstant effective mass for simplicity.

As an illustration, the preceding GaAs–$Al_{0.3}Ga_{0.7}As$ QW (with doping in the well) is shown again in Fig. 24, now including the exchange-

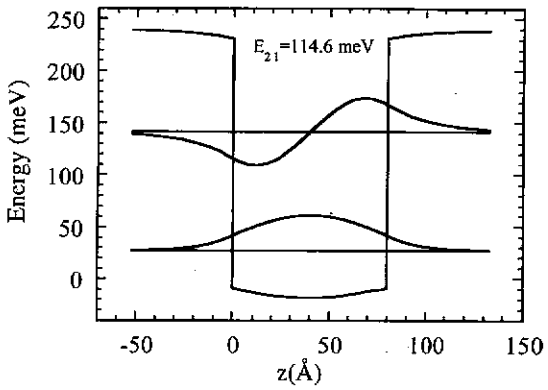

FIG. 24. The GaAs–$Al_{0.3}Ga_{0.7}As$ quantum well of Fig. 23 doped in the well, but with the exchange-correlation energy added to the potential.

correlation potential according to Eq. (55). The potential lowering in the regions of high electron density is clearly observed, and the subband separation is slightly increased to $E_{21} = 114.6\,\text{meV}$.

4. COLLECTIVE EFFECTS ON THE ABSORPTION (DEPOLARIZATION AND EXCITON SHIFT)

Many-body effects are relevant not only for the energy of the electron gas but also for its electric conductivity (or polarizability), which must be calculated to obtain the absorption spectrum in a many-body theory. The single-particle approach presented in Section II is not sufficient in this case. It has been shown that there are two main terms that cause a shift of the absorption maximum with respect to the bare energy levels; that is, the absorption does not occur at the energy difference $E_{21} = E_2 - E_1$, but rather at an energy given by

$$\tilde{E}_{21}^2 = E_{21}^2(1 + \alpha - \beta) \tag{57}$$

The frequency shifts represented by α and β (both >0) are known as the depolarization shift and the exciton or final-state interaction, respectively, in the many-body calculation of the conductivity or polarizability (Vinter, 1976, 1977; Ando *et al.*, 1982; Batke, 1991, and references therein). Here α and β should not be confused with the nonparabolicity parameters in the preceding section.

The depolarization shift essentially comes from a (time-dependent) Hartree term related to the high-frequency field inducing the absorption. Each electron feels an effective field that is different from the external field by the mean Hartree field of the other electrons polarized by the external field. Thus, the external field is screened by the quasi-two-dimensional electron gas (corresponding to the random phase approximation for the dynamic conductivity). In this spirit, Allen *et al.* (1976) calculated the depolarization shift using time-dependent perturbation theory by introducing a self-consistent AC potential in Schrödinger's equation and evaluating the induced oscillating charge density and AC current self-consistently from Poisson's equation. In this treatment, we restrict ourselves to a two-level system, which requires that there is significant oscillator strength for transitions to only one excited state. A generalization for several levels was performed by Allen *et al.* (1976) and Chun *et al.* (1993).

The frequency shift α (depolarization shift) is given by

$$\alpha = \frac{2e^2 n_s}{\varepsilon\varepsilon_0 E_{21}} S \qquad \text{with} \qquad S = \int_{-\infty}^{\infty} dz \left[\int_{-\infty}^{z} dz' \varphi_2(z') \varphi_1(z') \right]^2 \tag{58}$$

where S (in the literature often called S_{11}) has the units of length, and α is proportional to the electron density, in fact, the squared frequency shift is of the order of the three-dimensional plasma frequency and the absorption frequency can be written in the form $\tilde{\omega}_{21}^2 = \omega_{21}^2 + f_{12}\omega_p^2$, as was recognized by Chen *et al.* (1976). Here ω_p is a 3D plasma frequency defined by $\omega_p^2 = (n_s e^2/\varepsilon\varepsilon_0 m^* L_{\text{eff}})$, with $L_{\text{eff}} = (\hbar^2 f_{12}/2m^* S E_{21})$. This is the L_{eff} that must be used in Eq. (40) for consistency. Note that the oscillator strength f_{12} cancels in the final shift. For an infinite QW of thickness L, the preceding can be calculated analytically to give the values $S = (5/9\pi^2) \cdot L = 0.056 \cdot L$ and $L_{\text{eff}} = f_{12} \cdot (3/5) \cdot L$.

The physical content of the depolarization shift can be understood through the collective nature of the intersubband absorption. Exposing the system to external radiation not only excites electrons into the higher subband but also modulates their charge density. The restoring Coulomb force gives rise to a kind of plasma oscillation. The combined intersubband–Coulomb problem can thus be regarded as two coupled oscillators with frequencies ω_{21} and ω_p (Sherwin *et al.*, 1995).

As evident from the preceding formulas, the depolarization shift is important only at high electron densities and/or small energy separations. For quantum wells with E_{21} around 100 meV and $n_s < 10^{12}\,\text{cm}^{-2}$ it is a minor correction (see example following).

The same is true for the second term, β, which acts to reduce the absorption frequency, and is due to the Coulomb interaction between the excited electron and the quasi-hole left behind in the ground subband. Since this is similar to an excitonic electron–hole pair, the effect is called the exciton correction, or the final-state interaction. It corresponds to a reduction of the mean Hartree field around each electron due to exchange-correlation effects. In a systematic many-body theory, it can be shown that β represents a local field or vertex correction to the depolarization shift (Ando *et al.*, 1982; Bloss, 1989). Ando (1977a, 1977b) calculated both terms, α and β, using the density functional theory in the local density approximation and obtained

$$\beta = -\frac{2n_s}{E_{21}} \int_{-\infty}^{\infty} dz \varphi_2(z)^2 \varphi_1(z)^2 \frac{\partial V_{xc}[n(z)]}{\partial n(z)} \tag{59}$$

where V_{xc} is the exchange-correlation energy of Eq. (55). Since dV_{xc}/dn is negative (V_{xc} becomes more negative, when n is increased), β is a positive number. For GaAs QWs, β is usually much smaller than α. However, in the two-dimensional electron gas in Si accumulation or inversion layers, they can be of the same order of magnitude (resulting mostly from the higher effective mass), so that both effects nearly compensate each other.

Ando (1977a, 1977b, 1978) presented a treatment using the two-dimensional conductivity σ_{zz} and modified (observable) conductivity $\tilde{\sigma}_{zz}$ that reflect the response to the total electric field and external electric field, respectively. The induced current can be written as

$$j_z = \sigma_{zz} E \tag{60}$$

The external field E_{ext} is related to the total field through

$$E_{\text{ext}} = \varepsilon_{zz} E \tag{61}$$

where ε_{zz} is the dielectric function,

$$\varepsilon_{zz} = 1 + i \frac{\sigma_{zz}}{\varepsilon_0 \varepsilon_{\text{st}} \omega L_{\text{eff}}} \tag{62}$$

and ε_{st} the static background dielectric constant. The current can be expressed as

$$j_z = \tilde{\sigma}_{zz} E_{\text{ext}} \tag{63}$$

with

$$\tilde{\sigma}_{zz} = \frac{\sigma_{zz}}{\varepsilon_{zz}} = \frac{\sigma_{zz}}{1 + i(\sigma_{zz}/\varepsilon_0 \varepsilon_{st} \omega L_{eff})} \tag{64}$$

As a consequence, the absorption of the 2D layer occurs not at the poles, but at the zeroes of the dielectric function. If σ_{zz} is the conductivity of a two-dimensional electron gas with parabolic energy dispersion (i.e., E_{21} is independent of $\mathbf{k}_\perp$), the resulting $\tilde{\sigma}_{zz}$ has the same Drude-form as σ_{zz} (see Eq. (27)), however, with a renormalized resonance frequency $\tilde{\omega}_{21}$:

$$\tilde{\sigma}_{zz} = \frac{n_s e^2 f_{12}}{m^*} \frac{-i\omega}{\tilde{\omega}_{21}^2 - \omega^2 - 2i\gamma\omega} \tag{65}$$

The absorption A (if $A \ll 1$) is then again given by $A = (\mathrm{Re}\tilde{\sigma}_{zz}/\varepsilon_0 c\eta)$ (compare Eq. (26)).

To determine some numerical values let us go back to the earlier well-doped, 80-Å-wide GaAs–$Al_{0.3}Ga_{0.7}As$ QW. For this structure, we obtain $\alpha = 0.16$ and $\beta = 0.058$, which corresponds to a depolarization shift of 8.8 meV and exciton correction of -3.4 meV, if each is considered alone, and in a combined shift (according to Eq. (57)) of 5.7 meV. We can calculate now the position of the resonance absorption $\tilde{E}_{21}$ when the various correction terms are added successively:

	Resonance position
bare potential	111.2 meV
+ Hartree	112.3 meV
+ exchange correlation	114.6 meV
+ depolarization	123.4 meV
+ exciton	120.3 meV

The total shift is less than 10% and is dominated by the depolarization effect. It is clear, however, that for wide QWs with a bare subband separation of less than 20 meV the collective energies can become as large as E_{21}, and an intersubband transition cannot be described in a single-particle picture anymore.

For systems with nonparabolic energy dispersions (which require integration over k_x and k_y) the conductivity takes the more general form (Ando,

1978; Zaluzny, 1991, 1992a; Warburton *et al.*, 1996)

$$\tilde{\sigma}_{zz}(\omega) = \frac{n_s e^2 f_{12}}{m^*} \frac{-i\omega}{\omega_{21}^2(0)} \frac{G(\omega)}{1 + (\alpha - \beta)G(\omega)} \tag{66}$$

with

$$G(\omega) = \frac{1}{n_s} \frac{2}{(2\pi)^2} \int d^2k_\perp \frac{\omega_{21}^2(0)}{\omega_{21}^2(\mathbf{k}_\perp) - \omega^2 - 2i\omega\gamma} \tag{67}$$

The integration goes over all occupied states up to the Fermi wavevector. The change of the oscillator strength with $\mathbf{k}_\perp$ has been neglected. For superlattices, one proceeds similarly (Zaluzny, 1992b), except that the integration is over k_z. At finite temperature, $G(\omega)$ would contain the difference between the initial and final state distribution functions in addition.

Zaluzny (1991, 1992a, b) noted that under such conditions, the depolarization effect not only shifts the absorption resonance but can also induce a significant modification of the line shape. For a highly doped QW with large nonparabolicity, one expects a broad absorption line due to the $\mathbf{k}_\perp$ dependence of the transition energy $E_{21}(\mathbf{k}_\perp)$. When the depolarization effect is included, however, it turns out that the absorption spectrum consists of a narrow line near the high-energy side of $E_{21}(\mathbf{k}_\perp)$; thus nonparabolicity is compensated by the depolarization field (Zaluzny, 1991). This effect was also confirmed through experiments on InAs–AlSb QWs (Warburton *et al.*, 1996). Figure 25 shows the calculated absorption for a 150-Å-wide InAs–AlSb quantum well with an electron concentration of $n_s = 1 \times 10^{12}\,\mathrm{cm}^{-2}$. The small effective mass of InAs results in a large Fermi energy (over 50 meV) and a high nonparabolicity. Note that E_{21} varies by nearly 20 meV between $k_\perp = 0$ and $k_\perp = k_F$, as can be seen from the dotted curves, where the depolarization effect is neglected. When it is included (full curves), the absorption is shifted above the single-particle excitations (which are still visible as a low-energy shoulder) and its width is determined by the Lorentzian broadening parameter γ (in Fig. 26, the HWHMs are $\hbar\gamma = 0.5$ and 2.5 meV, respectively) and not by the variation of $E_{21}(\mathbf{k}_\perp)$. The corresponding experiment (Fig. 26) clearly confirms the validity of the collective-excitation picture: the absorption consists of one narrow, nearly Lorentzian peak with no obvious sign of nonparabolicity broadening.

According to Zaluzny (1992a), the nonparabolicity due to the k-dependence of the exchange energy (Eq. (54)) is also eliminated in the same way. A similar mechanism is predicted to narrow interminiband absorption in

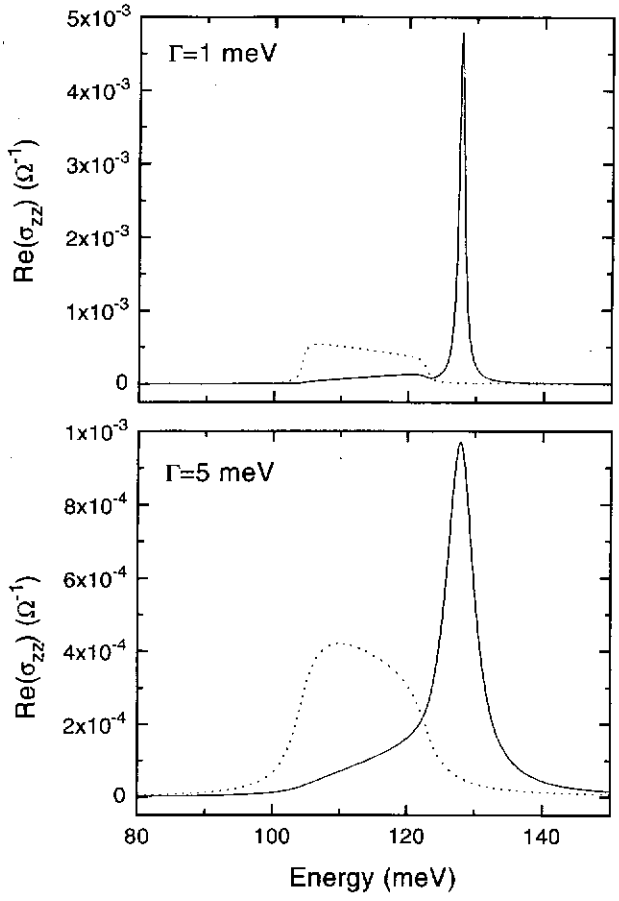

FIG. 25. Calculated real part of the conductivity (proportional to the absorption) of a 150-Å-wide InAs–AlSb quantum well. For the dotted curves, the depolarization effect was neglected; in the solid curves it is included. Spectra for two values of the broadening parameter Γ are shown. Note that here Γ is the FWHM, whereas in the main text we have used Γ (or γ) for the HWHM (from Warburton *et al.*, 1996).

strongly coupled superlattices (Zaluzny, 1992b). Nikonov *et al.* (1997) calculated the intersubband absorption in the framework of the semiconductor Bloch equations (Haug and Koch, 1993) in the Hartree–Fock approximation. In particular, they study the situation of two different effective masses in the first and second subbands, and find a similar line narrowing induced by the Coulomb and exchange interactions.

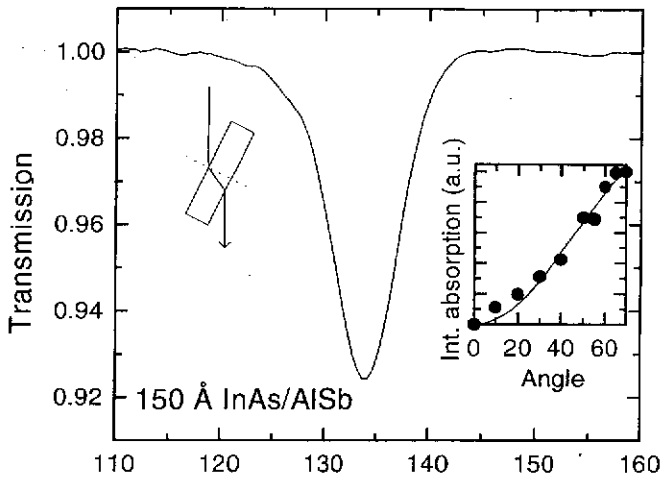

FIG. 26. Measured transmission spectrum of a 150-Å-wide InAs–AlSb quantum well. The experimental geometry is schematically shown as well as the angle (θ) dependence of the integrated absorption (from Warburton *et al.*, 1996).

A systematic treatment of many-body effects in intersubband transitions was presented by Chuang *et al.* (1992) and Luo *et al.* (1993) on the basis of the Bethe–Salpeter equation, and also by Huang *et al.* (1995). Other related approaches are due to Jiang (1992) and Boykin and Chui (1997).

It is interesting to note that in Raman scattering experiments (for a review see Pinczuk and Abstreiter, 1989), both the bare and dressed intersubband resonance can be measured (Pinczuk and Worlock, 1982; Pinczuk *et al.*, 1989; Ramsteiner *et al.*, 1990; Chuang *et al.*, 1992; Luo *et al.*, 1993). When the pump and scattered light have crossed polarizations, one measures the spin-density excitation (SDE), which is (nearly) coincident with the single-particle subband separation, whereas in crossed polarizations the charge-density excitation (CDE) is measured, which is identical to the depolarization shifted intersubband resonance. Intersubband excitations with a finite wavevector q have also been discussed (Heitmann *et al.*, 1982; Heitmann and Mackens, 1986; Yi and Quinn, 1983; Batke *et al.*, 1991).

The conclusion of this section is that a proper description of intersubband absorption has to proceed via a full quantum mechanical calculation of the conductivity or polarizability including band-structure and many-body effects on the same footing, and even treat the electromagnetics dictated by the sample geometry as outlined in Section IV. In other words, strictly the collective modes of the interacting system in response to the total (not

external) field have to be evaluated, taking into the correct boundary conditions and mode propagation. Still, in many realistic cases, the approach of Section II, which is based on the single-particle calculation of the absorption coefficient, can lead to satisfactory results within 10% accuracy.

VIII. Mechanisms for In-Plane Absorption

We have seen in Section II that the main intersubband absorption occurs for an electromagnetic wave polarized along the growth direction (i.e., perpendicular to the layer planes). This selection rule holds very well for many cases (such as, e.g., a typical *n*-type GaAs QW), but there are several mechanisms that can lead to relaxing this rule. In fact, theorists have actually searched for such mechanisms, since it would be useful for applications in infrared detectors (see Chapters 3 and 4 of this volume) to obtain absorption of in-plane polarized light, which can then be utilized in a normal-incidence geometry.

Strong normal-incidence intersubband absorption has been predicted and observed for holes in valence-band quantum wells, which is due to the mixing of the various hole bands. This is discussed in detail in the next section. In this section, we focus on mechanisms that enable in-plane polarized absorption in the simpler band structure of the conduction band.

1. INDIRECT-GAP SEMICONDUCTORS

In semiconductors with an indirect bandgap, the conduction-band minimum is located away from the Brillouin-zone center either near the X point (in the (001) direction) or near the L point (in the (111) direction). The constant-energy surfaces are then ellipsoids characterized by a longitudinal and a transverse effective mass. If the principal axis of such an ellipsoid is tilted with respect to the QW growth and confinement direction, the effective-mass tensor provides coupling between the parallel and perpendicular motion of the electrons. As a consequence, normally incident light (polarized in the plane of the layers) light leads to an electronic polarization component perpendicular to the layers and thus to intersubband transitions (Yang *et al.*, 1989; Brown and Eglash, 1990; Xu *et al.*, 1993, 1994). This concept was recognized many years ago in connection with Si-MOSFETs on (110) and (111) Si substrates (Yi and Quinn, 1983; Cole and McCombe, 1984). Interest has revived in this subject due to the prospect of realizing normal-incidence infrared detectors based on QWs.

The main candidates for this effect are of course Si and Ge, the former with the conduction-band minimum along the (001) direction (Δ) near the X point, the latter in the (111) direction at the L point. In addition, some III–V semiconductors are indirect as well: For an Al content $x > 0.45$ $Al_xGa_{1-x}As$ becomes indirect with the minimum at the X point, and $Al_xGa_{1-x}Sb$ is indirect for $0.25 > x > 0.55$ with the minimum at the L point (Xie *et al.*, 1991a), among others.

For electrons in an elliptical valley of a semiconductor heterostructure the Hamiltonian in the effective-mass approximation has the form

$$H = \tfrac{1}{2}\mathbf{p}\cdot\bar{\bar{\mathbf{w}}}\cdot\mathbf{p} + V(z) \tag{68}$$

where $\bar{\bar{\mathbf{w}}}$ is the 3×3 inverse effective mass tensor (Stern and Howard, 1967). The perturbation Hamiltonian for the electron–photon coupling is given by

$$H' = -\frac{e}{2}(\mathbf{A}\cdot\bar{\bar{\mathbf{w}}}\cdot\mathbf{p} + \mathbf{p}\cdot\bar{\bar{\mathbf{w}}}\cdot\mathbf{A}) \tag{69}$$

The absorption coefficient is now calculated in the same way as in Section II, by using the transition matrix elements $H'_{ij} = \langle\psi_i|H'|\psi_j\rangle$ and the dipole approximation. Since intersubband absorption is induced by the z component of the electronic polarization, only terms that contain a p_z component give a finite contributions. (Mathematically, the operators p_x and p_y have no net effect on the wave function and the matrix elements vanish due to the orthogonality of the wave functions.) Making also use of the symmetry of the inverse effective mass tensor, $w_{mn} = w_{nm}$, we obtain the transition rate

$$W_{if} = \frac{2\pi}{\hbar}e^2(A_x w_{xz} + A_y w_{yz} + A_z w_{zz})^2|\langle i|p_z|f\rangle|^2\delta(E_f - E_i - \hbar\omega) \tag{70}$$

where A_n are the Cartesian components of the amplitude of the vector potential. The absorption coefficient follows analogous to that in Section II. Xu *et al.* (1993, 1994) showed that with a proper coordinate transformation very general expressions for different material systems, substrate orientations, and polarizations can be obtained.

In the late 1970s it was predicted that the two-dimensional electron gas (2DEG) in Si-MOSFETs on (110) and (111) Si substrates should exhibit intersubband absorption for in-plane polarized radiation. Both theoretical (Ando *et al.*, 1977; Yi and Quinn, 1983) and extensive experimental (Cole and McCombe, 1984; Nee *et al.*, 1984; Wieck *et al.*, 1984) investigations have been carried out. One important result was the absence of the depolarization

shift for parallel excitation (Nee *et al.*, 1984). Chun and Wang (1992) (also Wang and Karunasiri, 1993; Wang *et al.*, 1994a) extensively discussed the intersubband absorption in *n*-type strained Si/SiGe quantum wells for various growth directions. Here, conduction-band QWs occur in the Si layers, when grown on a relaxed SiGe buffer. Experimental work include a study of *n*-type δ-doped Si/SiGe QWs on Si (110) (Lee and Wang, 1992) and Ge/SiGe QWs on Si (001) (Lee and Wang, 1994).

AlAs–$Al_xGa_{1-x}As$ *X*-valley QWs were investigated theoretically by Xie *et al.* (1992a, 1992b) and experimentally by Katz *et al.* (1992) for several substrate orientations other than (001). Here, an AlAs QW is embedded between AlGaAs barriers with $x \cong 0.4$. Wang *et al.* (1993) and Zhang *et al.* (1994) have fabricated a normal-incidence infrared detector using this scheme, the latter, however, grown on a Si substrate.

L-valley QWs and SLs based on the $Al_xGa_{1-x}Sb$–AlSb system were discussed by Xie *et al.* (1991a) and by Shaw and Jaros (1994). The latter work includes a microscopic calculation of the band structure and the linear and nonlinear susceptibilities. The normal-incidence absorption of an $Al_{0.09}Ga_{0.91}Sb$ QWs was experimentally demonstrated by Brown *et al.* (1992). Abramovich *et al.* (1994) studied the photoinduced intersubband absorption in GaSb–AlSb superlattices. Zhang *et al.* (1993) reported normal-incidence absorption and photoresponse in GaSb QWs, where the ground state is an *L*-type subband due to the confinement and the larger effective mass at the *L* point as compared to the Γ point. Normal-incidence electrooptic modulators were also proposed on this basis (Xie *et al.*, 1993, 1994).

Finally, another approach worth mentioning are QWs oriented vertically with respect to the wafer plane. Berger *et al.* (1995) fabricated such vertically oriented AlGaAs QWs (with low Al content) through growth on a patterned substrate and reported normal-incidence intersubband absorption of Γ point electrons. This is just the usual intersubband absorption, which is made possible here through the vertical orientation of the wells.

2. Spatial Variation of the Effective Mass

Yang (1995a, 1995b) has proposed a mechanism for in-plane polarized intersubband absorption, which applies even at the Γ point in a spherical conduction band, and relies on the spatial variation of the effective mass (i.e., m^* takes a different value in each of the material layers). When the variation of the effective mass along the z direction is taken into account, the proper form of the electron-photon Hamiltonian is

$$H' = \frac{e\mathbf{A}}{2} \cdot \left(\frac{1}{m^*(z)} \mathbf{p} + \mathbf{p} \frac{1}{m^*(z)} \right) \tag{71}$$

When the polarization of the perturbing electromagnetic field is taken in the QW plane, for instance, in the x direction, the induced transition rate according to Fermi's golden rule is then given by

$$W_{if} = \frac{2\pi}{\hbar} e^2 A_0^2 \hbar^2 k_x^2 \left| \left\langle i \left| \frac{1}{m^*(z)} \right| f \right\rangle \right|^2 \delta(E_f - E_i - \hbar\omega) \tag{72}$$

If the effective mass were constant throughout the quantum well system, it is clear that this rate would identically vanish due to the orthogonality of the wave functions. A z-dependent effective mass, however, leads to a finite value of the matrix elements and thus, of the absorption. For a symmetric quantum well, the matrix element is finite only when initial and final state have the same parity, which implies the selection rule $\Delta n = n' - n = 2, 4, \ldots$, in contrast to usual intersubband transitions. Candidates for observation of this effect are, for instance, step quantum wells, but so far no clear observation has been reported. Note also that in a multiband model, this effect actually tends to come out weaker, since the effective masses are energy dependent and become more alike in different materials at the same energy.

3. COUPLING TO THE VALENCE BAND

There is another mechanism that can give rise to in-plane polarized intersubband absorption of electrons at the Γ point. If one goes beyond the effective mass approximation (i.e., taking into account nonparabolicity), then not only the energy dispersions but also the electronic wave functions are modified. That is, they are not simple products of the conduction-band Bloch functions and an envelope function, but due to the band mixing in $\mathbf{k} \cdot \mathbf{p}$ theory, they acquire a contribution from the valence band. The wave functions are then linear combinations of electron as well as light, heavy, and split-off hole Bloch functions. The complete optical matrix elements within the 8×8 $\mathbf{k} \cdot \mathbf{p}$ model can thus be written (Yang *et al.*, 1994) (cf. Eq. (11))

$$\langle \psi_n | \mathbf{e} \cdot \mathbf{p} | \psi_{n'} \rangle = \sum_{j,j'=1}^{8} [\langle e^{i\mathbf{k}_\perp \cdot \mathbf{r}} \varphi_{nj} | \mathbf{e} \cdot \mathbf{p} | e^{i\mathbf{k}_\perp \cdot \mathbf{r}} \varphi_{n'j'} \rangle \langle u_j | u_{j'} \rangle + \langle \varphi_{nj} |_{n'j'} \rangle \langle u_j | \mathbf{e} \cdot \mathbf{p} | u_{j'} \rangle] \tag{73}$$

where φ_{nj} is the z-dependent part of the envelope function (n is the subband index) and u_j is the rapidly varying, periodic Bloch function of the jth band (with $\langle u_j | u_{j'} \rangle = \delta_{jj'}$). The first term is the envelope-function matrix element, which is responsible for the "usual," z-polarized intersubband absorption. The second term, which reflects the admixture from the other bands, can give rise to transitions for both orthogonal polarizations, and also transitions with and without a change of parity become allowed in principle. This issue was discussed in detail by Yang *et al.* (1994), Lew Yan Voon *et al.* (1995), Warburton *et al.* (1996), and Flatté *et al.* (1996). In most common quantum wells, the by far strongest transition is still the one with z polarization and parity change (Δn odd; e.g., the 1–2 transition). The matrix element for xy polarization with odd Δn reaches at maximum a few percent of this value, the ratio between the two can be approximated as (Yang *et al.*, 1994)

$$R_{xy/z} \approx \frac{1}{3} \frac{(E_{n'} - E_n)\Delta}{(E_n + E_g + \Delta)(E_{n'} + E_g)} \tag{74}$$

where E_n and $E_{n'}$ are the subband energies, E_g is the band gap, and Δ is the spin–orbit splitting of the valence band. Evidently the spin–orbit interaction is crucial here. The transitions with even Δn are still weaker (Warburton *et al.*, 1996) for both polarizations (of course not for asymmetric structures; there z-polarized transitions with Δn even can be very strong, cf. Section V). These effects should be (relatively) strongest in narrow-gap semiconductors such as InAs (small E_g, large Δ), where the band mixing is largest and also large k values are usually involved due to the small effective mass (Warburton *et al.*, 1996), but most likely still too small to be observed. Note that in the late 1970s and early 1980s in-plane polarized absorption was observed in surface layers of the narrow-gap semiconductors InSb (Beinvogl and Koch, 1977; Wiesinger *et al.*, 1982) and InAs (Reisinger and Koch, 1981), and corresponding calculations were performed by Zawadzki (1983), however on the basis of a 4×4 $\mathbf{k} \cdot \mathbf{p}$ model completely neglecting spin. In view of today's knowledge (Yang *et al.*, 1994; Warburton *et al.*, 1996), these calculations as well as that of Shik (1988, 1992) appear to overestimate the strength of the normal-incidence absorption. To date, only a few reports exist on the observation of in-plane polarized intersubband absorption in quantum wells ascribed to this mechanism. Peng *et al.* (1992, 1993), Peng and Fonstad (1993), Hirayama *et al.* (1993), and Smet *et al.* (1994) published a series of papers reporting both TM- and TE-polarized intersubband absorption of similar strength in InGaAs–InAlAs and InGaAs–AlAs structures prepared in slab waveguide

structures down to 40 μm thin and also in direct normal-incidence geometry. The peaks of the TM and TE mode were reported to be shifted from each other (polarization splitting) by a magnitude proportional to the strain in the structure. The authors have claimed to substantiate their experiments with a 14×14 $\mathbf{k}\cdot\mathbf{p}$ calculation (Peng and Fonstad, 1995), but this in turn was questioned by Lew Yan Voon *et al.* (1996). To our knowledge, the controversy on this topic has not yet been completely settled. In case the theoretical analysis by Yang *et al.* (1994), Warburton *et al.* (1994), and Lew Yan Voon *et al.* (1996) is correct, the origin of the observations of Peng *et al.* (1993) would still not be clear. The same is true for another work by Li *et al.* (1993) and Karunasiri *et al.* (1995), who have reported similar experimental results. Liu *et al.* (1998) conducted a systematic study of TE vs TM absorption and found the ratio to be less than 0.2% for a GaAs QW and still less than 3% for an InGaAs QW.

Finally, note that the band mixing just described as a mechanism for in-plane intersubband absorption is much more important in the valence band, where, in fact, it leads to strong, observable, normal-incidence intersubband absorption. The valence band is the topic of the next section.

IX. Intersubband Absorption in the Valence Band

So far we have considered only intersubband transitions of electrons in the conduction band of quantum wells. In a similar way, of course, valence-band intersubband transitions can be observed in quantum wells that are *p*-type doped. The main difference arises from the complexity of the valence band, which makes reasonably accurate calculations significantly more difficult, but also gives rise to some new phenomena, especially related to normal-incidence absorption. This is the reason why *p*-doped quantum wells are mainly being studied for applications in infrared detectors.

The valence-band maximum of most common semiconductors is located at the Γ point of the Brillouin zone, where it is fourfold degenerate (heavy holes (HHs) and light holes (LHs), each being doubly spin-degenerate). The degeneracy between heavy and light holes is lifted for nonzero values of the wavevector $\mathbf{k}$. In addition, a doubly degenerate band is split off by an amount Δ through the spin-orbit interaction (spin-orbit split-off band, SO). At $\mathbf{k} = 0$ all bands are decoupled, whereas for $\mathbf{k} \neq 0$ all bands are coupled (except in the (001) direction, where there is only a LH–SO coupling). In the case of a large spin-orbit splitting Δ, the interaction of the HH and LH bands with the SO band can be neglected. In Fig. 27 the valence-band structure is depicted schematically as it occurs in GaAs, Si, Ge, and other

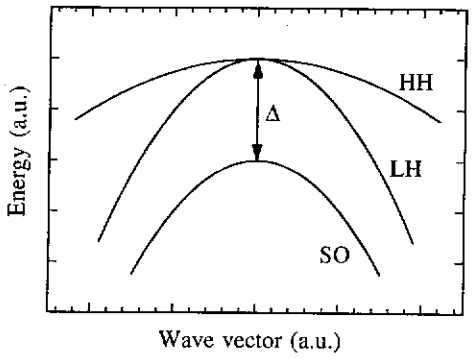

FIG. 27. Schematic of the valence-band structure of most common semiconductors at the Γ point. HH, LH, and SO indicate heavy-hole, light-hole, and spin-orbit split-off band, respectively. The splitting due to the spin-orbit interaction is Δ.

semiconductors. In a quantum well the degeneracy of the HH and LH bands at $\mathbf{k}_\perp = 0$ is removed due to the different effective masses, which results in different binding energies (see Fig. 28). Yet (for QWs grown in the (001) direction) they are still decoupled from each other at $\mathbf{k}_\perp = 0$ and thus the energetic positions of the subband edges can be obtained from a simple one-band calculation for HH and LH separately (as long as the SO band is neglected; for more details, see below).

The nonparabolicity of the conduction band is usually described with Kane's model, where the six (including spin) valence bands and two (or more) conduction bands are taken into account (8×8 $\mathbf{k}\cdot\mathbf{p}$ model). This procedure, however, leads to an free-electron like heavy-hole mass (with the wrong curvature) and is therefore not well suited to describe the valence band. Instead, the Luttinger–Kohn (LK) model (Luttinger and Kohn, 1955)

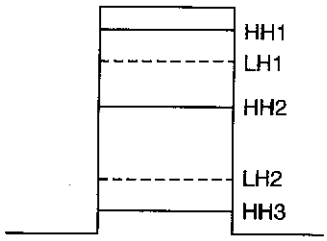

FIG. 28. Subbands of a typical valence-band quantum well (e.g., in GaAs). The energetical order of the HH and LH subbands depends on the QW thickness (see later in the text).

is appropriate; here, only the six valence bands are treated exactly, but the interaction with remote bands is taken into account perturbatively to second order in $\mathbf{k}\cdot\mathbf{p}$ (for the energies; to first order for the wave functions). This interaction gives rise to a finite heavy-hole mass and to the warping of the constant-energy surfaces.

Due to its crucial importance for calculating the valence-band structure and, of course, also intersubband transitions in the valence band, we briefly discuss the Luttinger–Kohn Hamiltonian, although good descriptions can be found in several textbooks. First, the theory is outlined for bulk semiconductors and then extended to quantum wells. The description closely follows the textbook by Chuang (1995).

The Schrödinger equation for the complete Bloch wave function including the spin-orbit interaction is given by (neglecting higher relativistic terms)

$$\left[\frac{p^2}{2m_0} + V(\mathbf{r}) + \frac{\hbar}{4m_0^2c^2}(\nabla V \times \mathbf{p})\cdot\sigma\right]\psi_{\nu\mathbf{k}}(\mathbf{r}) = E_\nu(\mathbf{k})\psi_{\nu\mathbf{k}}(\mathbf{r}) \tag{75}$$

where σ are the Pauli spin matrices. The relevant quantum numbers are the band index ν and the wavevector $\mathbf{k}$. According to the Bloch theorem, the wavefunction $\psi_{\nu\mathbf{k}}(\mathbf{r})$ is written as $\psi_{\nu\mathbf{k}}(\mathbf{r}) = e^{i\mathbf{k}\cdot\mathbf{r}}u_{\nu\mathbf{k}}(\mathbf{r})$, which is introduced in Eq. (75). The lattice-periodic basis functions $u_{\nu\mathbf{k}}(\mathbf{r})$ are expanded as a linear combination of the six zone-center Bloch functions of the hole bands $u_{\nu 0}(\mathbf{r})$ and the remote bands (called set A and set B, respectively):

$$u_{\nu\mathbf{k}}(\mathbf{r}) = \sum_i^A a_i(\mathbf{k})u_{i0}(\mathbf{r}) + \sum_j^B a_j(\mathbf{k})u_{j0}(\mathbf{r}) \tag{76}$$

The six valence bands contained in set A are included exactly, whereas the remote bands in set B are treated perturbatively.

The wave functions near the top of the valence band are p-like, and the bands can be best classified using the total angular momentum $j = l \pm s = 1 \pm 1/2$ and its projection m_z. The basis functions $u_{n0}(\mathbf{r}) = |j, m_z\rangle$ in set A are then explicitly given by (Chuang, 1995)

$$u_{10}(\mathbf{r}) = \left|\frac{3}{2}, \frac{3}{2}\right\rangle = \frac{-1}{\sqrt{2}}|(X + iY)\uparrow\rangle$$

$$u_{20}(\mathbf{r}) = \left|\frac{3}{2}, \frac{1}{2}\right\rangle = \frac{-1}{\sqrt{6}}|(X + iY)\downarrow\rangle + \sqrt{\frac{2}{3}}|Z\uparrow\rangle$$

$$
\begin{aligned}
u_{30}(\mathbf{r}) &= \left|\frac{3}{2}, \frac{-1}{2}\right\rangle = \frac{-1}{\sqrt{6}}|(X - iY)\uparrow\rangle + \sqrt{\frac{2}{3}}|Z\downarrow\rangle \\
u_{40}(\mathbf{r}) &= \left|\frac{3}{2}, \frac{-3}{2}\right\rangle = \frac{1}{\sqrt{2}}|(X - iY)\downarrow\rangle \\
u_{50}(\mathbf{r}) &= \left|\frac{1}{2}, \frac{1}{2}\right\rangle = \frac{1}{\sqrt{3}}|(X + iY)\downarrow\rangle + \sqrt{\frac{1}{3}}|Z\uparrow\rangle \\
u_{60}(\mathbf{r}) &= \left|\frac{1}{2}, \frac{-1}{2}\right\rangle = \frac{1}{\sqrt{3}}|(X - iY)\uparrow\rangle - \sqrt{\frac{1}{3}}|Z\downarrow\rangle
\end{aligned}
\tag{77}
$$

The order for the $j = 3/2$ bands is with descending quantum number m_z. Thus u_{10} and u_{40} represent the HH bands, u_{20} and u_{30} the LH bands, and u_{50} and u_{60} the SO bands.

Now the coupling of the lattice-periodic functions $u_{\nu\mathbf{k}}(\mathbf{r})$ ($\nu = 1, \ldots, 6$) to the remote bands of set B can be removed by $\mathbf{k}\cdot\mathbf{p}$ perturbation theory (Löwdin method) via the transformed basis

$$
u_{\nu\mathbf{k}}(\mathbf{r}) = u_{\nu 0}(\mathbf{r}) + \frac{\hbar}{m_0}\sum_{j}^{B}\frac{\langle u_{j0}|\mathbf{k}\cdot\mathbf{p}|u_{\nu 0}\rangle}{E_{\nu 0} - E_{j0}}u_{j0}(\mathbf{r}) \tag{78}
$$

Here $\nu \in A$ and $j \in B$. The $E_{\nu 0}$ and E_{j0} are the respective band-edge energies at the Γ point. There is no sum over set A, since the $\mathbf{k}\cdot\mathbf{p}$ coupling within the valence band vanishes. When this expression is substituted into the Schrödinger equation, one obtains a 6×6 matrix Schrödinger equation

$$
\sum_{\nu'=1}^{6} H_{\nu\nu'}^{\mathrm{LK}}(\mathbf{k})a_{\nu'}(\mathbf{k}) = E(\mathbf{k})a_{\nu}(\mathbf{k}) \tag{79}
$$

where H^{LK} is the Luttinger–Kohn Hamiltonian, which is of the form

$$
H_{\nu\nu'}^{\mathrm{LK}} = E_{\nu 0}\delta_{\nu\nu'} + \sum_{\alpha,\beta} D_{\nu\nu'}^{\alpha\beta}k_\alpha k_\beta \tag{80}
$$

The matrix $D^{\alpha\beta}$ ($\alpha, \beta = x, y, z$), which represents the nondiagonal elements of the LK Hamiltonian and comes from the interaction with the remote bands, plays the role of an inverse effective-mass tensor and is given by

$$
D_{\nu\nu'}^{\alpha\beta} = \frac{\hbar^2}{2m_0}\left[\delta_{\nu\nu'}\delta_{\alpha\beta} + \sum_{j}^{B}\frac{p_{\nu j}^{\alpha}p_{j\nu'}^{\beta} + p_{\nu j}^{\beta}p_{j\nu'}^{\alpha}}{m_0(E_0 - E_j)}\right] \tag{81}
$$

Here E_0 is the average value of the band-edge energies in set A (valence band); its use instead of E_{v0} is an excellent approximation, when the spin-orbit splitting Δ is much smaller than the energy separation from the remote bands.

The total Luttinger–Kohn Hamiltonian matrix then reads

$$H_{vv'}(\mathbf{k}) = -\begin{pmatrix} P+Q & -S & R & 0 & -S/\sqrt{2} & \sqrt{2}R \\ -S^* & P-Q & 0 & R & -\sqrt{2}Q & \sqrt{3/2}S \\ R^* & 0 & P-Q & S & \sqrt{3/2}S^* & \sqrt{2}Q \\ 0 & R^* & S^* & P+Q & -\sqrt{2}R^* & -S^*/\sqrt{2} \\ -S^*/\sqrt{2} & -\sqrt{2}Q^* & \sqrt{3/2}S & -\sqrt{2}R & P+\Delta & 0 \\ \sqrt{2}R^* & \sqrt{3/2}S^* & \sqrt{2}Q^* & -S/\sqrt{2} & 0 & P+\Delta \end{pmatrix} \tag{82}$$

where

$$P = \frac{\hbar^2}{2m_0}\gamma_1(k_x^2 + k_y^2 + k_z^2)$$

$$Q = \frac{\hbar^2}{2m_0}\gamma_2(k_x^2 + k_y^2 - 2k_z^2)$$

$$R = -\frac{\hbar^2\sqrt{3}}{2m_0}\left[\frac{\gamma_2+\gamma_3}{2}(k_x - ik_y)^2 + \frac{\gamma_2-\gamma_3}{2}(k_x + ik_y)^2\right]$$

$$= -\frac{\hbar^2\sqrt{3}}{2m_0}[-\gamma_2(k_x^2 - k_y^2) + 2i\gamma_3 k_x k_y]$$

$$S = \frac{\hbar^2\sqrt{3}}{m_0}\gamma_3(k_x - ik_y)k_z$$

where γ_1, γ_2, and γ_3 are the so-called Luttinger parameters (related to the elements of the matrix D) and describe the influence of the remote bands on the valence band. They can be expressed as a sum over momentum matrix elements between the valence band and the remote bands (compare Eq. (81)). Usually, however, they are not explicitly calculated, but taken from experiments and used as empirical parameters (e.g., to fit the experimentally obtained hole masses), in the same way as the effective mass is introduced in the single-band $\mathbf{k}\cdot\mathbf{p}$ perturbation theory. A closer inspection of the

preceding shows that γ_2 and γ_3 give rise to an anisotropic dispersion (warping) of the valence bands. When the coupling to the SO band is neglected, diagonalization of the Hamiltonian leads to a simple analytical result (see for example Bastard, 1988, p. 54, or other semiconductor physics textbooks).

When $k_x = k_y = 0$, the HH + LH part of the matrix (SO neglected) becomes diagonal. The diagonal elements $P + Q$ and $P - Q$ are proportional to $\gamma_1 - 2\gamma_2$ and $\gamma_1 + 2\gamma_2$, respectively. Thus, these two expressions can be viewed as the inverse effective masses for the heavy and light holes, respectively (note that this cannot be seen so easily when setting, e.g., $k_y = k_z = 0$, since the z direction has been used as quantization axis for the angular momentum).

To solve not the bulk but the quantum well problem, k_z must be replaced by the differential operator $-id/dz$ in Eq. (82), which, however, must be symmetrized before with respect to k_z to ensure Hermiticity. The resulting system of six coupled differential equations has to be solved for the six-component envelope wavefunction F_ν (with proper boundary conditions, see, e.g., Altarelli *et al.*, 1985; Altarelli, 1986):

$$\sum_{\nu'=1}^{6} [H_{\nu\nu'}^{\mathrm{LK}} + V(z)\delta_{\nu\nu'}]F_{\nu n\mathbf{k}_\perp}(\mathbf{r}) = E_{\nu n\mathbf{k}_\perp}F_{\nu n\mathbf{k}_\perp}(\mathbf{r}) \tag{83}$$

Here $V(z)$ is the quantum well potential (the proper offsets for each hole band—HH, LH, and SO—must be taken). Instead of the wavevector component k_z we now have the subband index n as a new quantum number, and $\mathbf{k}_\perp$ is the in-plane vector (k_x, k_y). Thus $E_{\nu n\mathbf{k}_\perp}$ gives the in-plane energy dispersion of the nth subband of the νth band. The envelope function $F_{\nu n\mathbf{k}}(\mathbf{r})$ can be separated into a z-dependent and an in-plane part:

$$F_{\nu n\mathbf{k}_\perp}(\mathbf{r}) = \frac{1}{\sqrt{A}} e^{i(\mathbf{k}_\perp\cdot\mathbf{r})} g_{\nu n\mathbf{k}_\perp}(z) \tag{84}$$

The total wave function is a linear superposition of the six basis functions, where the Fourier transform of $g_{\nu n\mathbf{k}_\perp}(z) = \Sigma_{k_z} g_{\nu n\mathbf{k}_\perp}(k_z)\cdot e^{ik_z z}$ is introduced for convenience (Altarelli, 1986; Chang and James, 1989):

$$\psi_{n\mathbf{k}}(\mathbf{r}) = \sum_{\nu,k_z} g_{\nu n\mathbf{k}_\perp}(k_z) e^{i\mathbf{k}\cdot\mathbf{r}} u_{\nu\mathbf{k}}(\mathbf{r}) \tag{85}$$

with $u_{\nu\mathbf{k}}(\mathbf{r})$ from Eq. (78). With this Fourier transform Eq. (83) is conveniently reduced to an algebraic matrix equation. The probability density (of

the envelope function, i.e., averaged over one lattice constant) along the quantization direction z for a state $(n, \mathbf{k}_\perp)$ is then given by

$$\sum_{\nu=1}^{6} g^*_{\nu n \mathbf{k}_\perp}(z) \cdot g_{\nu n \mathbf{k}_\perp}(z) \tag{86}$$

Several factors should be noted about the Luttinger–Kohn Hamiltonian applied to quantum wells:

1. When the spin-orbit splitting Δ is much larger than all energies of interest, the coupling to the SO band can be neglected. Then the Hamiltonian of Eq. (82) reduces to a 4×4 matrix. This is the case for the lowest subbands in not too narrow GaAs–AlGaAs quantum wells ($\Delta = 340$ meV), but never for Si–SiGe quantum wells, since Δ is as small as 45 meV for Si.
2. As a further simplification, one can put $\gamma_2 = \gamma_3 =: \bar{\gamma} = (\gamma_2 + \gamma_3)/2$ in the expression for R. This is called the axial approximation and removes the valence band warping (i.e., the in-plane dispersion becomes spherical).
3. As a main effect of the confinement, the degeneracy at $\mathbf{k}_\perp = 0$ of the HH and LH bands is lifted. In the 4×4 Hamiltonian (neglecting the SO band), the band-edge energies of the heavy and light holes can be determined separately like in the one-band model, since the Hamiltonian becomes diagonal for $k_x = k_y = 0$. The corresponding effective masses (which are relevant for the confinement energies) are given by

$$\frac{m^z_{\mathrm{HH}}}{m_0} = \frac{1}{\gamma_1 - 2\gamma_2} \quad \text{and} \quad \frac{m^z_{\mathrm{LH}}}{m_0} = \frac{1}{\gamma_1 + 2\gamma_2} \tag{87}$$

Approximate effective masses in the quantum well plane can be obtained by setting $k_z = 0$ and an expansion for small k_x and k_y. The result is

$$\frac{m^{xy}_{\mathrm{HH}}}{m_0} = \frac{1}{\gamma_1 + \gamma_2} \qquad \frac{m^{xy}_{\mathrm{LH}}}{m_0} = \frac{1}{\gamma_1 - \gamma_2} \tag{88}$$

This approximation is never really good, since a finite confinement energy already corresponds to a nonzero value of k_z. Note that these expressions predict a light in-plane mass for the heavy-hole band and vice versa, which inevitably leads to an anticrossing of the light- and heavy-hole subbands at some finite $\mathbf{k}_\perp$ value. Interaction between light and heavy holes also often leads to a negative (electron-like) in-plane

effective mass of some of the subbands. Figure 29 shows the hole subband dispersion along the (100) and (110) directions for a 50-Å-wide GaAs–AlAs quantum well, calculated with the full 6×6 LK Hamiltonian. The negative mass of the LH subbands is clearly observed. Near $k_\perp = 0.035\,\text{Å}^{-1}$ there is an anticrossing between the HH1 and LH1 states. The LH2 and HH3 states interact strongly near $k_\perp = 0$.

The energetic order of the HH and LH bands is determined by the confinement effective masses and the quantum well width. In GaAs QWs, the LH1 subband is below the HH2 subband for narrow wells (since in the extreme quantum limit, only one HH and one LH state are bound), while

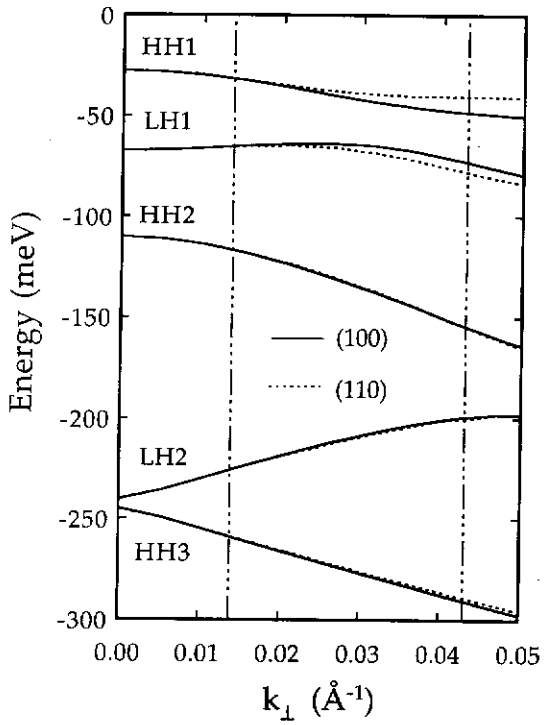

FIG. 29. In-plane hole–subband dispersions of a 50-Å-wide GaAs–AlAs quantum well calculated with the 6×6 Luttinger-Kohn theory along the (100) (solid curves) and (110) (dotted curves) directions. The vertical dash-dotted lines indicate the Fermi wavevector for $p = 3 \times 10^{11}\,\text{cm}^{-2}$ and $p = 3 \times 10^{12}\,\text{cm}^{-2}$, respectively. The character (HH, LH) of each subband at $\mathbf{k}_\perp = 0$ is indicated.

there is a crossover around $L = 190$ Å (Schulman and Chang, 1985). In asymmetric QW potentials, one would observe the lifting of the twofold spin degeneracy for $k_\perp \neq 0$.

Many quantum well systems are built from strained heterostructures, such as $Si–Si_{1-x}Ge_x$ or $In_xGa_{1-x}As–Al_yGa_{1-y}As$. In this case, strain terms must be added to the LK Hamiltonian following Pikus and Bir (1960) and Bir and Pikus (1974), which leads to a lifting of the HH–LH degeneracy at $\mathbf{k} = 0$. For biaxially strained QWs this yields additional terms for the diagonal elements of the HH and LH bands, leading to a shift of the respective band edges (which can change the order of HH and LH subbands) as well as a nondiagonal term, coupling the LH and SO bands (People and Sputz, 1990; Fromherz *et al.*, 1994; Chuang, 1995). In tensile strained QWs the ground state can be a light–hole subband (Xie *et al.*, 1991b, Stoklitsky *et al.*, 1994, 1995).

Now we proceed to the next step, the calculation of the optical matrix elements for intersubband transition in the valence band (Chang and James, 1989; People *et al.*, 1992a, 1992b, Fromherz *et al.*, 1994; Szmulowicz and Brown, 1995; Kim and Majerfeld, 1995; Tsang and Chuang, 1995). Here we restrict ourselves to the 4×4 LK Hamiltonian neglecting the spin-orbit interaction. The matrix elements of the momentum operator between the complete wavefunctions $\psi_{n\mathbf{k}}$ have to be taken ($\mathbf{k} = \mathbf{k}'$ during a transition)

$$\frac{\hbar}{m_0}\mathbf{e}\cdot\mathbf{p}_{nn'} = \left\langle \psi_{n\mathbf{k}} \left| \frac{\hbar}{m_0}\mathbf{e}\cdot\mathbf{p} \right| \psi_{n'\mathbf{k}} \right\rangle \tag{89}$$

Due to the formal analogy of the expression $\mathbf{e}\cdot\mathbf{p}$ with $\mathbf{k}\cdot\mathbf{p}$, the matrix element can be expressed through the inverse-mass tensor elements $D^{ij}_{\nu\nu'}$ of the LK Hamiltonian (Chang and James, 1989; Kim and Majerfield, 1995):

$$\frac{\hbar}{m_0}\langle u_{\nu\mathbf{k}}|\mathbf{e}\cdot\mathbf{p}|u_{\nu'\mathbf{k}}\rangle = \sum_{i,j}(D^{ij}_{\nu\nu'} + D^{ji}_{\nu\nu'})e_i k_j \tag{90}$$

Separating terms containing k_z (which actually becomes $-id/dz$) from the rest it can be shown that the preceding can be written in the form

$$\frac{\hbar}{m_0}\mathbf{e}\cdot\mathbf{p}_{nn'} = \mathbf{e}\cdot\sum_{\nu,\nu'=1}^{4}(\mathbf{I}_{\nu\nu'}Q^{nn'}_{\nu\nu'} + \mathbf{J}_{\nu\nu'}R^{nn'}_{\nu\nu'}) \tag{91}$$

Here the indices ν and ν' go over the four (or six) valence bands, whereas n and n' indicate the respective subband levels. Note that $Q^{nn'}_{\nu\nu'}$ and $R^{nn'}_{\nu\nu'}$ have nothing to do with Q and R of Eq. (82). The preceding quantities are given

by

$$\mathbf{e}\cdot\mathbf{I}_{vv'} = \sum_{i=x,y,z} e_i(D^{ix}_{vv'} + D^{xi}_{vv'})k_x + (D^{iy}_{vv'} + D^{yi}_{vv'})k_y$$

$$\mathbf{e}\cdot\mathbf{J}_{vv'} = \sum_{i=x,y,z} e_i(D^{iz}_{vv'} + D^{zi}_{vv'})$$

and

$$Q^{nn'}_{vv'} = \int dz F^*_v(n, \mathbf{k}_\perp, z) F_{v'}(n', \mathbf{k}_\perp, z)$$

$$R^{nn'}_{vv'} = \int dz F^*_v(n, \mathbf{k}_\perp, z)\left(-i\frac{d}{dz}\right) F_{v'}(n', \mathbf{k}_\perp, z) \tag{92}$$

The index i extends over the Cartesian components and represents the dot product. These terms of the transition matrix elements $\mathbf{p}_{nn'}$ can be written in the form of the following matrix, which contains the Luttinger parameters, γ_i, explicitly (Kim and Majerfeld, 1995):

1. x polarization

	HH(3/2)	HH(−3/2)	LH(1/2)	LH(−1/2)
HH(3/2)	$\hbar k_x(\gamma_1+\gamma_2)Q^{nn'}$	0	$-\sqrt{3}\hbar\gamma_3 R^{nn'}$	$-\sqrt{3}\hbar(\gamma_2 k_x - i\gamma_3 k_y)Q^{nn'}$
HH(−3/2)	0	$\hbar k_x(\gamma_1+\gamma_2)Q^{nn'}$	$-\sqrt{3}\hbar(\gamma_2 k_x + i\gamma_3 k_y)Q^{nn'}$	$\sqrt{3}\hbar\gamma_3 R^{nn'}$
LH(1/2)	$-\sqrt{3}\hbar\gamma_3 R^{nn'}$	$-\sqrt{3}\hbar(\gamma_2 k_x - i\gamma_3 k_y)Q^{nn'}$	$\hbar k_x(\gamma_1-\gamma_2)Q^{nn'}$	0
LH(−1/2)	$\sqrt{3}\hbar(\gamma_2 k_x + i\gamma_3 k_y)Q^{nn'}$	$\sqrt{3}\hbar\gamma_3 R^{nn'}$	0	$\hbar k_x(\gamma_1-\gamma_2)Q^{nn'}$

(93)

The y polarization or any linear superposition would be analogous.

2. z polarization

	HH(3/2)	HH(−3/2)	LH(1/2)	LH(−1/2)
HH(3/2)	$\hbar(\gamma_1-2\gamma_2)R^{nn'}$	0	$-\sqrt{3}\hbar\gamma_3(k_x+ik_y)Q^{nn'}$	0
HH(−3/2)	0	$\hbar(\gamma_1-2\gamma_2)R^{nn'}$	0	$\sqrt{3}\hbar\gamma_3(k_x-ik_y)Q^{nn'}$
LH(1/2)	$-\sqrt{3}\hbar\gamma_3(k_x-ik_y)Q^{nn'}$	0	$\hbar(\gamma_1+2\gamma_2)R^{nn'}$	0
LH(−1/2)	0	$\sqrt{3}\hbar\gamma_3(k_x+ik_y)Q^{nn'}$	0	$\hbar(\gamma_1+2\gamma_2)R^{nn'}$

(94)

For easier reading, the lower indices (vv') are suppressed in $R^{nn'}_{vv'}$ and $Q^{nn'}_{vv'}$, since the corresponding band (HH, LH) is already clear from the respective

row and column of the matrix. Note that now the bands have not been ordered by descending angular momentum component, but have been grouped into heavy and light holes.

Let us now try to get some understanding of the transition matrix elements and selection rules. According to Eqs. (93) and (94) there are two types of contributions:

The terms containing $\mathbf{J}R^{nn'}$: These contain a dipole matrix element of the envelope function ($R^{nn'}$). Due to the dipole matrix element only transitions between states of different parity are allowed. Since they are not proportional to $\mathbf{k}_\perp$, they are allowed at $\mathbf{k}_\perp = 0$. That these terms correspond to "usual" intersubband transitions, like in the conduction band, can be seen in the following way: $\mathbf{J}$ contains only elements of the D tensor with a z component (Eq. (92)), so it couples z- or xy-polarized radiation to an intersubband transition, analogous to the situation in an ellipsoidal conduction valley (compare Eq. (70)). Looking up the HH–HH transition in z polarization (Eq. (94)), one sees that the transition matrix element is proportional to $(\gamma_1 - 2\gamma_2) \cdot R^{nn'}$, which is just the inverse heavy-hole confinement mass (Eq. (87)) times the dipole matrix element, identical to intersubband absorption in a spherical conduction band. The same is true for LH–LH transitions. In addition, however, HH–LH transitions are allowed in xy polarization.

The terms containing $\mathbf{I}Q^{nn'}$: They contain an overlap integral between envelope wave functions, and thus only transitions between states of the same parity are allowed. Furthermore, they are proportional to $\mathbf{k}_\perp$, and are thus allowed only for $\mathbf{k}_\perp \neq 0$. Looking at Eqs. (93) and (94) one can see that HH–HH, LH–LH, and HH–LH transitions arise from these terms in xy polarization, but only HH–LH transitions in z polarization. These transitions are a specific feature of the valence band, and they originate from interband coupling to the remote bands (the direct interband coupling between different valence bands vanishes).

Finally the 2D absorption coefficient is given by analogue to Eq. (18)

$$\alpha_{2D} = \frac{\pi e^2}{\varepsilon_0 c \eta \omega m_0^2 A} \sum_{n,n'} \sum_{\mathbf{k}_\perp} |\mathbf{e} \cdot \mathbf{p}_{nn'}(\mathbf{k}_\perp)|^2 \cdot [f(E_n(\mathbf{k}_\perp)) - f(E_{n'}(\mathbf{k}_\perp)] \cdot \frac{\Gamma/\pi}{[E_n(\mathbf{k}_\perp) - E_{n'}(\mathbf{k}_\perp) - \hbar\omega]^2 + \Gamma^2} \tag{95}$$

From this discussion, we see that both the dipole and the overlap terms give rise to normal-incidence intersubband absorption. For illustration, the

calculated absorption spectrum of the previously discussed 50-Å-wide GaAs–AlAs QW is shown in Fig. 30 for both polarizations and for two different hole concentrations of 3×10^{11} and $3 \times 10^{12}\,\mathrm{cm}^{-2}$. The relevant transitions can be identified with the help of Fig. 29, where the corresponding Fermi wavevectors have been indicated by the dash-dotted vertical

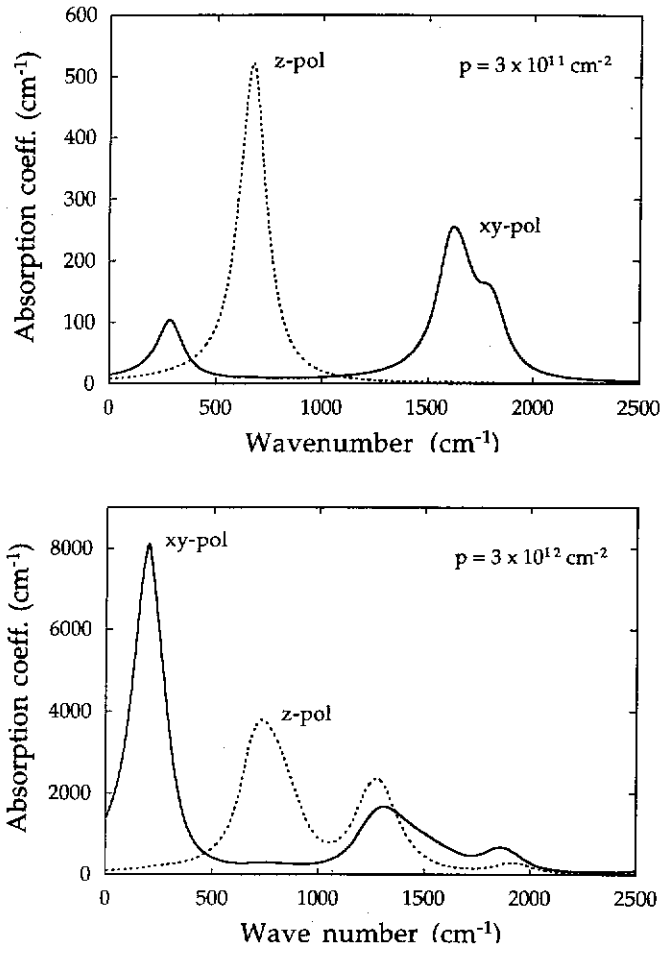

FIG. 30. Calculated absorption spectrum of the GaAs–AlAs quantum well of Fig. 29 for two different hole densities, $p = 3 \times 10^{11}\,\mathrm{cm}^{-2}$ (upper panel) and $p = 3 \times 10^{12}\,\mathrm{cm}^{-2}$ (lower panel). The spectra for z and xy polarization are represented by the dotted and full curves, respectively. For a discussion, see text.

ssed 50-Å-wide
ns and for two
$^{-2}$. The relevant
the correspond-
-dotted vertical

2500

2500

m well of Fig. 29 for
3×10^{12} cm^{-2} (lower
otted and full curves,

lines. (For ease of calculation, k-space integration was not performed over the complete 2D space, but only along several representative directions with proper averaging). The z-polarized peak at 700 cm^{-1} (87 meV) results from the HH1–HH2 transition. At 10 times higher hole concentration, it is (nearly) 10 times stronger, since the corresponding matrix element is independent of $\mathbf{k}_\perp$. This is the "usual" intersubband transition. The broadening at higher density is due to the nonparabolic dispersion. The xy-polarized HH1–LH1 transition occurs at 280 cm^{-1} (35 meV). Since its matrix element is proportional to $\mathbf{k}_\perp$, its size increases stronger than linear with the hole concentration, and in the lower panel it has become stronger than the HH1–HH2 transition. The doublet around 1700 cm^{-1} (or 210 meV, upper panel) is due to the HH1–LH2, HH3 transition, which latter are strongly mixed due to their proximity. The HH1–LH2 transition is allowed at $\mathbf{k}_\perp = 0$ for xy polarization, but in z polarization its strength is proportional to $\mathbf{k}_\perp$, so it appears only at high density (lower panel). The strength of the HH1–HH3 transition should be proportional to $\mathbf{k}_\perp$, but due to the strong mixing of the HH3 with the LH2 state, it can already be observed at low hole density. One has to keep in mind that a clear assignment of a specific subband to a band type (HH, LH, or SO) can strictly be done only at $\mathbf{k}_\perp = 0$. For $\mathbf{k}_\perp \neq 0$ the wave functions become strong mixtures of all basis states and thus basically all transitions become allowed to some degree.

Similar calculations were carried out for various material systems by Man and Pan (1992), Xie *et al.* (1991b, 1992c), and Stoklitsky *et al.* (1994, 1995). Chun *et al.* (1993) included many-body effects such as the depolarization shift properly into the multiband model. Corbin *et al.* (1994) employed a full-scale pseudopotential calculation for computing band structure and absorption of p-type QWs.

There have been a number of intersubband absorption studies in p-type quantum wells, interestingly mostly in Si–SiGe QWs (Park *et al.*, 1992; Fromherz *et al.*, 1994; Boucaud *et al.*, 1995; Zanier *et al.*, 1995). The reason is that in this material system p-type QWs are more easily achieved than n-type QWs (Wang and Karunasiri, 1993). Clear experimental identification of the various valence-band intersubband transitions has, however, remained rather scarce (Fomherz *et al.*, 1996), in part due to the large broadening one usually has in p-type quantum wells. Moreover, most experimental investigation were performed in structures where the final states of the strongest transitions already lie in the continuum, as desired for detector applications (Levine *et al.*, 1991; Wang *et al.*, 1994b; Szmulowicz and Brown, 1995), which leads to additional broadening. Often only photocurrent, but no transmission measurements have been performed on such samples. There have been two reports on far-infrared hole–intersub-

band absorption in relatively wide GaAs quantum wells (Shayasteh *et al.*, 1996; Cole *et al.*, 1996).

As an example, the transmission spectrum of a modulation doped Si–$Si_{0.71}Ge_{0.29}$ multiquantum well structure is shown in Fig. 31 (Helm *et al.*, 1997). Both *p*- and *s*-polarized spectra (full curves) were obtained by normalizing the transmission against the transmission of an undoped Si substrate in the same polarization. By comparing with a calculation as already outlined, but including an electromagnetic simulation of the waveguide transmission (lines with open symbols), one can identify the main absorption features. In *s* polarization, the absorption at $400\,cm^{-1}$ corre-

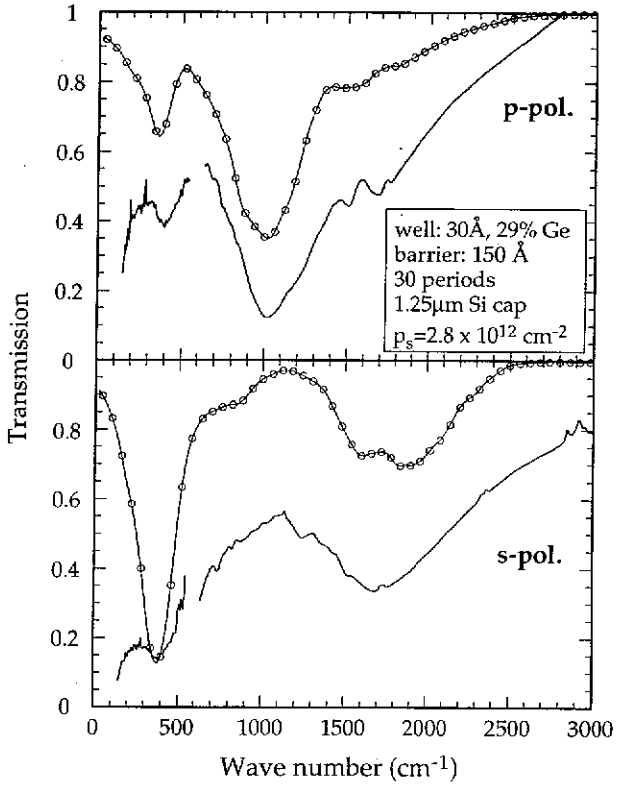

FIG. 31. Polarization dependent waveguide transmission spectrum (at $T = 10\,K$) of a Si–SiGe multiquantum well, as described in the inset. Solid curves: experiment; lines with open symbols: calculation. Note that the *s* polarization contains only *xy* components, whereas the *p* polarization contains both *z* and *xy* components. For a discussion, see text (from Helm *et al.*, 1997).

hayasteh *et al.*,

ion doped Si–
31 (Helm *et al.*,
e obtained by
an undoped Si
calculation as
on of the wave-
entify the main
00 cm^{-1} corre-

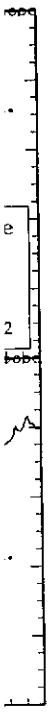

(at $T = 10$ K) of a
ment; lines with open
onents, whereas the p
xt (from Helm *et al.*,

sponds to the HH1–LH1 transition, and the broad minimum around 1800 cm^{-1} stems from transitions to a continuum SO subband (with admixtures of HH and LH character). The p-polarized spectrum shows a strong absorption at 1000 cm^{-1}, which can be identified as the "usual" HH1–HH2 intersubband transition. For the interpretation of the additional features one has to keep in mind that p-polarized light contains both z and xy (in-plane) electric-field components, so these features are the same as in the s-polarized spectrum. Note that the spectra (s polarization in particular) contain a background that can be ascribed to free-carrier absorption.

X. Line Broadening and Relaxation

So far we have dealt with the mechanism of intersubband absorption in various systems and calculated the absorption coefficient on the basis of Fermi's Golden Rule or including many-body effects. We have, however, not discussed any dissipative processes, which give rise to line broadening and relaxation, but we have simply introduced a phenomenological line-broadening parameter Γ. In this section, we expand somewhat on which mechanisms give rise to the finite linewidth and discuss the experimental situation. The linewidth is an important parameter for many applications; in particular, narrow lines give rise to a larger peak absorption in intersubband detectors or to a larger gain in intersubband lasers. Also any experiments or applications making use of the coherence between quantum mechanical energy levels (see Chapter 2), such as dressed states (Sadeghi *et al.*, 1995) or lasing without inversion (Imamoglu and Ram, 1994), require very narrow absorption lines. On the other hand, energy relaxation, which is described by an intersubband lifetime, is important for the electrical bandwidth of intersubband detectors (where a fast relaxation is desired) or for the possibility of achieving population inversion between subbands and hence for intersubband lasers.

In atomic physics, the relaxation processes in an optical transition are usually described in the framework of the density matrix. One can distinguish between a population decay time T_1, which describes the decay of the diagonal elements of the density matrix, and a polarization (or coherence) decay time T_2, which describes the decay of the nondiagonal elements (Milloni and Eberly, 1988). We assume a Lorentzian line shape

$$L(\hbar\omega) = \frac{\Gamma/\pi}{(E_{21} - \hbar\omega)^2 + \Gamma^2} \tag{96}$$

where Γ is the half width at half maximum, which is composed of two contributions

$$\Gamma = \hbar\left(\frac{1}{2T_1} + \frac{1}{T_2}\right) \tag{97}$$

Note that T_1 contributes only half as strongly as T_2. In atomic physics, T_2 is normally related to elastic collisions, whereas T_1 relates to inelastic collisions and spontaneous photon emission. (Note that the total relaxation time $\hbar/\Gamma$ is sometimes expressed as T_2). In quantum well subbands, the situation is slightly more complicated, since due to the free-electron subband dispersion along k_x and k_y even elastic scattering processes can induce a transition to another subband (at a different $\mathbf{k}_\perp$, however).

Let us now take a look at the various scattering processes in a semiconductor. As for inelastic processes, we have acoustic and optical phonon scattering, the former with a typical time constant of a few 100 ps; the latter, about 1 ps. At low temperatures, when there is no optical phonon population in the crystal, only emission processes are relevant. To emit optical phonons, electrons require a threshold energy of $\hbar\omega_{op}$. So naturally there will be a quite different behavior depending on whether the subband separation E_{21} is larger or smaller than $\hbar\omega_{op}$. Both situations together with the relevant scattering processes for relaxation are sketched in Figs. 32a and 32b. Elastic processes can be, for example, scattering by ionized impurities or scattering from interface roughness. Impurity scattering can be quite effective with a time constant of 1 ps, but in modulation-doped QWs with a large setback of the dopants, the scattering rate is reduced to the order of 10 ps. Interface roughness scattering (with respect to the electron mobility) is known to exhibit a strong L^{-6} dependence on the well width L, becoming significant around $L < 100$ Å (Sakaki *et al.*, 1987). If we now consider a typical GaAs–$Al_{0.3}Ga_{0.7}As$ QW with 100 Å thickness (leading to $E_{21} \approx$ 100 meV), we see that optical phonon emission will be the dominant contribution to T_1 (see Fig. 32a), whereas impurity and interface roughness scattering will determine T_2. We discuss this situation, as well as the more intricate case of wide QWs, where $E_{21} < \hbar\omega_{op}$ (Fig. 32b), in the following.

In the first intersubband absorption experiments on GaAs–AlGaAs QWs with E_{21} of the order of 100 meV the measured full linewidths (FWHM) were of the order of $2\Gamma \approx 10$–20 meV and were attributed to a combined effect of optical phonon emission, impurity scattering (only for well-doped samples), interface roughness, and, for MQW systems, also thickness fluctuations from layer to layer. Later, the material quality was improved significantly, and in 1994 Faist *et al.* (1994b) reported a linewidth of $2\Gamma =$ 2.66 meV. They claimed to have reached the intrinsic broadening limit due

FIG. 32. Schematic
wells, where the energy
$\hbar\omega_{LO}$, respectively. In na
relaxation, whereas in w
acoustic-phonon emissio
ionized-impurity scatteri

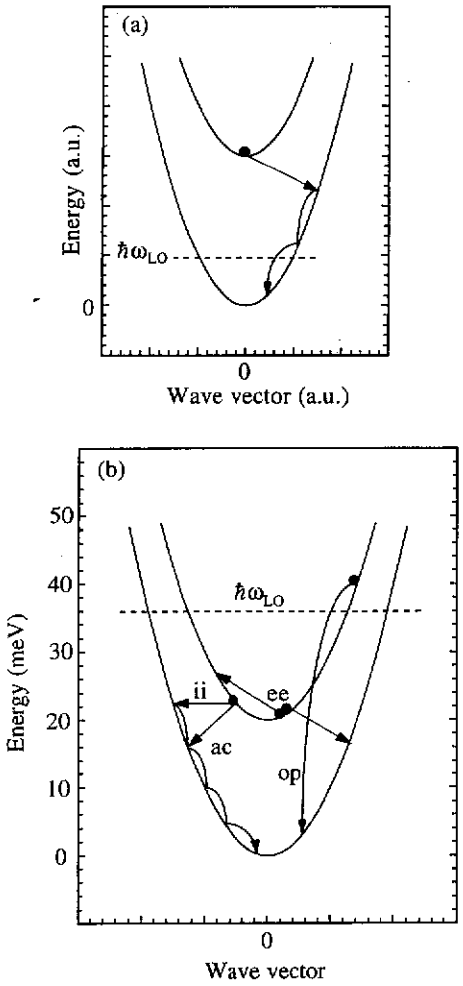

FIG. 32. Schematic view of intersubband relaxation for narrow (a) and wide (b) quantum wells, where the energy separation E_{21} is larger or smaller than the optical phonon energy, $\hbar\omega_{LO}$, respectively. In narrow QWs only optical-phonon emission is relevant for intersubband relaxation, whereas in wide wells several processes play a role: optical phonon emission (op), acoustic-phonon emission (ac), electron-electron scattering (ee), and elastic processes such as ionized-impurity scattering (ii).

to optical phonon emission. Remarkably, the sample was not a square well, but rather an asymmetric coupled MQW system (50 periods), where the 1–3 transition showed this narrow linewidth. Campman *et al.* (1996) conducted another study, showing that a linewidth of $2\Gamma = 2.5$ meV can also be achieved in a 100-Å-wide GaAs–AlGaAs square QW. They demonstrated that, under the same growth conditions, the linewidth increases when the well width gets smaller (to 4.4 meV for 75 Å QW in their study). Optical-phonon scattering, on the other hand, should get stronger for wider QWs, since its strength is proportional to $1/q^2$, with q the momentum transfer. This tendency, together with an evaluation of the optical-phonon scattering rate, led them to conclude that the intrinsic limit has not been reached yet, but should lie around $2\Gamma = 1.2$ meV for a 100-Å well. Interestingly, they found that the electron mobility varies much stronger with the well width than does the intersubband linewidth. Also, the linewidth is not too much affected by using an alloy QW ($In_xGa_{1-x}As$ or $Al_xGa_{1-x}As$ with $x < 10\%$, see Fig. 33). So the conclusion here seems to be that, although technology has driven the quality of QWs close to its intrinsic limit as far as

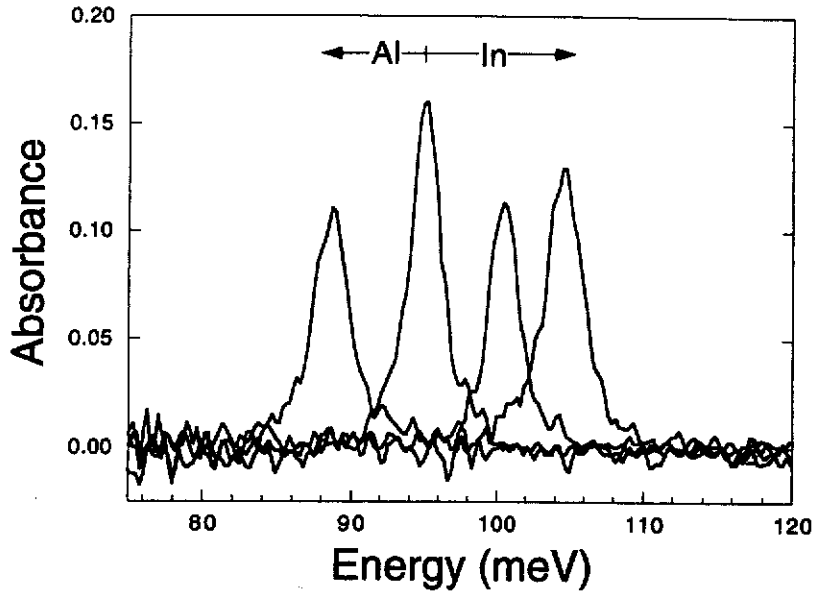

FIG. 33. Measured absorption spectrum of four single 100-Å-wide quantum wells with varying alloy composition. The well materials are (from left to right) $Al_{0.05}Ga_{0.95}As$, GaAs, $In_{0.05}Ga_{0.95}As$, and $In_{0.1}Ga_{0.9}As$, the barrier material is $Al_{0.3}Ga_{0.7}As$ for all samples (from Campman *et al.*, 1996).

not a square well,
ls), where the 1–3
(1996) conducted
neV can also be
hey demonstrated
ıcreases when the
r study). Optical-
:r for wider QWs,
›mentum transfer.
phonon scattering
been reached yet,
Interestingly, they
ith the well width
ı is not too much
As with $x < 10\%$,
hough technology
limit as far as

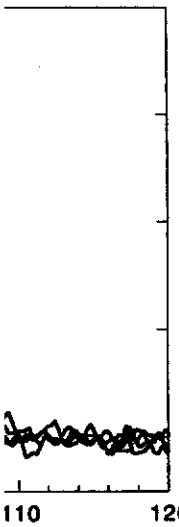

: quantum wells with
$Al_{0.05}Ga_{0.95}As$, GaAs,
for all samples (from

intersubband transitions are concerned, this limit has not been completely reached as yet, leaving some room for improvement. Finally, note that nearly the same as the record linewidth (namely, $2\Gamma = 2.8$ meV) has also been achieved in an MQW system containing 30 periods of 95-Å-wide QWs. This requires extremely accurate long-term control of the molecular beam epitaxy (MBE) growth (Gauer *et al.*, 1995; see also Fig. 35 in Section XI). Although intersubband absorption has been observed in many different material systems to date, the linewidths achieved in GaAs–AlGaAs are still the narrowest. An additional contribution to the linewidth can be due to nonparabolicity, but this has not been unambiguously identified, since it tends to be compensated by many-body effects (see also Section VII and Zaluzny, 1991; von Allmen, 1992; Warburton *et al.*, 1996).

An interesting issue is the question whether intersubband transitions are homogeneously or inhomogeneously broadened. Intrinsic processes such as phonon scattering give rise to homogeneous broadening, but the same is true for scattering by imperfections such as impurities or interface roughness, as long as their lateral length scale is smaller than the characteristic in-plane wavelength of the electrons. A lower bound for this is the Fermi wavelength, which is typically a few 100 Å for $n_s = 10^{11}$–10^{12} cm^{-2}. Compared to this, the mean distance between impurities (in samples doped heavily in the wells) is somewhat smaller than 100 Å. Interface roughness has the same lateral length scale, but only when the interfaces are grown without interruption (for a review, see Herman *et al.*, 1991). Thus both processes will give rise to homogeneous broadening. When the growth is interrupted at the interfaces, however, the lateral length scale can be much larger, up to micrometers. In this case, one can expect some inhomogeneous broadening. The most important sources of inhomogeneous broadening are probably vertical, well-to-well thickness fluctuations in MQW samples with many periods. However, in high-quality MQW structures, the intersubband absorption could be fitted by a Lorentzian line shape, indicating homogeneous broadening (Faist *et al.*, 1994b).

Experiments specifically investigating this issue were reported by Beadie *et al.* (1997) and Vodopyanov *et al.* (1996). Beadie *et al.* (1997) analyzed the saturation behavior in strained, narrow (40-Å) $In_{0.45}Ga_{0.55}As$–$Al_{0.45}Ga_{0.55}As$ MQWs and concluded that both homogeneous and inhomogeneous processes contribute to the line shape. Vodopyanov *et al.* (1996) performed a two-color pump–probe experiment on a somewhat wider (58.5-Å) $In_{0.5}Ga_{0.5}As$–$Al_{0.45}Ga_{0.55}As$ MQW, but could not observe any spectral hole burning; this indicated homogeneous broadening despite the quite large linewidth (>20 meV) of the sample used. A direct measurement of the polarization decay time T_2 in a lattice-matched 60-Å-wide InGaAs/InAlAs QW has been performed by Kaindl *et al.* (1998) by time-

resolved four-wave mixing in the mid-infrared. They found a dephasing time T_2 of a few 100 fs, caused by electron–electron scattering, and could determine the homogeneous contribution to the linewidth to be 4 meV, which was about 30% of the total linewidth.

Thus, this issue has apparently not been completely resolved, but as a preliminary conclusion one can probably say that for very high quality and not too narrow QWs, the intersubband absorption is homogeneously broadened, but for many other structures there is a significant part of inhomogeneous broadening. To conclude this discussion, let us note another fundamentally inhomogeneous (yet intrinsic) broadening mechanism, namely, subband nonparabolicity. This mechanism, however, is hard to track down due to its already mentioned (see Section VII, Subsection 4, Figs. 25 and 26, and Warburton *et al.*, 1996) cancellation through many-body effects (Zaluzny, 1991; von Allmen, 1992; Warburton *et al.*, 1996). Theoretical work (Nikonov *et al.*, 1997) suggests that intersubband absorption in QWs with a large nonparabolicity (such as InAs–AlSb) may be mostly homogeneously broadened due to the collective character of the excitation. This view is also supported through experiments by Warburton *et al.* (1998), demonstrating the need for a microscopic theory of line broadening in intersubband absorption, which does not exist to date. The first step toward such a theory has, however, been published by Ullrich and Vignale (1998).

A lot of effort has also been put into the measurement of the intersubband relaxation time T_1. Experimental techniques reaching from interband (Oberli *et al.*, 1987; Tatham *et al.*, 1989; Levenson *et al.*, 1990; Hunsche *et al.*, 1994; Hartig *et al.*, 1996) or intersubband (Seilmeier *et al.*, 1987; Bäuerle *et al.*, 1988; Elsaesser *et al.*, 1989; Boucaud *et al.*, 1996; Lutgen *et al.*, 1996a, 1996b) time-resolved pump-and-probe measurements with short-pulse lasers to steady-state absorption saturation measurements (Julien *et al.*, 1988, erratum 1993; Faist *et al.*, 1993b; Cui *et al.*, 1993; West and Roberts, 1994) have been employed. Whereas initially the relaxation time was somewhat overestimated (Seilmeier *et al.*, 1987) due to the specific sample design, there seems to be agreement now that the intersubband relaxation time is of the order of 0.3 to 0.6 ps for GaAs QWs with E_{21} of the order of 100 meV. This would be in agreement with a intrinsic lifetime broadening of $2\Gamma = 2 \cdot \hbar/2T_1 = 1.1$ to 2.2 meV.

In wide quantum wells with $E_{21} < \hbar\omega_{op}$ the situation is totally different. Optical phonon emission is irrelevant for the linewidth, but also, monolayer thickness fluctuations play only a minor role (for a 400-Å QW, thickness fluctuations about one monolayer contribute only 0.1 meV to the linewidth). This is the reason that linewidths of $2\Gamma < 1.5$ meV (Helm *et al.*, 1991) have been readily achieved even with samples that were doped in the QWs. Here,

most likely impurity scattering was the dominant broadening mechanism. In such samples, the intersubband linewidth is also correlated with the electron mobility. Thus, it is obvious that the absorption lines can be made narrower by modulation doping with a large setback (thick spacer layer). In this way, linewidths of $2\Gamma = 0.8$ meV ($=6.5\,\mathrm{cm}^{-1}$) have been achieved in multiquantum wells (Fig. 34) and of $2\Gamma = 0.3$ meV in single-period QW systems (Craig *et al.*, 1994, 1996). It is likely that remote-impurity scattering is responsible for this, but also interface roughness comes back into play in this regime.

As far as intersubband lifetime and energy relaxation in wide QWs are concerned, the situation has been far from well understood until recently, and a wide range of lifetimes from a few picoseconds to a few 100 ps were reported (Oberli *et al.*, 1987; Levenson *et al.*, 1990; Faist *et al.*, 1994b; Heyman *et al.*, 1995, 1996; Murdin *et al.*, 1994; Luo *et al.*, 1997; Hartig *et al.*, 1998). These values were again achieved by a variety of time-resolved and steady-state experimental methods. The possible relaxation channels are sketched in Fig. 32b. In principle, acoustic-phonon emission is the only

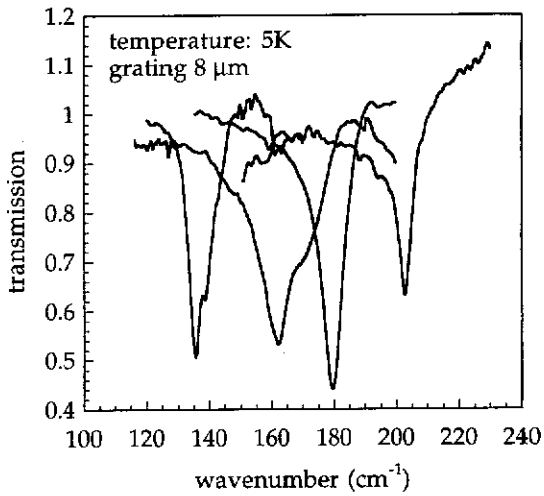

FIG. 34. Transmission spectra of wide modulation-doped GaAs–$Al_{0.3}Ga_{0.7}As$ multiquantum wells with thicknesses of 250, 280, 300, and 320 Å and an electron concentration of $2\text{–}3 \times 10^{11}\,\mathrm{cm}^{-2}$, measured with a grating coupler. The high-energy shoulders in the two low-energy curves are most likely due to well-thickness variations in the MQW, thus these two lines are inhomogeneously broadened, whereas the two lines at higher energy appear to be mostly homogeneously broadened (courtesy of G. Strasser).

energy-dissipating process in this regime at low temperatures and leads to a theoretical lifetime of a few 100 ps. Time-resolved pump-probe measurements conducted with the far-infrared free-electron laser (FELIX) as well as careful analysis of previous experiments have, however, shed new light on this problem (Murdin *et al.*, 1997). It has been found that the measured lifetime depends strongly on the experimental situation, such as the lattice temperature T_L of the sample and the optical excitation intensity I. Both high T_L and high I lead to a strong reduction of the measured lifetime. This can be interpreted in terms of the heating and cooling of a hot electron distribution. For high T_L or strong pumping a high electron temperature is reached within less than a picosecond due to electron-electron scattering (Dür *et al.*, 1996; Lee and Galbraith, 1997). Some electrons from the tail of this distribution can then relax by emitting optical phonons, thus giving rise to a shorter relaxation time (Lee *et al.*, 1995). This cooling takes place until an electron temperature of around $T_e = 35$ K is reached. Below this temperature, there are not enough electrons in the high-energy tail to emit optical phonons and thus acoustic-phonon emission becomes dominant. For $T_e > 40$ K lifetimes of a few picoseconds and for $T_e < 30$ K of a few 100 ps are measured. A detailed analysis and discussion can be found in Murdin *et al.* (1997).

XI. Other Phenomena Related to Intersubband Transitions

1. Magnetic-Field Effects

When a magnetic field is applied perpendicular to the plane of a quantum well, the magnetic part of the Hamiltonian is decoupled from the electric confinement $V(z)$ and the energy spectrum consists of a ladder of Landau levels for each electric subband. The infrared absorption spectrum then shows cyclotron resonance for in-plane polarized light and intersubband absorption for z polarization. We won't discuss this case here further, since it brings no new aspects concerning the intersubband absorption. The situation is different when the magnetic field is applied in the layer plane or in some tilted direction. In these cases, the cyclotron and electric motions are coupled.

Let us first discuss the geometry, where the magnetic field lies in the plane of the QW layer. The confinement direction is still assumed to be the z axis, whereas the magnetic field points along the x direction. Using the gauge $\mathbf{A}_B = (0, -eBz, 0)$ (the subscript B is used to distinguish this from the AC vector potential) the Hamiltonian is still separable and its z-dependent part

can be written as

$$H = -\frac{\hbar^2}{2m^*}\frac{\partial^2}{\partial z^2} + \frac{1}{2}m^*\omega_c^2(z - z_0)^2 + V(z) \tag{98}$$

where $\omega_c = eB/m^*$ is the cyclotron frequency and $z_0 = -\hbar k_y/eB$ is the Landau level center coordinate. The electronic motion is clearly determined by two z-dependent effective potentials, the electric confinement, $V(z)$, and the parabolically shaped magnetic confinement. Depending on their relative strength, the motion and the energy levels are electric or magnetic in character.

For small magnetic fields, obeying the condition $\omega_c \ll \omega_{21}$, or equivalently $l \gg L$ (where $l = \sqrt{\hbar/eB}$ is the magnetic length) the electric subbands (and their energy separation) undergo only a small quadratic shift, the diamagnetic shift. When the magnetic field increases ($\omega_c \approx \omega_{21}$), the energy becomes position-dependent and one obtains hybrid magneto-electric subbands (Zawadzki, 1987). In the limit of large magnetic fields ($\omega_c \gg \omega_{21}$) the electron does not feel the electric confining potential anymore and one recovers three-dimensional Landau levels.

It is interesting to calculate the optical matrix elements for magnetic fields so small that the wave functions can be assumed to remain unchanged (Gauer *et al.*, 1995). In the interaction term $(e/m^*)\mathbf{A}\cdot\mathbf{P}$, the canonical momentum $\mathbf{P} = \mathbf{p} - e\mathbf{A}_B$ must be used. The usual, z-polarized intersubband matrix element then reads

$$\frac{eA_z}{m^*}\langle 1|p_z|2\rangle = eA_z\omega_{21}\langle 1|z|2\rangle \tag{99}$$

The matrix element for radiation polarized in the y direction (i.e., in the layer plane), but perpendicular to the magnetic field, is

$$\frac{eA_y}{m^*}\langle 1|p_y - eBz|2\rangle = eA_y\omega_c\langle 1|z|2\rangle \tag{100}$$

since the term containing p_y vanishes. Thus, we get the remarkable result that the in-plane polarized absorption is proportional to the usual intersubband z matrix element, however reduced by a factor ω_c/ω_{21}. Physically, the magnetic field couples the y and z motions of the electrons, thus making normal-incidence absorption possible. This effect has been discussed and experimentally observed by Gauer *et al.* (1995), shown in Fig. 35. (Note the extremely narrow linewidth of $2\Gamma = 2.8$ meV in this sample). When the magnetic field is increased further, the oscillator strength is transferred from the z polarization (intersubband type) to the y polarization (cyclotron resonance), and the magnetic limit is reached. Note also that somewhat

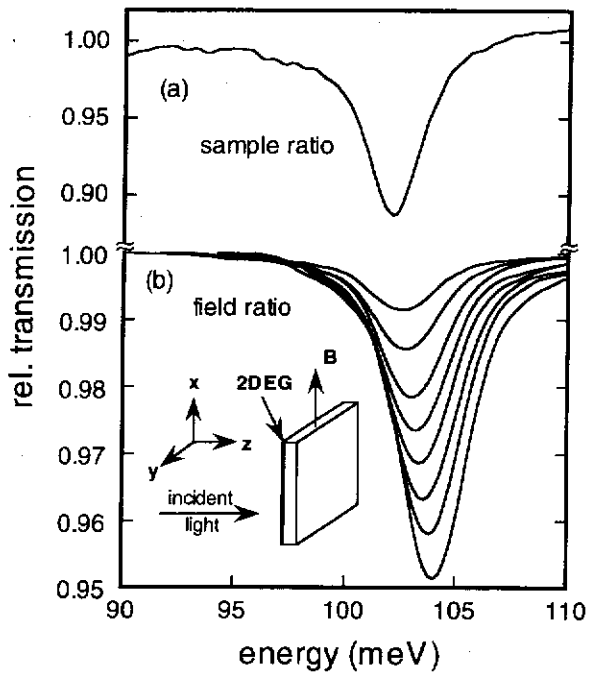

FIG. 35. (a) Intersubband absorption of a 30-period, 95-Å-wide modulation doped GaAs–$Al_{0.35}Ga_{0.65}As$ multiquantum well sample measured under an oblique angle (electron concentration $n_s = 6 \times 10^{11}$ cm^{-2}). (b) The transmission spectra recorded in Voigt geometry with a magnetic field of $B = 6$, 8, 10, 11, 12, 13, 14, and 15 T parallel to the layers (geometry sketched in the inset) (from Gauer *et al.*, 1995).

related experiments were carried out already by Oelting *et al.* (1986) on InSb inversion layers.

For a parabolic potential $V(z)$ the Hamiltonian, Eq. (98), becomes particularly simple, since it consists of the sum of two harmonic oscillators. Then an exact solution can even be obtained for an arbitrarily tilted magnetic-field direction (Maan, 1984; Merlin, 1987). Other properties of parabolic quantum wells are discussed in the following subsection.

If the magnetic field is tilted from the surface-normal (the z direction) by only a small angle θ, a small coupling is induced between the electric subbands and the Landau levels. This leads to an anticrossing and an absorption line doublet near resonance (at $\hbar\omega_c = E_{21}$), which can be observed in a normal-incidence absorption experiment. This was the method that actually provided the first evidence of the subbands in a GaAs–AlGaAs

heterostructure (Schlesinger *et al.*, 1983). Later, this technique was applied by a number of authors for intersubband spectroscopy on 2D systems (Rikken *et al.*, 1986; Wieck *et al.*, 1987, 1989; Ensslin *et al.*, 1989; Pillath *et al.*, 1989). In Fig. 36 this anticrossing is observed at $B = 11.25$ T at an energy of 150 cm^{-1} (Fig. 36a) and compared to a direct (grating-coupler induced) intersubband absorption measurement (Fig. 36b), where the resonance occurs at 168 cm^{-1}. This experiment was regarded as a proof that the anticrossing measures the bare energy separation, whereas the intersubband absorption includes the depolarization shift (and exciton correction) (Pillath *et al.*, 1989). However, theory (Zaluzny, 1989) and later experiments (Wixforth *et al.*, 1994) were in contradiction with this and showed that the anticrossing is also affected by the depolarization shift.

Away from the resonance (i.e., for $\hbar\omega_c \neq E_{21}$) again the diamagnetic shift of the intersubband absorption has been observed, but also combined intersubband–cyclotron resonances (Beinvogl and Koch, 1978; Wieck *et al.*, 1988; Batke *et al.*, 1991). These resonances involve intersubband transitions, which are accompanied by a change of the Landau quantum number, so

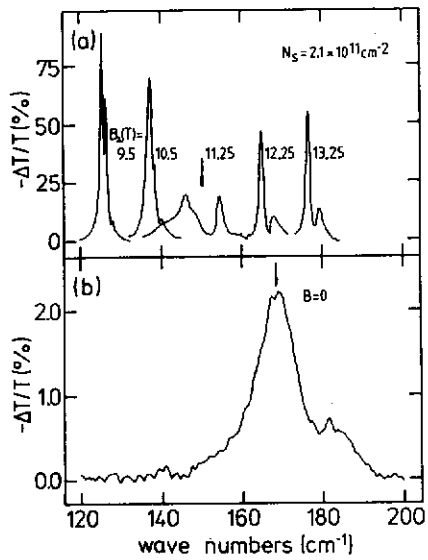

FIG. 36. (a) Cyclotron resonance absorption of a GaAs–AlGaAs heterostructure in a magnetic field slightly tilted from the surface normal. Spectra are plotted for different values of the normal magnetic-field projection, $B_\perp$. At $B_\perp = 11.25$ T a line splitting is observed due to the subband–Landau-level coupling (at 168 cm^{-1}). (b) In comparison, the direct (grating coupled) intersubband absorption peaked at 150 cm^{-1}. The frequency difference is ascribed to the depolarization shift (from Pillath *et al.*, 1989).

they occur at energies of $E = E_{21} \pm n\hbar\omega_c$, where n is an integer. A review of these effects can be found in Batke (1991).

2. PARABOLIC QUANTUM WELLS

At first sight, parabolically shaped quantum wells are not fundamentally different from any other QWs. It turns out, however, that they exhibit some very interesting properties, especially regarding their infrared (IR) absorption properties.

A parabolic potential shape (see Fig. 37) can be achieved by grading the Al content continuously from zero to a certain value; the same can be done using a digitally graded quasi-alloy (Sundaram *et al.*, 1991). In this harmonic-oscillator potential, the energy spectrum consists of equally spaced levels, $E_n = \hbar\omega_0(n + 1/2)$. The oscillator frequency is related to the shape of the parabola by

$$\omega_0 = \sqrt{\frac{8\Delta}{m^* W^2}} \tag{101}$$

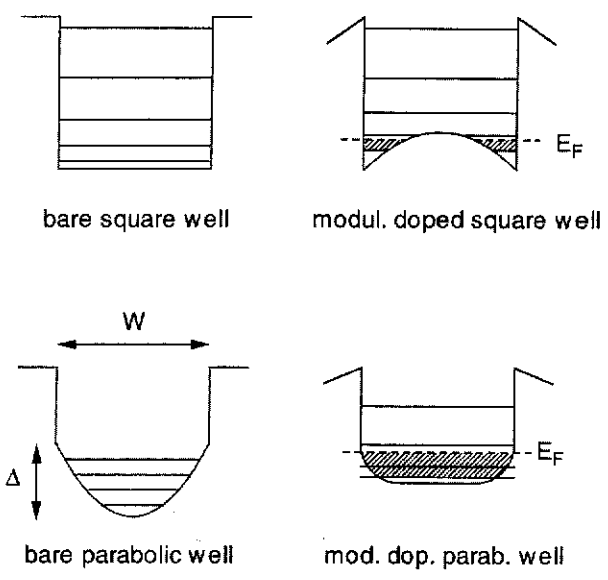

FIG. 37. Schematic of a rectangular (top) and parabolic (bottom) quantum well, before (left) and after (right) introducing electrons through modulation doping. The width W and depth Δ of the parabolic QW are indicated as well as the subbands and the Fermi energy.

where Δ is the depth of the parabola and W is its width (at the top edge). The ratio Δ/W^2 is proportional to the curvature of the parabola. Thus one can expect that a parabolic QW will exhibit resonant intersubband absorption at $\omega = \omega_0$. There is also a remarkable facet to this. Suppose that electrons are introduced in the parabolic QW through modulation doping. As a consequence, the electrons transferred to the well give rise to an additional Hartree potential, which is, according to Poisson's equation, also parabolic and exactly compensates the bare potential over a certain width near the minimum of the parabola, the width depending on the electron density. In this way, a high-mobility quasi-three-dimensional electron system can be tailored (Shayegan *et al.*, 1988), which was the main motivation at the outset of this work. The remarkable phenomenon now is that, no matter how many electrons are located in the parabolic QW and change the self-consistent potential drastically, the resonant absorption always occurs at the bare oscillator frequency ω_0 (Karrai *et al.*, 1989a, 1989b). This is a consequence of the generalized Kohn's theorem (Kohn, 1961; Brey *et al.*, 1989), which states that in a parabolically confined system, the low-frequency excitations are independent of electron-electron interactions, since they only couple to the center-of-mass coordinates of the system. The resonance frequency can also be viewed as the plasma frequency of an 3D electron gas with 3D density $n = 8\varepsilon\varepsilon_0\Delta/e^2W^2$. Figure 37 schematically shows a rectangular and a parabolic quantum well, both before and after introducing carriers through modulation doping.

Such systems were realized based on GaAs–AlGaAs with Δ of the order of 100 meV and W around 1000 Å, leading to a resonance frequency of $\omega_0 \approx 10$ meV. The electron density can be varied with a gate voltage from the low to the mid $10^{11}\,\mathrm{cm}^{-2}$ range. Situations with several occupied subbands were also investigated. Figure 38 shows absorption spectra (Wixforth *et al.*, 1994) of a 2000-Å-wide parabolic QW for three different densities (from 1.6 to $2.5 \times 10^{11}\,\mathrm{cm}^{-2}$). Here a grating coupler was used to couple to the intersubband–plasma resonance (see also Wendler *et al.*, 1997). Deviations from a perfectly harmonic potential usually manifest themselves in the occurrence of additional absorption features (Wixforth *et al.*, 1991).

Other experiments have been performed with a magnetic field applied parallel to the layers (Voigt geometry) or tilted from the surface normal. A detailed account can be found in the review by Wixforth *et al.* (1994).

A nice extension of this concept is realized by embedding a strongly coupled superlattice into a wide parabolic quantum well (Jo *et al.*, 1990), which leads to interesting optical properties (Brey *et al.*, 1990; Streibl *et al.*, 1996).

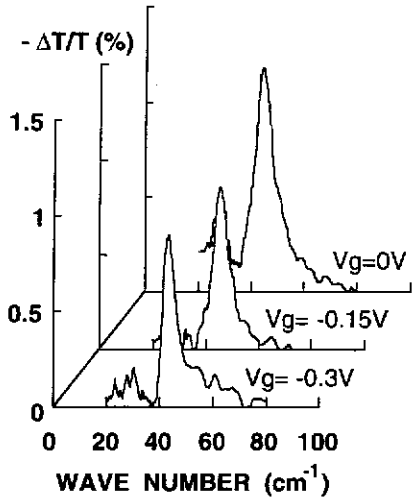

FIG. 38. Absorption spectra of a 200-nm-wide parabolic quantum well for three different gate voltages, as indicated, corresponding to electron concentrations from 1.6 to 2.5 × 10^{11} cm^{-2}. The resonance remains at the same frequency (from Wixforth *et al.*, 1994).

3. IMPURITIES

Although impurities are not really a topic of this chapter, we mention a few things that are related to intersubband transitions.

In a bulk semiconductor the energy levels of shallow donors can be well described in the usual scheme for hydrogen atoms with the quantum numbers N, l (angular momentum), m (magnetic quantum number); that is, the $1s$, $2s$, $2p$ ($m = \pm 1, 0$), $3s$, $3p$ ($m = \pm 1, 0$), $3d$ ($m = \pm 2, \pm 1, 0$), etc., states. In two dimensions, the classification is different, and, for example, the $2p$ state is only twofold degenerate. The exact two-dimensional limit corresponds to a situation with a single subband, and is only of limited relevance for realistic QWs. In a quasi-2D system with several subbands it is still possible and useful to employ the 3D classification, which, however, becomes modified by the QW potential. The breaking of the translation symmetry in the z direction removes the degeneracy of some states (Greene and Bajaj, 1985), which become pinned to higher QW subbands. The subband index n associated with a certain hydrogenic level can be determined by the relation $n = l - |m| + 1$ (Cheng and McCombe, 1990). Correspondingly, the most important levels near the first subband are $1s$, $2p_{\pm 1}$, and near the second subband $2p_0$ and $3d_{\pm 1}$ (for illustration, see Fig. 39).

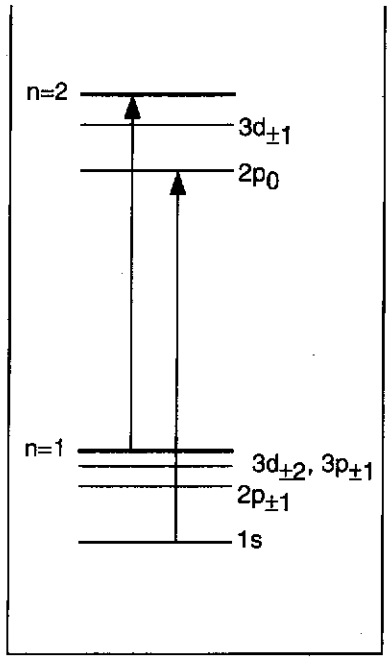

FIG. 39. Schematic of the most important shallow-donor states in a quantum well. The threefold degeneracy of the $2p$ state is lifted and the $2p_0$ state moves up to the second subband, where it becomes the ground state of a new hydrogenic series. Indicated are the intersubband transition and the $1s$–$2p_0$ donor transition. For details, see text.

The $2p_0$ (or $2p_z$) state actually becomes the ground state of the hydrogenic series associated with the $n = 2$ subband. It turns out that optical transitions are allowed for the $1s$–$2p_z$ transitions when the light is polarized perpendicular to the layers. So this transition follows the same selection rule as the usual intersubband transition and also occurs at nearly the same energy, thus it can be regarded as an "impurity-shifted intersubband transition." A difference comes about only through the different (and position dependent) binding energies (Lane and Greene, 1986; Helm *et al.*, 1992) of the donors with respect to the $n = 1$ and $n = 2$ subbands. This is the reason why the $1s$–$2p_z$ transition has been observed only in wide quantum wells, where the donor binding energy is comparable to E_{21} (Helm *et al.*, 1991, 1992), or in superlattices, where it is energetically well separated from the critical points and can actually be used to measure the miniband width of the first and second minibands (Helm *et al.*, 1993). For illustration, we refer back to Fig. 22 in Section VI. For observation of the impurity transition, the doping of

the QWs must also be low enough so that the impurity states ("impurity band") have not completely merged with the conduction band.

4. PHOTON DRAG EFFECT

Finally, we mention an effect, where the momentum transfer rather than the energy transfer from the photon to the electron system is relevant. This is the so-called photon-drag effect (Luryi, 1987; Grinberg and Luryi, 1988; Stockman *et al.*, 1990), which is well known in connection with intervalence band transitions in bulk semiconductors such as Ge, but has also been observed with intersubband transitions (Wieck *et al.*, 1990).

Although the photon momentum q is very small as compared to a typical electron momentum (such as the Fermi momentum k_F), it is not completely negligible. Figure 40 shows the intersubband absorption process taking into account the finite momentum transfer. The energy balance for the absorption process reads

$$\hbar\omega - \hbar\omega_{21} = \frac{\hbar^2}{2m^*}(\mathbf{k}_\perp + \mathbf{q}_\perp)^2 - \frac{\hbar^2\mathbf{k}_\perp^2}{2m^*} \cong \frac{\hbar^2}{m^*}(\mathbf{k}_\perp \cdot \mathbf{q}_\perp) \qquad (102)$$

for $\mathbf{q}_\perp \ll \mathbf{k}_\perp$ ($\mathbf{k}_\perp$ and $\mathbf{k}_\perp + \mathbf{q}_\perp$ are the initial and final in-plane wavevectors, respectively). This can be regarded as a Doppler shift of the resonance

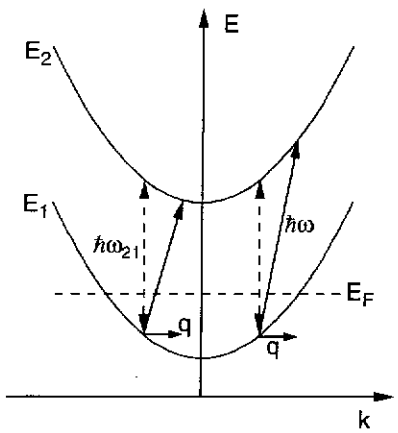

FIG. 40. Illustration of the photon-drag effect in intersubband absorption. The size of the photon momentum q is drawn vastly exaggerated for clarity.

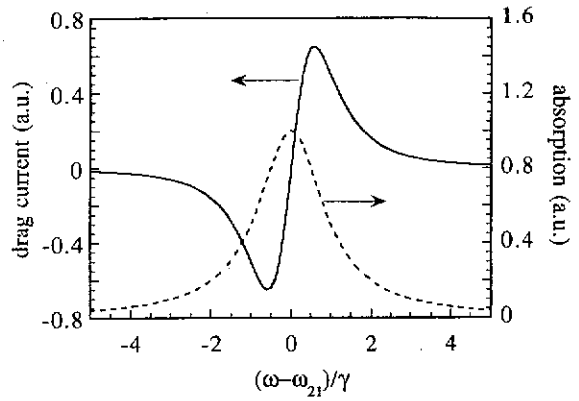

FIG. 41. Dependence of the photon-drag current on the relative detuning, $(\omega - \omega_{21})/\gamma$, calculated for a Lorentzian broadened intersubband transition (solid curve). The absorption line shape (dashed curve) is also shown for comparison.

frequency. The net drag current can be written as

$$\mathbf{j} = -\frac{e\hbar}{m^*}[\tau_2(\mathbf{k}_\perp + \mathbf{q}_\perp) - \tau_1\mathbf{k}_\perp]\cdot\dot{n} \tag{103}$$

where τ_1 and τ_2 are the momentum relaxation times in the first and second subbands, respectively, and $\dot{n}$ is the number of excitations per unit time and area (Sigg, 1992). The two terms correspond to a drag current of an electron in the second subband and a quasi-hole left behind in the first subband, respectively. Obviously, the current will be large, when the two relaxation times are sufficiently different. This is indeed the case in a modulation doped QW with $\hbar\omega_{21} > \hbar\omega_{op}$, the optical phonon energy. Then τ_2 is determined by optical-phonon scattering and is of the order of 0.5 ps, whereas τ_1 is limited by remote impurity scattering and can be 10 times larger. The quasi-holes are then responsible for the drag current, which gives rise to a dispersion-like line shape as a function of detuning, $(\omega - \omega_{21})/\gamma$, where γ is the HWHM of the absorption line (see Fig. 41). Also shown is the absorption coefficient for comparison. This behavior has been observed experimentally (Wieck *et al.*, 1990). Due to the intrinsic speed of the photon drag effect, which is limited only by the momentum relaxation time, it can be used for extremely fast infrared detectors (Sigg *et al.*, 1995).

XII. Concluding Remarks and Outlook

We have attempted to give an introductory overview over the basic physics of intersubband transitions in quantum wells and its present comprehension. Herein a wealth of different aspects of solid state physics and optics have been shown to play a significant role. The thorough understanding achieved to date has enabled researchers to develop useful applications such as infrared detectors and lasers, which are discussed in other chapters of this volume. At present, much research effort is being devoted to the investigation of coherent and quantum optical effects related to intersubband transitions. Among these are microcavities (Duboz, 1996; Berger *et al.*, 1997; Liu, 1997; Faist *et al.*, 1996a; for a survey, see Burstein and Weisbuch, 1995; Rarity and Weisbuch, 1996), Fano-resonances and electromagnetically induced transparency (Imamoglu and Ram, 1994; Faist *et al.*, 1996b; Schmidt and Imamoglu, 1996; Schmidt *et al.*, 1997), and dressed states (Sadeghi *et al.*, 1995). Many of these new developments rely on the similarity of intersubband transitions with atomic transitions. Although the relaxation and dephasing rates in semiconductors are many orders of magnitudes larger than in atoms, the steady improvement of the material quality may render possible the observation of presently unforeseen phenomena.

ACKNOWLEDGMENTS

Most of all, I am grateful to my former graduate student and collaborator Thomas Fromherz, whose help has been invaluable, even after he left academic research. It is my pleasure to acknowledge uncounted hours of discussion with him. Without him, the section concerning the valence band would have never come into existence. I am also grateful to Helga M. Böhm for discussions about and help with many-body theory, to M. Zaluzny for advice about intersubband electromagnetics, and to Rui Yang for discussions on normal-incidence absorption. Special thanks also to S. J. Allen and M. S. Sherwin for their kind hospitality during a one-month stay at the University of California, Santa Barbara, where this chapter was started, and to K. Unterrainer for discussions about many theoretical and experimental aspects. I also want to express my gratitude to H. C. Liu, R. J. Warburton, A. Wixforth, and G. Strasser for providing me with figures from their publications or unpublished data. Finally, I would like to thank my former graduate students W. Hilber, P. Kruck, and M. Seto for their contributions to our joint research, and to G. Bauer for his continuous support and encouragement.

REFERENCES

Abramovich, Y., Poplawski, J., Ehrenfreund, E., Gershoni, D., Brar, B., and Kroemer, H. (1994). *Phys. Rev. B* **50**, 8922.

Ahn, D., and Chuang, S. L. (1986). *Phys. Rev. B* **34**, 9034.

Ahn, D., and Chuang, S. L. (1987). *Phys. Rev. B* **35**, 4149.

Allen, S. J., Tsui, D. C., and Vinter, B. (1976). *Solid State Commun.* **20**, 425.

Altarelli, M. (1986). In *Heterojunctions and Semiconductor Superlattices*, eds. Allan, G., Bastard, G., Boccara, N., Lannoo, M., and Voos, M. (Springer, Berlin), p. 12.

Altarelli, M., Ekenberg, U., and Fasolino, A. (1985). *Phys. Rev. B* **32**, 5138.

Altschul, V. A., Fraenkel, A., and Finkman, E. (1992). *J. Appl. Phys.* **71**, 4382.

Andersson, J. Y., and Lundqvist, L. (1991). *Appl. Phys. Lett.* **59**, 857.

Andersson, J. Y., and Lundqvist, L. (1992). *J. Appl. Phys.* **71**, 3600.

Andersson, J. Y., Lundqvist, L., and Paska, Z. F. (1991). *Appl. Phys. Lett.* **58**, 2264.

Ando, T. (1977a). *Solid State Commun.* **21**, 133.

Ando, T. (1977b). *Z. Phys. B* **26**, 263.

Ando, T., Eda, T., and Nakayama, M. (1977). *Solid State Commun.* **23**, 751.,

Ando, T. (1978). *J. Phys. Soc. Jpn.* **44**, 475.

Ando, T., Fowler, A. B., and Stern, F. (1982). *Rev. Mod. Phys.* **54**, 437.

Asai, H., and Kawamura, Y. (1990). *Appl. Phys. Lett.* **56**, 1149.

Bandara, K. S. M... V., Coon, D. D., Byungsung, O., Lin, Y. F., and Francombe, M. H. (1988). *Appl. Phys. Lett.* **53**, 1931; erratum: (1989). *Appl. Phys. Lett.* **55**, 206.

Bastard, G. (1981). *Phys. Rev. B* **24**, 5693.

Bastard, G. (1982). *Phys. Rev. B* **25**, 7584.

Bastard, G. (1988). *Wave Mechanics Applied to Semiconductor Heterostructures* (Les editions de Physique, Les Ulis, France).

Bastard, G., Mendez, E. E., Chang, L. L., and Esaki, L. (1983). *Phys. Rev. B* **28**, 3241.

Batke, E. (1991). *Festkörperprobleme* (*Adv. Solid State Phys.*) **31**, 297.

Batke, E., Weimann, G., and Schlapp, W. (1989). *Phys. Rev. B* **39**, 11171.

Batke, E., Weimann, G., and Schlapp, W. (1991). *Phys. Rev. B* **43**, 6812.

Bäuerle, R. J., Elsaesser, T., Kaiser, W., Lobentanzer, H., Stolz, W., and Ploog, K. (1988). *Phys. Rev. B* **38**, 4307.

Beadie, G., Rabinovich, W. S., Katzer, D. S., and Goldenberg, M. (1997). *Phys. Rev. B* **55**, 9731.

Beinvogl, W., and Koch, F. (1977). *Solid State Commun.* **24**, 687.

Beinvogl, W., and Koch, F. (1978). *Phys. Rev. Lett.* **40**, 1736.

Berger, V., Vermeire, G., Demeester, P., and Weisbuch, C. (1995). *Appl. Phys. Lett.* **66**, 218.

Berger, V., Duboz, J.-Y., Ducloux, E., Lafon, F., Pavel, I., Boucaud, P., Gauthier-Lafaye, O., Julien, F. H., Tchelnokov, A., and Planel, R. (1997). *Mat. Res. Soc. Symp. Proc.* **450**, 135.

Berreman, D. W. (1963). *Phys. Rev.* **130**, 2193.

Bir, G. L., and Pikus, G. E. (1974). *Symmetry and Strain-Induced Effects in Semiconductors* (Wiley, New York).

Bloss, W. (1989). *J. Appl. Phys.* **66**, 3639.

Boucaud, P., Gao, L., Moussa, Z., Visocekas, F., Julien, F. H., Lourtioz, J.-M., Sagnes, I., Campidelli, Y., and Badoz, P.-A. (1995). *Appl. Phys. Lett.* **67**, 2948.

Boucaud, P., Julien, F. H., Prazeres, R., Ortega, J.-M., Berger, V., Nagle, J., and Leburton, J.-P. (1996). *Electron. Lett.* **32**, 2357.

Boykin, T. B., and Chui, H. C. (1997). *Phys. Rev. B* **55**, 7091.

Braun, M., and Rössler, U. (1985). *J. Phys. C* **18**, 3365.

Brey, L., Johnson, N. F., and Halperin, B. I. (1989). *Phys. Rev. B* **40**, 647.

Brey, L., Johnson, N. F., and Dempsey, J. (1990). *Phys. Rev. B* **42**, 2886.

Brown, E. R., and Eglash, S. J. (1990). *Phys. Rev. B* **41**, 7559.
Brown, E. R., Eglash, S. J., and McIntosh, K. A. (1992). *Phys. Rev. B* **46**, 7244.
Burstein, E., and Weisbuch, C. (eds.). (1995). *Confined Electrons and Photons* (Plenum Press, New York).
Burt, M. G. (1992). *J. Phys. Condens. Matter* **4**, 6651.
Byungsung, O., Choe, J. W., Francombe, M. H., Bandara, K. M. S. V., Coon, D. D., Li, Y. F., and Takei, W. J. (1990). *Appl. Phys. Lett.* **57**, 503.
Campman, K. L., Schmidt, H., Imamoglu, A., and Gossard, A. C. (1996). *Appl. Phys. Lett.* **69**, 2554.
Capasso, F., Sirtori, C., Faist, J., Sivco, D. L., Chu, S.-N. G., and Cho, A. Y. (1992). *Nature* **358**, 565.
Capasso, F., Sirtori, C., and Cho, A. Y. (1994). *IEEE J. Quantum Electron.* **30**, 1313.
Chang, Y.-C., and James, R. B. (1989). *Phys. Rev. B* **39**, 12672.
Chen, W. P., Chen, Y. J., and Burstein, E. (1976). *Surf. Sci.* **58**, 263.
Cheng, J. P., and McCombe, B. D. (1990). *Phys. Rev. B* **42**, 7626.
Chuang, S. L. (1995). *Physics of Optoelectronic Devices* (Wiley, New York).
Chuang, S. L., Luo, M. S.-C., Schmitt-Rink, S., and Pinczuk, A. (1992). *Phys. Rev. B* **46**, 1897.
Chui, H. C., Martinet, E. L., Fejer, M. M., and Harris, J. S., Jr. (1994). *Appl. Phys. Lett.* **64**, 736.
Chun, S. K., and Wang, K. L. (1992). *Phys. Rev. B* **46**, 7682.
Chun, S. K., Pan, D. S., and Wang, K. L. (1993). *Phys. Rev. B* **47**, 15638.
Cohen-Tannoudji, C., Dupont-Roc, J., and Grynberg, G. (1989). In *Photons and Atoms* (Wiley, New York), p. 325–326.
Cole, B. E., Chamberlain, J. M., Henini, M., Nakov, V., and Gobsch, G. (1996). *J. Appl. Phys.* **80**, 6058.
Cole, T., and McCombe, B. D. (1984). *Phys. Rev. B* **29**, 3180.
Corbin, E., Wong, K. B., and Jaros, M. (1994). *Phys. Rev. B* **50**, 2339.
Craig, K., Felix, C. L., Heyman, J. N., Markelz, A. G., Sherwin, M. S., Campman, K. L., Hopkins, P. F., and Gossard, A. C. (1994). *Semicond. Sci. Technol.* **9**, 627.
Craig, K., Galdrikian, B., Heyman, J. N., Markelz, A. G., Williams, J. B., Sherwin, M. S., Campman, K., Hopkins, P. F., and Gossard, A. C. (1996). *Phys. Rev. Lett.* **76**, 2382.
Cui, D., Chen, Z., Pan, S., Lu, H., and Yang, G. (1993). *Phys. Rev. B* **47**, 6755.
Dahl, D. A., and Sham, L. J. (1977). *Phys. Rev. B* **16**, 651.
Davé, D. P., and Taylor, H. F. (1994). *Phys. Lett. A* **184**, 301.
Dingle, R., Wiegmann, W., and Henry, C. H. (1974). *Phys. Rev. Lett.* **33**, 827.
Duboz, J. Y. (1996). *J. Appl. Phys.* **80**, 5432.
Dupont, E., Corkum, P. B., Liu, H. C., Buchanan, M., and Wasilewski, Z. R. (1995). *Phys. Rev. Lett.* **74**, 3596.
Dür, M., Goodnick, S. M., and Lugli, P. (1996). *Phys. Rev. B* **54**, 17794.
Ekenberg, U. (1987). *Phys. Rev. B* **36**, 6152.
Ekenberg, U. (1989). *Phys. Rev. B* **40**, 7714.
Elsaesser, T., Bäuerle, R. J., Kaiser, W., Lobentanzer, H., Stolz, W., and Ploog, K. (1989). *Appl. Phys. Lett.* **54**, 256.
Ensslin, K., Heitmann, D., and Ploog, K. (1989). *Phys. Rev. B* **39**, 10879.
Eppenga, R., Schuurmans, M. F. H., and Colak, S. (1987). *Phys. Rev. B* **36**, 1554.
Esaki, L., and Sakaki, H. (1977). *IBM Techn. Disclosure Bull.* **20**, 2456.
Faist, J., Capasso, F., Hutchinson, A. L., Pfeiffer, L. N., and West, K. W. (1993a). *Phys. Rev. Lett.* **71**, 3573.
Faist, J., Capasso, F., Sirtori, C., Sivco, D. L., Hutchinson, A. L., Chu, S.-N. G., and Cho, A. Y. (1993b). *Appl. Phys. Lett.* **63**, 1354.

Faist, J., Capasso, F., Sivco, D. L., Sirtori, C., Hutchinson, A. L., and Cho, A. Y. (1994a). *Science* **264**, 553.
Faist, J., Sirtori, C., Capasso, F., Pfeiffer, L., and West, K. W. (1994b). *Appl. Phys. Lett.* **64**, 872.
Faist, J., Gmachl, C., Striccoli, M., Sirtori, C., Capasso, F., Sivco, D. L., and Cho, A. Y. (1996a). *Appl. Phys. Lett.* **69**, 2456.
Faist, J., Sirtori, C., Capasso, F., Chu, S.-N. G., Pfeiffer, L. N., and West, K. W. (1996b). *Opt. Lett.* **21**, 985.
Flatté, M. E., Young, P. M., Peng, L. H., and Ehrenreich, H. (1996). *Phys. Rev. B* **53**, 1963.
Fowler, A. B., Fang, F. F., Howard, W. E., and Stiles, P. J. (1966). *Phys. Rev. Lett.* **16**, 901.
Fromherz, T., Koppensteiner, E., Helm, M., Bauer, G., Nützel, J. F., and Abstreiter, G. (1994). *Phys. Rev. B* **50**, 15073.
Fromherz, T., Kruck, P., Helm, M., Bauer, G., Nützel, J. F., and Abstreiter, G. (1996). *Appl. Phys. Lett.* **68**, 3611.
Gauer, C., Wixforth, A., Kotthaus, J. P., Abstreiter, G., Weimann, G., and Schlapp, W. (1995). *Europhys. Lett.* **30**, 111.
Greene, R. L., and Bajaj, K. K. (1985). *Phys. Rev. B* **31**, 4006.
Grinberg, A. A., and S. Luryi, S. (1988). *Phys. Rev. B* **38**, 87.
Goossen, K. W., and Lyon, S. A. (1985). *Appl. Phys. Lett.* **47**, 1257.
Goossen, K. W., Lyon, S. A., and Alavi, K. (1988). *Appl. Phys. Lett.* **53**, 1027.
Gunapala, S. D., Levine, B. F., and Chand, N. (1991). *J. Appl. Phys.* **70**, 305.
Gunnarson, O., and Lundqvist, B. I. (1976). *Phys. Rev. B* **13**, 4274.
Harbecke, B. (1986). *Appl. Phys. B* **39**, 165.
Harbecke, B., Heinz, B., and Grosse, P. (1985). *Appl. Phys. A* **38**, 263.
Hartig, M., Haacke, S., Deveaud, B., and Rota, L. (1996). *Phys. Rev. B* **54**, 14269.
Hartig, M., Haacke, S., Selbmann, P. E., Deveaud, B., Taylor, R. A., and Rota, L. (1998). *Phys. Rev. Lett.* **80**, 1940.
Harwit, A., and Harris, J. S., Jr. (1987). *Appl. Phys. Lett.* **50**, 685.
Hasnain, G., Levine, B. F., Bethea, C. G., Logan, R. A., Walker, J., and Malik, R. J. (1989). *Appl. Phys. Lett.* **54**, 2515.
Haug, H., and Koch, S. W. (1993). *Quantum Theory of the Optical and Electronic Properties of Semiconductors* (World Scientific, Singapore).
Hedin, L., and Lundqvist, B. I. (1971). *J. Phys. C* **4**, 2064.
Heitmann, D., Kotthaus, J. P., and Mohr, E. G. (1982). *Solid State Commun.* **44**, 715.
Heitmann, D., and Mackens, U. (1986). *Phys. Rev. B* **33**, 8269.
Helm, M. (1995). *Semicond. Sci. Technol.* **10**, 557.
Helm, M., Peeters, F. M., DeRosa, F., Colas, E., Harbison, J. P., and Florez, L. T. (1991). *Phys. Rev. B* **43**, 13983.
Helm, M., Peeters, F. M., DeRosa, F., Colas, E., Harbison, J. P., and Florez, L. T. (1992). *Surface Sci.* **263**, 518.
Helm, M., Hilber, W., Fromherz, T., Peeters, F. M., Alavi, K., and Pathak, R. N. (1993). *Phys. Rev. B* **48**, 1601.
Helm, M., Kruck, P., Fromherz, T., Weichselbaum, A., Seto, M., Bauer, G., Moussa, Z., Boucaud, P., Julien, F. H., Loutzioz, J.-M., Nützel, J. F., and Abstreiter, G. (1977). *Thin Solid Films* **294**, 330.
Herman, M. A., Bimberg, D., and Christen, J. (1991). *J. Appl. Phys.* **70**, R1.
Hertle, H., Schuberth, G., Gornik, E., Abstreiter, G., and Schäffler, F. (1991). *Appl. Phys. Lett.* **59**, 2977.
Heyman, J. N., Craig, K., Galdrikian, B., Sherwin, M. S., Campman, K., Hopkins, P. F., Fafard, S., and Gossard, A. C. (1994). *Phys. Rev. Lett.* **72**, 2183.

Heyman, J. N., Unterrainer, K., Craig, K., Galdrikian, B., Sherwin, M. S., Campman, K., Hopkins, P. F., and Gossard, A. C. (1995). *Phys. Rev. Lett.* **74**, 2683.
Heyman, J. N., Unterrainer, K., Craig, K., Williams, J., Sherwin, M. S., Campman, K., Hopkins, P. F., Gossard, A. C., Murdin, B. N., and Langerak, C. J. G. M. (1966). *Appl. Phys. Lett.* **68**, 3019.
Hirayama, Y., Smet, J. H., Peng, L. H., Fonstad, C. G., and Ippen, E. P. (1993). *Appl. Phys. Lett.* **63**, 1663.
Höpfel, R. A., and Gornik, E. (1986). In *Heterojunctions and Semiconductor Superlattices*, eds. Allan, G. *et al.* (Springer, Berlin), p. 84.
Huang, D., Gumbs, G., and Manasreh, M. O. (1995). *Phys. Rev. B* **52**, 14126.
Hunsche, S., Leo, K., Kurz, H., and Köhler, K. (1994). *Phys. Rev. B* **50**, 5791.
Imamoglu, A., and Ram, R. J. (1994). *Opt. Lett.* **19**, 1744.
Jiang, M. Y. (1992). *Solid State Commun.* **84**, 81.
Jo, J., Santos, M., Shayegan, M., Suen, Y. W., Engel, L. W., and Lanzilotto, A. M. (1990). *Appl. Phys. Lett.* **57**, 2130.
Jogai, B. (1991). *J. Vac. Sci. Technol. B* **9**, 2473.
Julien, F. H., and P. Boucaud, P. (1997). In *Optical Spectroscopy of Low-Dimensional Semiconductors*, ed. Abstreiter, G. (Kluwer Academic Publishers, Dordrecht), p. 41.
Julien, F. H., Lourtioz, J.-M., Herschkorn, N., Delacourt, D., Pocholle, J. P., Papuchon, M., Planel, R., and Le Roux, G. (1988). *Appl. Phys. Lett.* **53**, 116; Erratum ibid. (1993) **62**, 2289.
Kaindl, R., Lutgen, S., Woerner, M., Elsaesser, T., Nottelmann, B., Axt, V. M., Kuhn, T., Hase, A., and Künzel, H. (1998). *Phys. Rev. Lett.* **80**, 3575.
Kamgar, A., Kneschaurek, P., Dorda, G., and Koch, J. F. (1974). *Phys. Rev. Lett.* **32**, 1251.
Kane, E. O. (1969). In *Tunneling Phenomena in Solids*, ed. Burstein, E., and Lundqvist, S. (Plenum, New York), p. 1.
Kane, M. J., Emeny, M. T., Apsley, N., Whitehouse, C. R., and Lee, D. (1988). *Semicond. Sci. Technol.* **3**, 722.
Karrai, K., Drew, H. D., Lee, H. W., and Shayegan, M. (1989a). *Phys. Rev. B* **39**, 1426.
Karrai, K., Ying, X., Drew, H. D., and Shayegan, M. (1989b). *Phys. Rev. B* **40**, 12020.
Karunasiri, G., Park, J. S., Chen, J., Shih, R., Scheihing, J. F., and Dodd, M. A. (1995). *Appl. Phys. Lett.* **67**, 2600.
Katz, J., Zhang, Y., and Wang, W. I. (1992). *Appl. Phys. Lett.* **61**, 1697.
Keilmann, F. (1994). *Solid State Commun.* **92**, 223.
Khurgin, J. (1993). *Appl. Phys. Lett.* **62**, 1390.
Kim, B. W., and Majerfeld, A. (1995). *J. Appl. Phys.* **77**, 4552.
Kim, K. T., Lee, S. S., and Chuang, S. L. (1990). *J. Appl. Phys.* **69**, 6617.
Kneschaurek, P., Kamgar, A., and Koch, J. F. (1976). *Phys. Rev. B* **14**, 1610.
Kohn, W. (1961). *Phys. Rev.* **123**, 1242.
Kohn, W., and Sham, L. J. (1965). *Phys. Rev.* **140**, A1133.
Lane, P., and Greene, R. L. (1986). *Phys. Rev. B* **33**, 5871.
Lee, C., and Wang, K. L. (1992). *Appl. Phys. Lett.* **60**, 2264.
Lee, C., and Wang, K. L. (1994). *Appl. Phys. Lett.* **64**, 1256.
Lee, S.-C., Galbraith, I., and Pidgeon, C. R. (1995). *Phys. Rev. B* **52**, 1874.
Lee, S.-C., and Galbraith, I. (1997). *Phys. Rev. B* **55**, R16025.
Lenz, G., and Salzman, J. (1990). *Appl. Phys. Lett.* **56**, 871.
Levenson, J. A., Dolique, G., Oudar, J. L., and Abram, I. (1990). *Phys. Rev. B* **41**, 3688.
Levine, B. F., Malik, R. J., Walker, J., Choi, K. K., Bethea, C. G., Kleinman, D. A., and Vandenberg, J. M. (1987). *Appl. Phys. Lett.* **50**, 273.
Levine, B. F., Gunapala, S. D., Kuo, J. M., Pei, S. S., and Hui, S. (1991). *Appl. Phys. Lett.* **59**, 1864.

Levine, B. F. (1993). *J. Appl. Phys.* **74**, R1.
Lew Yan Voon, L. C., Willatzen, M., and Ram-Mohan, L. R. (1995). *J. Appl. Phys.* **78**, 295.
Lew Yan Voon, L. C., Willatzen, M., Cardona, M., and Ram-Mohan, L. R. (1996). *J. Appl. Phys.* **80**, 600 (Comment); Reply: Peng, L. H., and Fonstad, C. G. (1996). *J. Appl. Phys.* **80**, 603.
Li, H. S., Karunasiri, R. P. G., Chen, Y. W., and Wang, K. L. (1993). *J. Vac. Sci. Technol. B* **11**, 922.
Li, S. S., and Su, Y. K. (1998). *Intersubband Transitions in Quantum Wells: Physics and Devices* (Kluwer Academic Publishers, Dordrecht).
Li, W. J., McCombe, B. D., Chambers, F. A., Devane, G. P., Ralston, J., and Wicks, G. (1990a). *Surf. Sci.* **228**, 164.
Li, W. J., McCombe, B. D., Chambers, F. A., Devane, G. P., Ralston, J., and Wicks, G. (1990b). *Phys. Rev. B* **42**, 11953.
Li, W. J., and McCombe, B. D. (1992). *J. Appl. Phys.* **71**, 1038.
Liu, A. (1994). *Phys. Rev. B* **50**, 8569.
Liu, A. (1997). *Phys. Rev. B* **55**, 7101.
Liu, H. C., Levine, B. F., and Andersson, J. Y. (eds.). (1994). *Quantum Well Intersubband Transition Physics and Devices* (Kluwer Academic Publishers, Dordrecht).
Liu, H. C. (1993). *J. Appl. Phys.* **73**, 3062.
Liu, H. C., Buchanan, M., and Wasilewski, Z. R. (1998). *Appl. Phys. Lett.* **72**, 1682.
Loehr, J. P., and Manasreh, M. O. (1993). In *Semiconductor Quantum Wells and Superlattices for Long-Wavelength Infrared Detectors*, ed. Manasreh, M. O. (Artech House, Boston).
Luo, K., Zheng, H., Lu, Z., Xu, J., Xu, Z., Zhang, T., Li, C., Yang, X., and Tian, J. (1997). *Appl. Phys. Lett.* **70**, 1155.
Luo, M. S.-C., Chuang, S.-L., Schmitt-Rink, S., and Pinczuk, A. (1993). *Phys. Rev. B* **48**, 11086.
Luryi, S. (1987). *Phys. Rev. Lett.* **58**, 2263.
Lutgen, S., Kaindl, R. A., Woerner, M., Elsaesser, T., Hase, A., Künzel, H., Meglio, D., and Lugli, P. (1996a). *Phys. Rev. Lett.* **77**, 3657.
Lutgen, S., Kaindl, R. A., Woerner, M., Elsaesser, T., Hase, A., and Künzel, H. (1996b). *Phys. Rev. B* **54**, 17343.
Luttinger, J. M., and Kohn, W. (1955). *Phys. Rev.* **97**, 869.
Maan, J. C. (1984). In *Two-Dimensional Systems, Heterostructures, and Superlattices*, eds. Bauer, G., Kuchar, F., and Heinrich, H. (Springer, Berlin), p. 183.
Man, P., and Pan, D. S. (1992). *Appl. Phys. Lett.* **61**, 2799.
Manasreh, M. O., Szmulowicz, F., Vaughan, T., Evans, K. R., Stutz, C. E., and Fischer, D. W. (1991). *Phys. Rev. B* **43**, 9996.
McCombe, B. D., Holm, R. T., and Schafer, D. E. (1979). *Solid State Commun.* **32**, 603.
Meney, A. T., Gonul, B., and O'Reilly, E. P. (1994). *Phys. Rev. B* **50**, 10893.
Merlin, R. (1987). *Solid State Commun.* **64**, 99.
Mii, Y. J., Wang, K. L., Karunasiri, R. P. G., and Yuh, P. F. (1990a). *Appl. Phys. Lett.* **56**, 1046.
Mii, Y. J., Karunasiri, R. P. G., Wang, K. L., Chen, M., and Yuh, P. F. (1990b). *Appl. Phys. Lett.* **56**, 1986.
Milonni, P. W., and Eberly, J. H. (1988). *Lasers* (Wiley, New York).
Murdin, B. N., Knippels, G. M. H., van der Meer, A. F. G., Pidgeon, C. R., Langerak, C. J. G. M., Helm, M., Heiss, W., Unterrainer, K., Gornik, E., Geerinck, K. K., Hovenier, N. J., and Wenckebach, W. Th. (1994). *Semicond. Sci. Technol.* **9**, 1554.
Murdin, B. N., Heiss, W., Langerak, C. J. G. M., Lee, S.-C., Galbraith, I., Strasser, G., Gornik, E., Helm, M., and Pidgeon, C. R. (1997). *Phys. Rev. B* **55**, 5171.
Nakayama, M. (1975). *J. Phys. Soc. Jpn.* **39**, 265.
Nakayama, M. (1977). *Solid State Commun.* **21**, 587.

Nee, S.-M., Claessen, U., and Koch, F. (1984). *Phys. Rev. B* **29**, 3449.
Nelson, D. F., Miller, R. C., and Kleinman, D. A. (1987). *Phys. Rev. B* **35**, 7770.
Newson, D. J., and Kurobe, A. (1988). *Semicond. Sci. Technol.* **3**, 786.
Nikonov, D. E., Imamoglu, A., Butov, L. V., and Schmidt, H. (1997). *Phys. Rev. Lett.* **79**, 4633.
Oberli, D. Y., Wake, D. R., Klein, M. V., Klem, J., Henderson, T., and Morkoc, H. (1987). *Phys. Rev. Lett.* **59**, 696.
Oelting, S., Merkt, U., and Kotthaus, J. P. (1986). *Surface Sci.* **170**, 402.
Olszakier, M., Ehrenfreund, E., Cohen, E., Bajaj, J., and Sullivan, G. J. (1989). *Phys. Rev. Lett.* **62**, 2997.
Park, J. S., Karunasiri, R. P. G., and Wang, K. L. (1992). *Appl. Phys. Lett.* **61**, 681.
Peeters, F. M., Matulis, A., Helm, M., Fromherz, T., and Hilber, W. (1993). *Phys. Rev. B* **48**, 12008.
Peng, L. H., and Fonstad, C. G. (1993). *Appl. Phys. Lett.* **62**, 3342.
Peng, L. H., and Fonstad, C. G. (1995). *J. Appl. Phys.* **77**, 747.
Peng, L. H., Smet, J. H., Broekaert, T. P. E., and Fonstad, C. G. (1992). *Appl. Phys. Lett.* **61**, 2078.
Peng, L. H., Smet, J. H., Brokaert, T. P. E., and Fonstad, C. G. (1993). *Appl. Phys. Lett.* **62**, 2413.
People, R., and Sputz, S. K. (1990). *Phys. Rev. B* **41**, 8431.
People, R., Bean, J. C., Bethea, C. G., Sputz, S. K., and Peticolas, L. J. (1992a). *Appl. Phys. Lett.* **61**, 1122.
People, R., Bean, J. C., Sputz, S. K., Bethea, C. G., and Peticolas, L. J. (1992b). *Thin Solid Films* **222**, 120.
Perera, A. G. U., Choe, J.-W., and Francombe, M. H. (1997). *Thin Films* **23**, 217.
Persson, A., and Cohen, R. M. (1988). *Phys. Rev. B* **38**, 5568.
Pikus, G. E., and Bir, G. L. (1960). *Sov. Phys. Solid State* **1**, 1502.
Pillath, J., Batke, E., Weimann, G., and Schlapp, W. (1989). *Phys. Rev. B* **40**, 5879.
Pinczuk, A., and Worlock, J. M. (1982). *Surf. Sci.* **113**, 69.
Pinczuk, A., and Abstreiter, G. (1989). In *Light Scattering in Solids V*, eds. Cardona, M., and Güntherodt, G. (Springer, Berlin), p. 153.
Pinczuk, A., Schmitt-Rink, S., Danan, G., Valladares, J. P., Pfeiffer, L. N., and West, K. W. (1989). *Phys. Rev. Lett.* **63**, 1633.
Ralston, J. D., Gallagher, D. F. G., Bittner, P., Fleissner, J., Dischler, B., and Koidl, P. (1992). *J. Appl. Phys.* **71**, 3562.
Ramsteiner, M., Ralston, J. D., Koidl, P., Dischler, B., Biebl, H., Wagner, J., and Ennen, H. (1990). *J. Appl. Phys.* **67**, 3900.
Rarity, J., and Weisbuch, C. (eds.). (1996). *Microcavities and Photonic Bandgaps: Physics and Applications* (Kluwer, Dordrecht).
Reisinger, H., and Koch, F. (1981). *Solid State Commun.* **37**, 429.
Rikken, G. L. J. A., Sigg, H., Langerak, C. J. G. M., Myron, H. W., Perenboom, J. A. A. J., and Weimann, G. (1986). *Phys. Rev. B* **34**, 5590.
Rössler, U. (1984). *Solid State Commun.* **49**, 943.
Rosencher, E., and Bois, Ph. (1991). *Phys. Rev. B* **44**, 11415.
Rosencher, E., Vinter, B., and Levine, B. F. (eds.). (1992). *Intersubband Transitions in Quantum Wells* (Plenum Press, New York).
Rosencher, E., Fiore, A., Vinter, B., Berger, V., Bois, Ph., and Nagle, J. (1996). *Science* **271**, 168.
Sa'ar, A. (1993). *J. Appl. Phys.* **74**, 5263.
Sadeghi, S. M., Young, J. F., and Meyer, J. (1995). *Phys. Rev. B* **51**, 13349.
Sakaki, H., Noda, T., Hirakawa, H., Tanaka, M., and Matsusue, T. (1987). *Appl. Phys. Lett.* **51**, 1934.

Schlesinger, Z., Hwang, J. C. M., and Allen, S. J., Jr. (1983). *Phys. Rev. Lett.* **50**, 2098.
Schmidt, H., and Imamoglu, A. (1996). *Opt. Commun.* **131**, 333.
Schmidt, H., Campman, K. L., Gossard, A. C., and Imamoglu, A. (1997). *Appl. Phys. Lett.* 70, 3455.
Schulman, J. N., and Chang, Y.-C. (1985). *Phys. Rev. B* **31**, 2056.
Seilmeier, A., Hübner, H. J., Abstreiter, G., Weimann, G., and W. Schlapp, W. (1987). *Phys. Rev. Lett.* **59**, 1345.
Shaw, M. J., and Jaros, M. (1994). *Phys. Rev. B* **50**, 7768.
Shayasteh, S. F., Dumelow, T., Parker, T. J., Mirjalili, G., Vorobjev, L. E., Donetsky, D. V., and Kastalsky, A. (1996). *Semicond. Sci. Technol.* **11**, 323.
Shayegan, M., Sajoto, T., Santos, M., and Silvestre, C. (1988). *Appl. Phys. Lett.* **53**, 791.
Sherwin, M. S., Craig, K., Galdrikian, B., Heyman, J., Markelz, A., Campman, K., Fafard, S., Hopkins, P. F., and A. C. Gossard (1995). *Physica D* **83**, 229.
Shik, A. (1988). *Sov. Phys. Semicond.* **22**, 1165.
Shik, A. (1992). In *Intersubband Transitions in Quantum Wells*, eds. Rosencher, E., Vinter, B., and Levine, B. F. (Plenum Press, New York), p. 319.
Sigg, H. (1992). In *Intersubband Transitions in Quantum Wells*, eds. Rosencher, E., Vinter, B., and Levine, B. (Plenum Press, New York), p. 83.
Sigg, H., Kwakernaak, M., Margotte, B., Erni, D., van Son, P., and Köhler, K. (1995). *Appl. Phys. Lett.* **67**, 2827.
Sirtori, C., Capasso, F., Faist, J., Sivco, D. L., Chu, S.-N. G., and Cho, A. Y. (1992). *Appl. Phys. Lett.* **61**, 898.
Sirtori, C., Capasso, F., Faist, J., and Scandolo, S. (1994). *Phys. Rev. B* **50**, 8663.
Smet, J. H., Peng, L. H., Hirayama, Y., and Fonstad, C. G. (1994). *Appl. Phys. Lett.* **64**, 986.
Smith, J. S., Chiu, L. C., Margalit, S., Yariv, A., and Cho, A. Y. (1983). *J. Vac. Sci. Tech. B* **1**, 376.
Stern, F., and Howard, W. E. (1967). *Phys. Rev.* **163**, 816.
Stockman, M. I., Pandey, L. N., and George, T. F. (1990). *Phys. Rev. Lett.* **65**, 3433.
Stoklitsky, S. A., Holtz, P. O., Monemar, B., Zhao, Q. X., and Lundström, T. (1994). *Appl. Phys. Lett.* **65**, 1706.
Stoklitsky, S. A., Zhao, Q. X., Holtz, P. O., Monemar, B., and Lundström, T. (1995). *J. Appl. Phys.* **77**, 5256.
Streibl, M., Warburton, R. J., Wixforth, A., Campman, K. L., and Gossard, A. C. (1996). In *Proc. 23rd Int. Conf. on the Physics of Semiconductors*, eds. Scheffler, M., and Zimmermann, R. (World Scientific, Singapore), p. 1739.
Sundaram, M., Chalmers, S. A., Hopkins, P. F., and Gossard, A. C. (1991). *Science* **254**, 1326.
Szmulowicz, F., and Brown, G. J. (1995). *Phys. Rev. B* **51**, 13203; *Appl. Phys. Lett.* **66**, 1659.
Szmulowicz, F., and Manasreh, M. O. (1992). *J. Vac. Sci. Technol. B* **10**, 1341.
Szmulowicz, F., Manasreh, M. O., Stutz, C. E., and Vaughan, T. (1994). *Phys. Rev. B* **50**, 11618.
Tatham, M. C., Ryan, J. F., and Foxon, C. T. (1989). *Phys. Rev. Lett.* **63**, 1637.
Terzis, A. F., Liu, X. C., Petrou, A., McCombe, B. D., Dutta, M., Shen, H., Smith, D. D., Cole, M. W., Taysing-Lara, M., and Newman, P. G. (1990). *J. Appl. Phys.* **67**, 2501.
Tsang, L., and Chuang, S. L. (1995). *IEEE J. Quant. Electron.* **31**, 20.
Ullrich, C. A., and Vignale, G. (1998). *Phys. Rev. B* **58**, 15756.
Vinter, B. (1976). *Phys. Rev. B* **13**, 4447.
Vinter, B. (1977). *Phys. Rev. B* **15**, 3947.
Vodopyanov, K. L., Chazapis, V., and Phillips, C. C. (1996). *Appl. Phys. Lett.* **69**, 3405.
Vodopyanov, K. L., Chazapis, V., Phillips, C. C., Sung, B., and Harris, J. S. (1997). *Semicond. Sci. Technol.* **12**, 708.
von Allmen, P. (1992). *Phys. Rev. B* **46**, 13351.

von Allmen, P., Berz, M., Petrocelli, G., Reinhart, F.-K., and Harbeke, G. (1988). *Semicond. Sci. Technol.* **3**, 1211.

Wang, K. L., and Karunasiri, R. P. G. (1993). In *Semiconductor Quantum Wells and Superlattices for Long-Wavelength Infrared Detectors*, ed. Manasreh, M. O. (Artech House, Boston), p. 139.

Wang, K. L., Lee, C., and Chun, S. K. (1994a). In *Quantum Well Intersubband Transition Physics and Devices*, eds. Liu, H. C., Levine, B. F., and Andersson, J. Y. (Kluwer Academic Publishers, Dordrecht), p. 221.

Wang, Y. H., Li, Sheng, S., Ho, Pin, and Manasreh, M. O. (1993). *J. Appl. Phys.* **74**, 1382.

Wang, Y. H., Li, Sheng, S., Chu, J., and Ho, Pin. (1994b). *Appl. Phys. Lett.* **64**, 727.

Warburton, R. J., Gauer, C., Wixforth, A., Kotthaus, J. P., Brar, E., and Kroemer, H. (1996). *Phys. Rev. B* **53**, 7903.

Warburton, R. J., Weilhammer, K., Kotthaus, J. P., Thomas, M., and Kroemer, H. (1998). *Phys. Rev. Lett.* **80**, 2185.

Wendler, L., Kraft, T., Hartung, M., Berger, A., Wixforth, A., Sundaram, M., English, J. H., and Gossard, A. C. (1997). *Phys. Rev. B* **55**, 2303.

West, L. C., and Eglash, S. J. (1985). *Appl. Phys. Lett.* **46**, 1156.

West, L. C., and Roberts, C. W. (1994). In *Quantum Well Intersubband Transition Physics and . Devices*, eds. Liu, H. C., Levine, B. F., and Andersson, J. Y. (Kluwer, Dordrecht), p. 501.

Wieck, A. D., Batke, E., Heitmann, D., and Kotthaus, J. P. (1984). *Phys. Rev. B* **30**, 4653.

Wieck, A. D., Maan, J. C., Merkt, U., Kotthaus, J. P., Ploog, K., and Weimann, G. (1987). *Phys. Rev. B* **35**, 4145.

Wieck, A. D., Bollweg, K., Merkt, U., Weimann, G., and Schlapp, W. (1988). *Phys. Rev. B* **38**, 10158.

Wieck, A. D., Thiele, F., Merkt, U., Ploog, K., Weimann, G., and Schlapp, W. (1989). *Phys. Rev. B* **39**, 10879.

Wieck, A. D., Sigg, H., and Ploog, K. (1990). *Phys. Rev. Lett.* **64**, 463.

Wiesinger, K., Reisinger, H., and Koch, F. (1982). *Surf. Sci.* **113**, 102.

Winkler, R., and Rössler, U. (1993). *Phys. Rev. B* **48**, 8918.

Wixforth, A., Kaloudis, M., Rocke, C., Ensslin, K., Sundaram, M., English, J. H., and Gossard, A. C. (1994). *Semicond. Sci. Technol.* **9**, 215 (and references therein).

Wixforth, A., Sundaram, M., Ensslin, K., English, J. H., and Gossard, A. C. (1991). *Phys. Rev. B* **43**, 10,000.

Xie, H., Piao, J., Katz, J., and Wang, W. I. (1991a). *J. Appl. Phys.* **70**, 3152.

Xie, H., Katz, J., and Wang, W. I. (1991b). *Appl. Phys. Lett.* **59**, 3601.

Xie, H., Katz, J., and Wang, W. I. (1992a). *J. Appl. Phys.* **72**, 3681.

Xie, H., Katz, J., and Wang, W. I. (1992b). *Appl. Phys. Lett.* **61**, 2694.

Xie, H., Katz, J., Wang, W. I., and Chang, Y. C. (1992c). *J. Appl. Phys.* **71**, 2844.

Xie, H., Wang, W. I., Meyer, J. R., Hoffman, C. A., and Bartoli, F. J. (1993). *J. Appl. Phys.* **74**, 1195.

Xie, H., Wang, W. I., and Meyer, J. R. (1994). *J. Appl. Phys.* **76**, 92.

Xu, B., and Hu, Q. (1997). *Appl. Phys. Lett.* **70**, 2511.

Xu, Wenlan, Fu, Y., and Willander, M. (1993). *Phys. Rev. B* **48**, 11477.

Xu, Wenlan, Willander, M., and Shen, S. C. (1994). *Phys. Rev. B* **49**, 13760.

Yang, C.-L., Pan, D.-S., and Somoano, R. (1989). *J. Appl. Phys.* **65**, 3253.

Yang, D. D., Julien, F. H., Lourtioz, J.-M., Boucaud, P., and Planel, R. (1990). *IEEE Photon. Technol. Lett.* **2**, 398.

Yang, R. Q. (1995a). *Appl. Phys. Lett.* **66**, 959.

Yang, R. Q. (1995b). *Phys. Rev. B* **52**, 11958.

Yang, R. Q., Xu, J. M., and Sweeny, M. (1994). *Phys. Rev. B* **50**, 7474.

Yi, K. S., and Quinn, J. J. (1983). *Phys. Rev. B* **27**, 2396.
Yoo, K. H., Ram-Mohan, L. R., and Nelson, D. F. (1989). *Phys. Rev. B* **39**, 12808.
Yu, L. S., Li, S. S., Wang, Y. H., and Kao, Y. C. (1992). *J. Appl. Phys.* **72**, 2105.
Yuh, P. F., and Wang, K. L. (1988). *Phys. Rev. B* **38**, 8377.
Yuh, P. F., and Wang, K. L. (1989). *J. Appl. Phys.* **65**, 4377.
Yuh, P. F., Kuo, T. C., and Wang, K. L. (1990). *J. Appl. Phys.* **67**, 3199.
Zaluzny, M. (1989). *Phys. Rev. B* **40**, 8495.
Zaluzny, M. (1991). *Phys. Rev. B* **43**, 4511.
Zaluzny, M. (1992a). *Solid State Commun.* **82**, 565.
Zaluzny, M. (1992b). *Appl. Phys. Lett.* **60**, 1486.
Zaluzny, M. (1996). *Solid State Commun.* **97**, 809.
Zaluzny, M., and Nalewajko, C. (1997). *J. Appl. Phys.* **81**, 3323.
Zaluzny, M., and Nalewajko, C. (1999). *Phys. Rev. B* **59**, 13043.
Zanier, S., Berroir, J. M., Guldner, Y., Vieren, J. P., Sagnes, I., Glowacki, F., Campidelli, Y., and Badoz, P. A. (1995). *Phys. Rev. B* **51**, 14311.
Zawadzki, W. (1983). *J. Phys. C* **16**, 229.
Zawadzki, W. (1987). *Semicond. Sci. Technol.* **2**, 550.
Zhang, Y., Baruch, N., and Wang, W. I. (1993). *Appl. Phys. Lett.* **63**, 1068.
Zhang, Y., Baruch, N., and Wang, W. I. (1994). *J. Appl. Phys.* **75**, 3690.
Zheng, L., Schaich, W. L., and MacDonald, A. H. (1990). *Phys. Rev. B* **41**, 8493.